Aerosol Optical Properties and Particle Size Distributions on the East Coast of the United States as Derived from Airborne In Situ and MISR Remote Sensing Measurements

David R. Reidmiller

A thesis
submitted in partial fulfillment of the
requirements for the degree of

Master of Science

University of Washington

2005

Program Authorized to Offer Degree:
Atmospheric Sciences

University of Washington
Graduate School

This is to certify that I have examined this copy of a master's thesis by

David R. Reidmiller

and have found that it is complete and satisfactory in all respects,
and that any and all revisions required by the final
examining committee have been made

Committee Members:

Peter V. Hobbs

Theodore L. Anderson

David S. Covert

Date: _____

In presenting this thesis in partial fulfillment of the requirements for a master's degree at the University of Washington, I agree that the Library shall make its copies freely available for inspection. I further agree that extensive copying of this thesis is allowable only for scholarly purposes, consistent with "fair use" as prescribed in the U.S. Copyright Law. Any other reproduction for any purposes or by any means shall not be allowed without my written permission.

Signature _____

Date _____

University of Washington

Abstract

Aerosol Optical Properties and Particle Size Distributions on the East Coast of the United States as Derived from Airborne In Situ and MISR Remote Sensing Measurements

David R. Reidmiller

Chair of the Supervisory Committee:
Professor Peter V. Hobbs
Department of Atmospheric Sciences

Airborne in situ measurements of vertical profiles and horizontal transects of aerosol optical and physical properties, obtained during the Chesapeake Lighthouse and Aircraft Measurements for Satellites (CLAMS) field campaign off the East Coast of the United States during the summer of 2001, are presented. Most of the measurements were obtained in relatively clean air dominated by airflows that had passed over Canada and the northern Atlantic Ocean. Results from two flights are presented (July 17 and August 2, 2001); on these days the aerosol loading was relatively high. Comparisons of airborne in situ measurements versus remotely sensed aerosol parameters, such as the single-scattering albedo (ω_0), aerosol optical depth (AOD) and effective radius (r_{eff}) of particles, derived from the Multi-angle Imaging Spectro-Radiometer (MISR) aboard the Terra satellite were in good agreement. Mid-visible wavelength values of AOD and ω_0, as well as values of r_{eff}, obtained from the aircraft and MISR measurements were the same, given the associated uncertainties. In the lower troposphere, ω_0 values at a wavelength of 550 nm were consistently above 0.93 throughout the field experiment, indicating the dominance of highly non-absorbing aerosol. The number size, surface area and volume

distributions of particles are presented and discussed for transects at altitudes ~0.05 to 3.5 km above mean sea level. These size distributions show there was a dominance of sub-micrometer particles. Specifically, particles with diameters (D_p) <0.1 μm made up the majority of the aerosol number. The variability of optical and physical aerosol parameters was analyzed on horizontal scales down to ~1-4 km. There was little horizontal variability in ω_0, aerosol optical depth, and the accumulation mode size, but greater variability in particle number concentration and the coarse mode size. The aerosol properties derived from aircraft data in CLAMS are compared to those collected during TARFOX, a field campaign conducted in the same region and during the same time of year as CLAMS. Single-scattering albedo and accumulation mode size parameters are similar for both experiments, but particle number concentration, aerosol optical depth and particle composition were significantly different. In general, the MISR retrievals captured both the similarities and the differences in the properties of the aerosol on July 17 versus those on August 2.

TABLE OF CONTENTS

LIST OF FIGURES

LIST OF TABLES

ACKNOWLEDGEMENTS

Each person in the University of Washington Cloud and Aerosol Research Group (CARG) has been instrumental to the writing of this thesis. Foremost, I thank my advisor, Peter Hobbs, for the guidance, encouragement, support and freedom he provided during the work on this project. I am also indebted to my thesis committee members, Tad Anderson and David Covert, for their useful suggestions, flexibility and advice over the past three years. Ralph Kahn provided MISR results and has served as an invaluable mentor. I also thank my fellow graduate students in CARG: Ricky Sinha, Louise Leahy, and especially Brian Magi for answering innumerable questions and providing encouragement when needed.

I am grateful for the support and encouragement from my parents and especially my brother, who has served as an ideal, if not knowing, mentor throughout the years.

Finally, I thank my friends here in Seattle, especially the Atmospheric Sciences graduate students from the entering class of 2002. Jimmy Booth and Joe Casola in particular, have made the past couple of years truly memorable.

CHAPTER 1

BACKGROUND AND SCOPE OF THESIS

1.1 Introduction

The Earth's atmosphere consists not only of a mixture of gases, but also small solid or liquid particles called *aerosols*. These tiny atmospheric particles originate from a variety of natural (e.g., biological, oceanic, crustal, etc.) and anthropogenic (e.g., fuel combustion, industrial processes, land use changes, etc.) sources. Natural and anthropogenic aerosols play an important role in air chemistry, visibility, the formation of cloud particles and atmospheric radiation. Aerosols attenuate solar radiation as it passes through the atmosphere, which in turn affects the radiative budget (Fig. 1.1) and, thus, the temperature of the Earth.

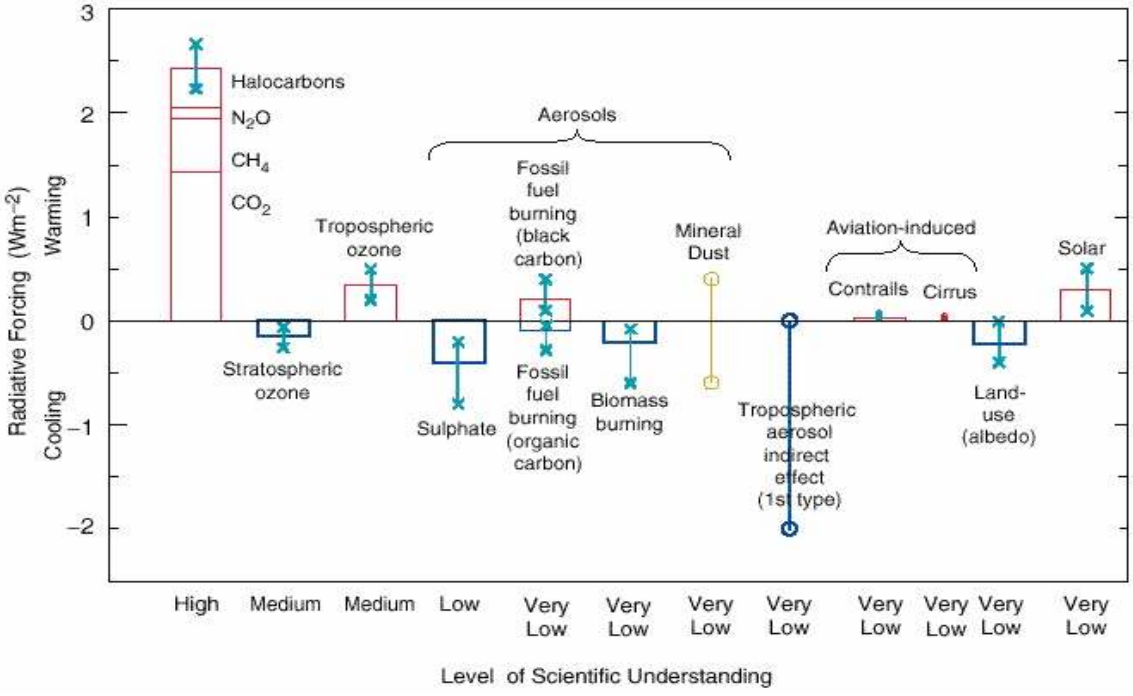

Figure 1.1 Top-of-atmosphere radiative forcing due to several agents (from IPCC, 2001).

The amount of attenuation depends on several factors, including the light scattering coefficient (σ_s), light absorption coefficient (σ_a), the aerosol single-scattering albedo (ω_0), particle number concentrations (N), particle size distributions and particle composition. Single-scattering albedo is defined as the fraction of light extinction, σ_e (where light extinction is defined as the sum of the light scattering and absorption coefficients, $\sigma_s + \sigma_a$) that is scattered. For the work presented herein, ω_0 is defined by:

$$\omega_0 = \sigma_{sp} \Big/ \left(\sigma_{sp} + \sigma_{apd} \right) \tag{1}$$

where σ_{sp} is the light scattering coefficient due to particles and σ_{apd} is the light absorption coefficient due to dried particles (i.e., the effect of hydration on the light absorption coefficient has been neglected for reasons that will be discussed in Section 2.7). Figure 1.1 shows the top-of-atmosphere (TOA) radiative forcing due to a number of agents, including scattering and absorbing particles (adapted from IPCC, 2001).

1.2 Basic Aerosol Properties

Aerosols can be described broadly by their physical and optical properties. Size is an important physical property, and is the focus of much of the work presented herein. Most aerosols begin as trace atmospheric gases (such as SO_2, NH_3, etc.) that condense via nucleation processes, such as gas-to-particle conversion, to form Aitken, or *nucleation mode*, particles with diameters (D_p) <0.01 μm (e.g., Hobbs 2000). Nucleation mode particles grow by: 1) further condensation of trace gases, and/or 2) colliding and coagulating with other particles due to the aerosols being in constant Brownian motion. These processes produce particles in the 0.01 μm < D_p < 1 μm size range, the so-called

accumulation mode. Growth much beyond 1 μm is slow via these processes because the particles are now too large to grow rapidly by condensation of trace gases and also because they have less Brownian motion, which reduces the collision/coagulation rate. As a result, the majority of particles in the atmosphere with $D_p > 1$ μm (*coarse mode* particles) are produced by direct emission from industrial processes, or by mechanical processes such as bubble-bursting over the oceans, dust storms, etc. (Seinfeld and Pandis 1998). Particle size is also important because it determines how well a given particle will scatter or absorb light. The most efficient light scatterers are those particles having a diameter that is similar to the wavelength of incident radiation. For example, when discussing the attenuation of incident solar radiation, particles having $0.4\ \mu m < D_p < 0.8$ μm would be the most efficient light scatterers.

Aerosol optical properties of significance include aerosol optical depth (AOD) and single-scattering albedo (ω_0), both of which are wavelength-dependent properties. AOD is defined as the column-integrated value of the light extinction coefficient, σ_e, and is represented mathematically by:

$$AOD = \int_{z}^{\infty} \sigma e dz \tag{2}$$

In other words, AOD is a measure of the degree to which aerosols prevent light from passing through the atmosphere. This value depends on the size, shape, number concentration and index of refraction of the particles. Typical AOD values at mid-visible wavelengths are ~0.3-0.5 for polluted air (e.g., urban air; continental, stagnant airmasses downwind of industrialized regions; air near areas of biomass burning; certain desert

areas where windblown sand is concentrated; etc.) and ~0.1-0.2 for fairly clean air (e.g., remote continental air; marine air; polar air; etc.).

Single-scattering albedo is defined here by Eqn. (1). Therefore, a ω_0 value of 1.0 indicates the aerosol is perfectly scattering. As this value decreases from unity, the aerosol has a more absorbing component. The single-scattering albedo depends on the particle size distribution and chemical composition. When discussing ω_0 values at mid-visible wavelengths, particle size is important (as discussed previously in Section 1.2), as is particle composition. If the aerosol is composed of compounds that are highly absorbing (e.g., black carbon), ω_0 values will be relatively low and vice versa.

1.3 Importance of Aerosols in the Troposphere

Tropospheric aerosols are of great importance due to their wide-ranging effects, which include: 1) human health impacts, 2) visibility reduction, 3) acid deposition and other chemical interactions, and 4) perturbing the Earth's radiation balance. Ambient atmospheric particles can have detrimental respiratory effects on human health, especially in urban environments (e.g., Peters et al. 1997; Ibald-Mulli et al. 2002). Peters et al. (1997) illustrate how the particle size distributions help elucidate the properties of ambient aerosols responsible for negative health effects. Atmospheric particles also play a large role in reducing visibility by contributing to the presence of haze layers (e.g., Sloane and White 1986; Seinfeld 1989). The role of aerosols in atmospheric chemistry is currently an area of significant research. Aerosols not only serve as sites on which

chemical reactions can occur (e.g., Worsnop et al. 2002), but they also play a large role in tropospheric acid deposition (e.g., Parungo et al. 1987).

Atmospheric particles play both a direct and indirect role in modifying the Earth's radiative balance (e.g., Haywood and Boucher 2000). Their direct effect is to primarily scatter (and to a lesser degree, absorb) incoming solar radiation, thus increasing (decreasing) ω_0, and causing a negative (positive) forcing. The indirect effect aerosols have on the radiative balance is their role in cloud formation, lifetime, thickness, coverage, etc. While the uncertainty associated with the magnitude of this indirect aerosol effect is still large, the best available research indicates it is a negative forcing that may be equal to, or greater than, the magnitude of the forcing due to the direct aerosol effect (Charlson et al. 1992).

1.4 Methods for Measuring Aerosol Properties

In view of the importance of aerosols in the Earth system, increasing attention has been given over the past fifty years or so to accurately measuring aerosol properties. Jaenicke (1993) discusses the evolution of measuring techniques. Until the late nineteenth century, when Aitken developed the first particle counters, visual observations of atmospheric aerosols were the only available means of gleaning information on aerosols. Aircraft measurements throughout the latter half of the twentieth century allowed in situ characterization of aerosol properties in a finite atmospheric layer. Currently, satellite sensors allow total column average aerosol properties to be remotely sensed around the globe. One such remote sensing instrument is the Multiangle Imaging Spectro-

Radiometer (MISR) on the NASA EOS Terra platform, which will be discussed in detail in Section 2.15 (Diner et al. 1998). However, aerosol retrieval validation from these remote sensing instruments is very challenging because column effective aerosol properties are needed. One of the most reliable ways for obtaining such measurements is to determine aerosol properties (e.g., particle size, σ_{sp}, σ_{apd}, etc.) at multiple levels of the atmosphere and, to the degree possible, construct an "environmental snapshot" of as much of the atmospheric column as possible (e.g., Kahn et al. 2004). However, ground-based sunphotometry (such as the AErosol RObotic NETwork [AERONET] system) is the most reliable means of obtaining column-effective AOD and its wavelength dependence. We use both measurement/analysis techniques here.

1.5 Overview of the Chesapeake Lighthouse and Aircraft Measurements for Satellites (CLAMS) Experiment

One such field campaign, designed to provide in situ "environmental snapshots" for satellite validation, was the Chesapeake Lighthouse and Aircraft Measurements for Satellites (CLAMS) experiment. CLAMS was conducted from July 10-August 2, 2001 off the East Coast of the United States (Fig. 1.2) and served primarily as a validation experiment for satellite-based retrievals of aerosol properties and radiative fluxes.

A variety of measuring platforms were utilized in CLAMS on the ground, in the air and in orbit. An AERONET site was one ground-based measuring platform employed during CLAMS. AERONET is a globally distributed network of Sunphotometers that

provide measurements of spectral AOD and various inversion products, including particle size parameters and ω_0.

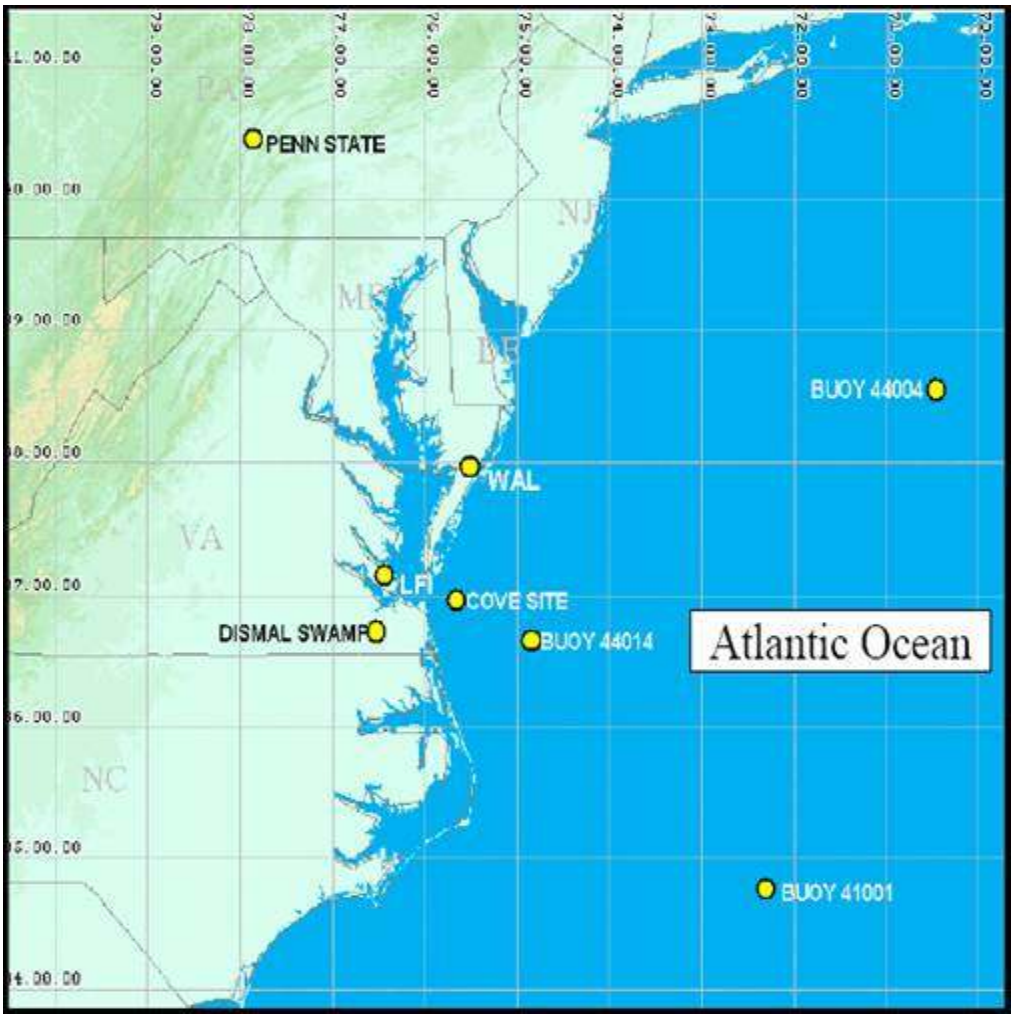

Figure 1.2 Study region of CLAMS field campaign over eastern U.S. seaboard.

The Clouds & Earth's Radiant Energy System (CERES) Ocean Validation Experiment (COVE), located at the Chesapeake Bay Lighthouse, measured upwelling and net atmospheric radiative fluxes for validation of the CERES satellite sensor. Coincidentally, COVE is also an AERONET site, and it is also instrumented to monitor various meteorological and oceanic conditions.

Six low- and high-flying aircraft were used during CLAMS: the University of Washington's Convair-580, NASA's ER-2 and OV-10, the Proteus, a Cessna 210, and a Lear-25C Jet. The satellite sensors whose retrievals were being validated in CLAMS included the MODerate Resolution Imaging Spectroradiometer (MODIS), the Clouds & Earth's Radiant Energy System (CERES), and the Multiangle Imaging Spectro-Radiometer (MISR). The NASA ER-2 flew at ~20 km MSL and was home to airborne versions of both MODIS and MISR and was also equipped with a Scanning High-resolution Interferometer Sounder and the Advanced Visible/Infrared Imaging Spectrometer for measuring longwave and shortwave spectra, respectively. The OV-10 aircraft generally flew within 0.5 km MSL and was configured to measure upwelling and downwelling longwave (broadband) and shortwave (broadband and spectral) irradiances. The Proteus aircraft typically flew at ~17 km MSL and was equipped with a Far-Infrared Spectrometer for Cirrus (a high resolution interferometer measuring from 70 to 1000 μm), as well as a 17-channel scanning microwave radiometer used for temperature sounding through non-precipitating clouds and for deriving precipitation cell height. A nine channel visible and near infrared Research Scanning Polarimeter was aboard the Cessna 210. This aircraft flew at ~3.5 km MSL to obtain intensity and polarization measurements to retrieve aerosol properties and at ~ 50 m MSL to retrieve ocean optical properties. The NASA Langley Airborne A-Band (765 nm) Spectrometer was flown on a Lear-25C jet at ~12 km MSL to demonstrate its capability for AOD retrievals. The Convair-580 aircraft was instrumented to measure the physical, optical, and chemical properties of the aerosol in situ. Together, the sub-orbital measurements made aboard

these six aircraft provide a robust dataset characterizing radiative fluxes and aerosol properties with which validation analyses for MODIS and MISR can be performed. The research presented herein utilizes in situ measurements made aboard the Convair-580 aircraft to provide validation information for MISR.

1.6 Objectives of Thesis

There are three main objectives to this thesis work. The first is to characterize the aerosol optical properties and particle size distributions during CLAMS using in situ measurements made aboard the Convair-580 aircraft. These results are then compared to those from the Tropospheric Aerosol Radiative Forcing Observational Experiment (TARFOX), which took place in 1996 in the same general region and during the same period of the year as CLAMS. The second goal is to analyze the small-scale horizontal variability of several aerosol parameters. The motivation for this was to determine if the resolution of MISR's aerosol retrieval algorithm (~17.6 km) is fine enough to capture small-scale horizontal differences, and also to justify the methodology employed in providing "total layer mean" values from our in situ measurements. The third objective is to compare our in situ results to the remotely sensed MISR aerosol properties (specifically, accumulation mode effective particle radius, single-scattering albedo and aerosol optical depth) in an effort to validate the MISR retrieval algorithm.

Smith et al. (2005) present a thorough discussion of the CLAMS field campaign, its objectives, platforms and instrumentation and some preliminary results. Magi et al. (2005) and Castanho et al. (2005) discuss chemical composition and apportionment of

AOD of aerosol in CLAMS as measured aboard the Convair-580. Redemann et al. (2005) describe the horizontal variability of AOD in CLAMS. Table 1.1 lists the dates and times of all the Convair-580 aircraft's flights, as well as the times of the Terra overpasses. On some dates, MISR data is available but the Convair-580 did not fly. On three occasions (July 17, 26 and August 2) the Convair-580 underflew the Terra satellite. Since July 26 was cloudy and the MISR aerosol retrieval algorithm has limitations in could-screening, measurements obtained on July 17 and August 2 (under generally clear skies) are the focus here.

Table 1.1 Flight dates, UW flight numbers, times and locations along with relevant Terra overpasses for the eleven flights in which the Convair-580 collected data during CLAMS.

Date (2001)	University of Washington Flight Number	Period of Flight (UTC)	Principal Locations	Terra (MISR) Overpass
July 10	1870	1725-2220	Near Chesapeake Bay Lighthouse (COVE)	1602 UTC (CV-580 take-off delayed; overpass missed)
July 12	1871	1102-1640	Near Chesapeake Bay Lighthouse (COVE)	N/A
July 14	1872	1433-1749	Near Chesapeake Bay Lighthouse (COVE)	N/A
July 16	1873	1630-1947	Near Chesapeake Bay Lighthouse (COVE) and buoys 44014 and 41001	N/A
July 17 "Golden Day"	1874	1228-1816	1) Near Chesapeake Bay Lighthouse (COVE) 2) Great Dismal Swamp	1608 UTC

Table 1.1 (continued)

July 23	1875	1351-1646	~70 miles east of Wallops Flight Center	N/A
July 26	1878	1528-1909	1) Chesapeake Bay Lighthouse (COVE) 2) Buoy 44014	1607 UTC (cloudy skies)
July 30	1879	1609-1951	1) Chesapeake Bay Lighthouse (COVE) 2) Buoy 44014	N/A
July 31	1880	1424-2004	1) Buoy 44004 2) From buoy 44004 to Great Dismal Swamp via COVE	N/A
August 2	1881	1521-1859	1) Chesapeake Bay Lighthouse (COVE) 2) Buoy 44014 3) ~60 miles east of Wallops Flight Center	1608 UTC
August 2	1882	1914-2042	Chesapeake Bay Lighthouse (COVE)	N/A

CHAPTER 2

INSTRUMENTATION AND CALIBRATION

The University of Washington's (UW) Convair-580 (CV-580) aircraft flew 11 flights during CLAMS, each lasting 3-6 hours. Aboard the aircraft was a variety of instrumentation, some of which was designed to measure the physical, optical, and chemical aerosol properties. A summary of the instrumentation, its manufacturer, relevant detection limits, etc. used in the results presented here is given in Table 2.1.

Typical Convair-580 flight patterns during CLAMS are shown in Figures 2.1a-b. Figure 2.1a illustrates a time/height cross-section for the CLAMS "Golden Day" flight on July 17, 2001. Figure 2.1b shows the time/height cross-section for the August 2, 2001 flight. These figures show flight patterns consisting of several horizontal transects ranging in altitude from ~0.05 to ~3.5 km above mean sea level (MSL) and several vertical profiles, which provided characterization of atmospheric particles in the lower troposphere. Each transect was flown for up to 45 minutes, with continuous measurements being made. Along-wind and cross-wind legs were flown to measure horizontal variabilities. Except for surface temperature and pressure, all of the sub-orbital measurements presented in this paper were obtained aboard the UW Convair-580 research aircraft. The aerosol instruments were located on two interior aircraft racks and under the left wing of the aircraft; they sampled air from a continuous airstream (the equivalent of ambient air). An important objective of CLAMS was to provide height-resolved aerosol optical and physical properties as validation data against which to test

the remotely sensed aerosol parameters derived from MISR. Therefore, it is of extreme importance to ensure the Convair-580 instrumentation and sampling system were calibrated accurately. In the remainder of this section we describe the calibration procedures and operating principles for the instruments aboard the Convair-580 and the MISR instrument.

Table 2.1 Instruments aboard the Convair-580 aircraft used in this study

Parameter	Instrument Type	Manufacturer/Model	Range (and Error)
Latitude & longitude	Global positioning system (GPS)	Trimble TANS/Vector	Global (~2-5 m)
Pressure	Variable Capacitance	Rosemount Model 830BA	1100 to 150 hPa (<0.2%)
Temperature	Reverse-flow	In-house	-60 to 40° C
Humidity	IR optical hygrometer	Ophir Model IR-2000	0 to 10 g m^{-3}
Light scattering coefficient at 30% RH (σ_{spd})	Integrating 3-wavelength nephelometer with backscatter shutter	MS-Electron 3W-02 (custom built for UW)	0.1 to 1000 Mm^{-1} at 450, 550, 700 nm (~10%)
Light absorption coefficient at low RH (σ_{apd})	Particle & Soot Absorption Photometer (PSAP)	Radiance Research	0.1 to 10000 Mm^{-1} at 567 nm (~25%)
Aerosol optical depth (AOD)	14-channel Sunphotometer (AATS-14)	NASA Ames	14 discrete wavelengths from 354-1558 nm
Particle size distribution	35 to 120° light scattering	Particle Measuring Systems Model PCASP-100X	Particle diameters 0.12 to 3.0 μm, 15 channels
Particle size distribution	4 to 12° light scattering	Particle Measuring Systems Model FSSP-300	Particle diameters 0.3 to 20 μm, 31 channels
Particle size distribution	"Time-of-flight"	TSI Model 3320 APS	Particle diameters 0.36 to 1.0 μm, 15 channels
Particle number concentration (N)	Condensation particle counter	TSI Model 3022A	0-10^7 cm^{-3} (D_p > 7 nm)
Particle number concentration (N)	Condensation particle counter	TSI Model 3025A	0-10^5 cm^{-3} (D_p > 3 nm)

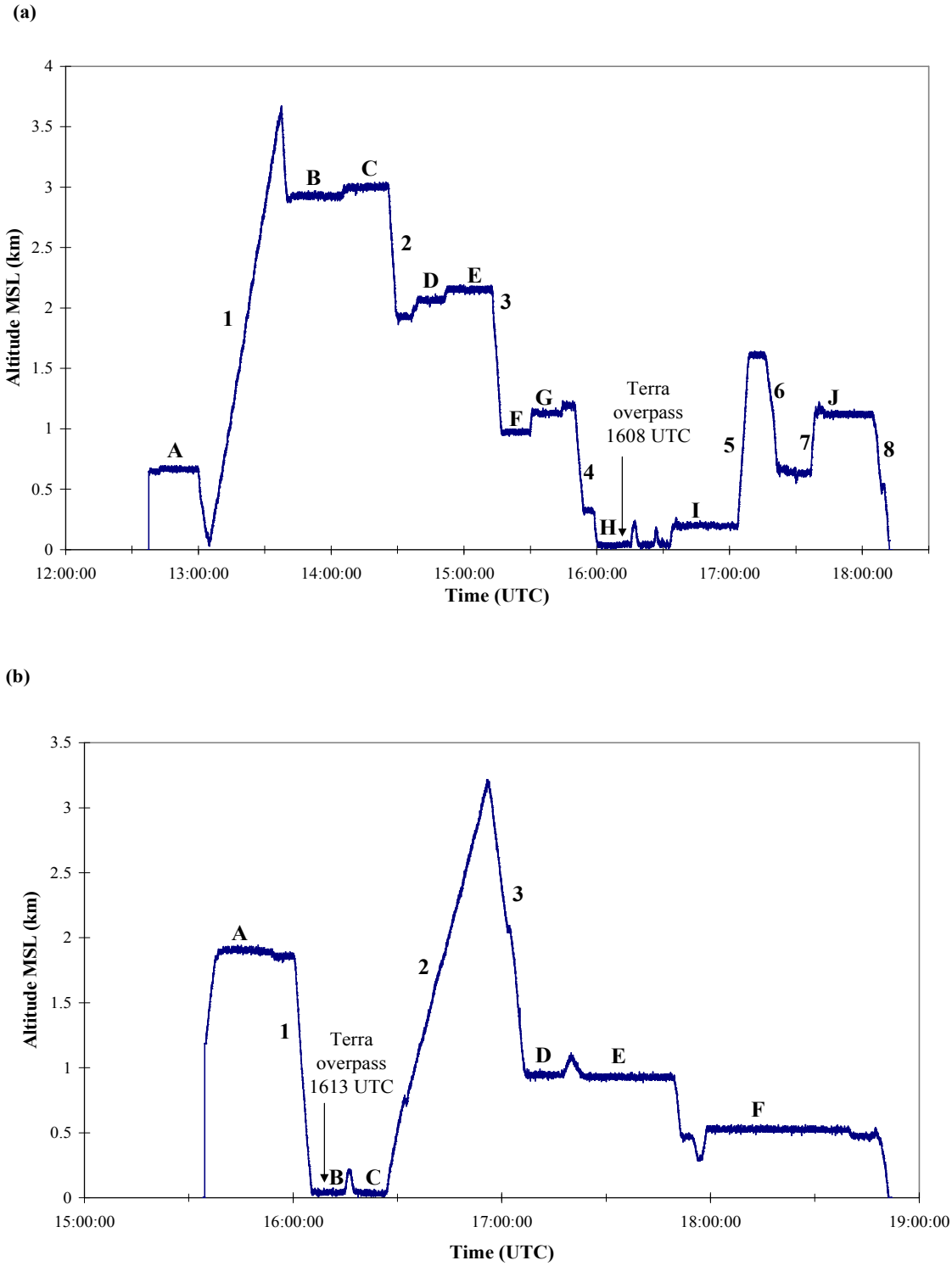

Figure 2.1 Time/height cross-sections of (a) July 17, 2001 and (b) August 2, 2001 Convair-580 flights.

2.1 Aircraft Location

Aircraft location and altitude were measured in-flight from an onboard global positioning system (GPS). However, since the GPS suffered from periodic outages, in post-analysis the altitude of the Convair-580 was determined using the hypsometric equation (e.g., Wallace and Hobbs 1977), the onboard temperature and pressure measurements, and hourly surface temperature and pressure measurements made at the Wallops Flight Facility, Virginia. In all cases, altitude is reported as above mean sea level (MSL). Table 2.2 divides the two flights of interest here into vertical profiles and horizontal transects.

2.2 Pressure

Ambient pressure was measured with a Rosemount 830BA barometer (range: 1100 to 150 hPa), which was calibrated prior to CLAMS (on April 17, 2001) over Paine Field, Washington State, where several flybys of the FAA air traffic control tower were conducted. The differences between the tower static pressure and the raw (i.e., no corrections applied) Convair-580 pressure fell within the manufacturer's tolerance of 0.1% accuracy. The Rosemount barometer was calibrated again during CLAMS (on July 14, 2001) via a coordinated flight with the Wallops Island NWS rawinsonde; again, any differences in the two measurements were within the accuracy of the Rosemount.

Table 2.2 Description of the July 17 and August 2 Convair-580 flights during CLAMS. Each flight consisted of a series of vertical profiles (numbers) and horizontal transects (letters) at various altitudes ranging from sea level (~50 m MSL) to ~3.5 km MSL. Horizontal ranges in the aircraft's flight path were determined using data from the on-board GPS. Altitudes are calculated using the hypsometric equation with on-board temperature and pressure measurements, as well as surface temperature and pressure measurements from the Wallops Flight Facility, VA. Mean (with one SD) and maximum RH values are listed for each profile and transect, as well. An asterisk (*) in the "Profile/Transect" column indicates the time when a Terra (MISR) overpass occurred.

Date (2001)	Profile/ Transect	Relative Humidity (%)		Range of Horizontal Position in Aircraft Profile (km)		Altitude Range (km MSL)	Duration (min)
		Mean ± 1 SD	Max	Zonal	Meridional		
July 17	1	60 ± 12	79	10.7	8.9	0.10-3.63	32
	2	63 ± 10	78	6.2	4.4	1.91-2.98	4
	3	58 ± 7	66	18.7	8.9	1.01-2.08	4
	4	46 ± 10	65	24.9	2.2	0.31-1.19	5
	5	57 ± 4	64	4.5	4.4	0.21-1.59	5
	6	61 ± 9	76	19.6	17.7	0.68-1.56	5
	7	58 ± 7	71	7.2	8.9	0.70-1.15	2
	8	54 ± 8	64	15.8	23.2	0.11-1.10	7
	A	40 ± 3	49	16.8	102.9	0.66	14
	B	71 ± 7	83	65.0	26.5	2.92	25
	C	75 ± 4	86	73.9	15.5	2.99	20
	D	60 ± 5	73	27.6	14.4	2.06	12
	E	74 ± 4	84	44.5	6.6	2.15	15
	F	36 ± 4	45	52.5	16.6	0.97	13
	G	45 ± 5	56	50.8	5.5	1.13	14
	H*	72 ± 4	84	73.0	7.7	0.04	16
	I	63 ± 4	73	11.6	7.7	0.20	29
	J	62 ± 6	83	57.6	101.8	1.12	21
August 2	1	66 ± 3	72	8.0	16.6	0.05-1.83	5
	2	57 ± 19	76	23.1	14.4	0.05-3.18	30
	3	50 ± 20	74	24.9	13.3	1.00-3.17	10
	A	58 ± 7	78	28.4	90.7	1.88	22
	B*	70 ± 3	77	44.5	1.1	0.07	9
	C	71 ± 3	80	45.4	2.2	0.03	9
	D	69 ± 5	80	53.4	0.0	0.94	11
	E	62 ± 12	83	24.8	108.4	0.93	26
	F	62 ± 7	80	111.6	84.1	0.52	40

2.3 Temperature

Ambient temperature was measured with a UW-manufactured reverse-flow thermometer (range: -60 °C to 40 °C), which was calibrated on April 17, 2001, prior to CLAMS with several flybys of the FAA control tower at Paine Field. The raw aircraft temperature readings were, on average, 2.5 °C below the temperature recorded by the control tower. However, it is suspected that the measurements may have been affected by heat coming from the tower.

The reverse-flow thermometer was calibrated again during CLAMS on July 14, 2001, when the Convair-580 flew a coordinated flight up to ~5 km MSL with a rawinsonde launched from Wallops Island. The reverse-flow temperature was generally lower than the rawinsonde temperature by 1-2 °C. The best-fit linear regression derived from the sounding produced the following adjustment to the raw temperatures (T_{raw}) recorded by the reverse-flow thermometer:

$$T_{corrected} = 0.98T_{raw} + 0.9 \quad (3)$$

Comparisons of the rawinsonde temperatures to the raw and to the corrected Convair-580 reverse-flow temperature measurements, respectively, showed that adequate agreement (within 0.2 °C) was achieved. The uncertainty associated with ambient temperature measurements obtained from the reverse-flow thermometer is ± 0.5 °C.

2.4 Humidity

In-flight relative humidity (RH) was measured with an Ophir Model IR-2000 optical hygrometer. This instrument was calibrated on July 14, 2001 in a coordinated

flight with a rawinsonde launched from Wallops Island. The dewpoint temperatures derived from the Cambridge cooled-mirror dew points aboard the Convair-580 were often lower by 2-4 °C than those measured by the rawinsonde. These differences were probably due to rapid local fluctuations in humidity in space and time in the field of cumulus clouds that was present, and the fact that the Convair-580 could not fly exactly the same path as the rawinsonde. However, averaging the Convair-580 derived dew points from the Ophir optical hygrometer over 10 s produced an average dewpoint temperature that was only ~0.5 °C lower than the rawinsonde. As a result, in post-analysis the dew points measured from the Convair-580 were raised by 0.5 ºC. Mean (with one standard deviation) and maximum RH values for each profile and transect of both flights are reported in Table 2.2. The instrumental uncertainty is ± 0.5 ºC for dew point ($T > 0$ ºC) and 0.6 ºC for frost point ($T \leq 0$ ºC) as discussed by Hartley et al. (2000). Given the small uncertainties associated with the measurements of ambient temperature and dewpoint temperature, the uncertainty associated with the ambient RH values is estimated at ± ~5%.

2.5 Aerosol Inlet and Plumbing

The aerosol sampled during CLAMS aboard the Convair-580 aircraft, with the exception of those detected by the PCASP (Section 2.9) and FSSP-300 (Section 2.10), had to pass through an inlet on the top of the aircraft, followed by tubing to the respective instrument. The stainless steel inlet (outer diameter ~ 3 cm) was designed to minimize particle losses and maximize isokineticity (and avoid turbulence) by capping the inlet

with a diffuser that had a 6:1 expansion ratio and an expansion half-angle of ~ 5°. The exterior profile was NACA 150 to decrease sensitivity to the angle of entry. The tubing connecting this inlet to the PSAP and nephelometer was approximately 3.0 cm (outer diameter), flexible and conductive to prevent the loss of ionic particles. Narrower (outer diameter ~ 1.0 cm) PVC tubing (non-conductive) came off this wider, more flexible tubing to bring ambient air to the APS and the two CPC counters. Despite the meticulous design of this plumbing system, there is no documentation of tests being performed to determine the passing efficiency of particles through the inlet/plumbing system. However, the scientist charged with designing this system is confident that the passing efficiency for the inlet/tubing going to the PSAP and nephelometer was essentially 100% up to ~ 3.0 μm (personal communication, D. Hegg 2005). Using the data presented here, though, it appears that some particles with diameters > ~1.0 μm were not detected efficiently by the APS due to loss to the tubing, inability to be captured by the inlet, etc. (these super-μm particle losses are of negligible concern for the CPCs, since the smallest particles heavily dominated number concentration). This is illustrated by results that will be described later (Section 3.1) showing number concentrations of super-μm particles, as measured by the PCASP and FSSP-300 (both mounted under a wing of the aircraft), that are several orders of magnitude greater than those measured by the TSI 3320 APS. Therefore, the APS and CPC results presented here should be viewed as pertaining to sub-μm aerosol and some unknown portion of super-μm particles.

2.6 Light Scattering Coefficient (σ_{sp})

The dry aerosol light scattering coefficient, σ_{spd}, was measured with a custom-built MS Electron integrating three-wavelength (450, 550 and 700 nm with a nominal 40 nm bandwidth) nephelometer. The MS Electron integrating nephelometer is similar to the commercially available TSI nephelometer (Anderson et al. 1996; Anderson and Ogren 1998), but it had an improved (closer to Lambertian) light source. Hartley et al. (2000) discuss the corrections for forward angular truncation and non-Lambertian illumination to give the total aerosol scattering coefficient (0° to 180°) and the hemispheric backscattering coefficient (90° to 180°). The authors also discuss the accuracy of the light scattering coefficient measurements, which is ~10% for polluted air dominated by accumulation mode particles. The accuracy decreases, though, for cleaner conditions or when coarse mode particles dominate.

The air stream to the nephelometer was heated to dry the aerosol and lower the RH (to ~30%), thereby reducing the effects of ambient RH on the measured aerosol light scattering and backscattering coefficients. To allow for the effects of varying ambient RH in CLAMS (ranging from 40-80%, with a mean of ~60%) on the ambient scattering coefficients, a humidification correction factor was applied to the dry aerosol light scattering coefficient measurements to adjust them to the ambient RH. Unfortunately, the humidograph that had been employed on previous Convair-580 field campaigns to determine the humidification correction factor was not working throughout CLAMS. As a result, the empirical expression derived by Kotchenruther et al. (1999), from the

Tropospheric Aerosol Radiative Forcing Observational Experiment (TARFOX) data set collected in the same locale as CLAMS, was used:

$$\sigma_{sp} = \sigma_{spd}\left(1 + a\left[RH/100\right]^{b}\right) \quad (4)$$

where "a" and "b" are fitting parameters that vary with air parcel backtrajectories. Use of Eq. (2) assumes that the aerosol in CLAMS was of similar size and composition to aerosol measured by Kotchenruther et al. (1999). As will be discussed later, values of ω_0 and various size parameters were virtually identical in the two campaigns, but the aerosol composition differed as discussed by Magi et al. (2005). As Magi et al. (2005) explain, we can assume the Kotchenruther et al. (1999) results provide a lower bound for the RH growth in CLAMS and use theoretical growth curve parameterizations for pure sulfate aerosols as determined by Li et al. (2001) to estimate an upper bound. Since Magi et al. (2005) show that aerosol composition in CLAMS was heavily dominated by sulfate, we can determine the degree of acidity of the pure sulfate aerosol based on a study by Brook et al. (1997) and air parcel back trajectories during CLAMS. Using these upper and lower limits for f(RH), we found that the uncertainty associated with using Eq. (1) to ultimately calculate values of ω_0 was ± 0.035 (or ± ~4 %). Also, it should be noted that Eq. (4) does not work well to describe hygroscopic growth at low RH (i.e., < 40%). Regarding Convair-580 flight paths on the two days of interest, the RH was < 40% only at altitudes > 2.5 km on August 2, 2001. For these measurements, we have assumed a hygroscopic growth factor of 1.0.

Figures 2.2 and 2.3 show air parcel backtrajectories at various altitudes for the July 17 and August 2 flights, respectively, which were obtained using NOAA's

HYSPLIT analysis tool (available online at http://www.arl.noaa.gov/ready/hysplit4.html). Kotchenruther et al. (1999) considered three broad backtrajectory classifications. Westerly flows, which passed over regions of the continental U.S. (not otherwise specified by northerly or southerly flows below), were assumed to be more anthropogenically influenced than either northerly or southerly flows. Northerly flows passed over Ontario or Quebec, Canada, or the North Atlantic Ocean and usually had significant passage over land. However, as was the case in CLAMS, northerly flows generally occurred at higher altitudes than westerly flows and, therefore, were less likely to be influenced by anthropogenic sources at the surface. Southerly flows passed over the eastern Gulf of Mexico, Florida or the Atlantic Ocean east of Florida. They had substantial lifetimes over water where there are few anthropogenic sources. In CLAMS, there were a few days that had backtrajectories with an easterly near-surface component. In these cases fit parameters for northerly or southerly flows were used since they too were less influenced by anthropogenic sources. Values of these fitting parameters (along with ω_0 values at a wavelength of 550 nm) are listed in Table 2.3.

(a)

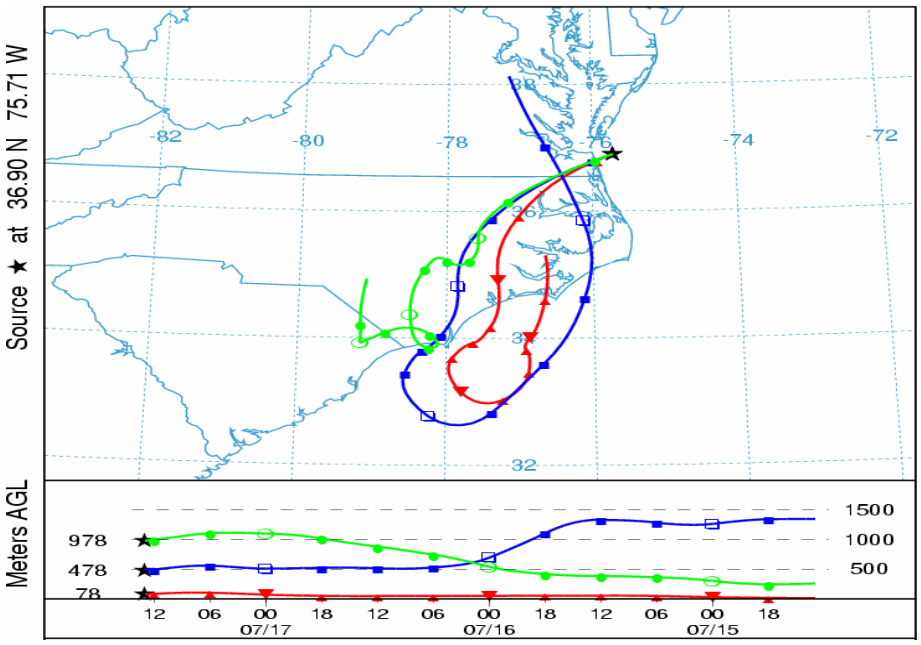

(b)

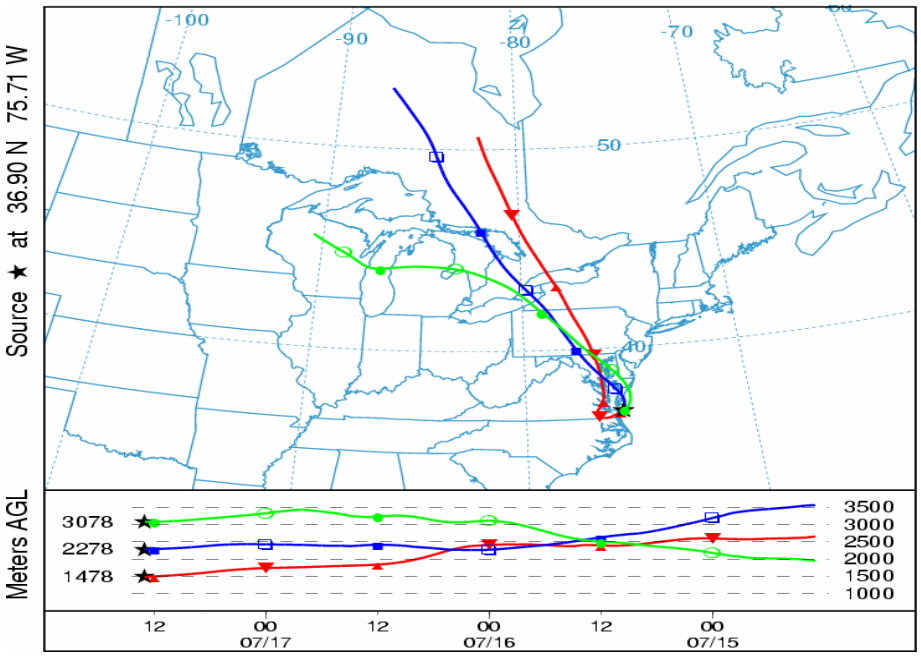

Figure 2.2 Air parcel 72 hour backtrajectories at (a) 100 m (red triangles), 500 m (blue squares) and 1000 m (green circles) MSL and (b) 1500 m (red triangles), 2300 m (blue squares) and 3100 m (green circles) MSL for July 17, 2001 over the U.S. East Coast determined with NOAA's HYSPLIT analysis tool. The star off the coast of Virginia marks the location of the Chesapeake Bay Lighthouse. Altitudes of airflow backtrajectories are listed at the bottom of each panel.

(a)

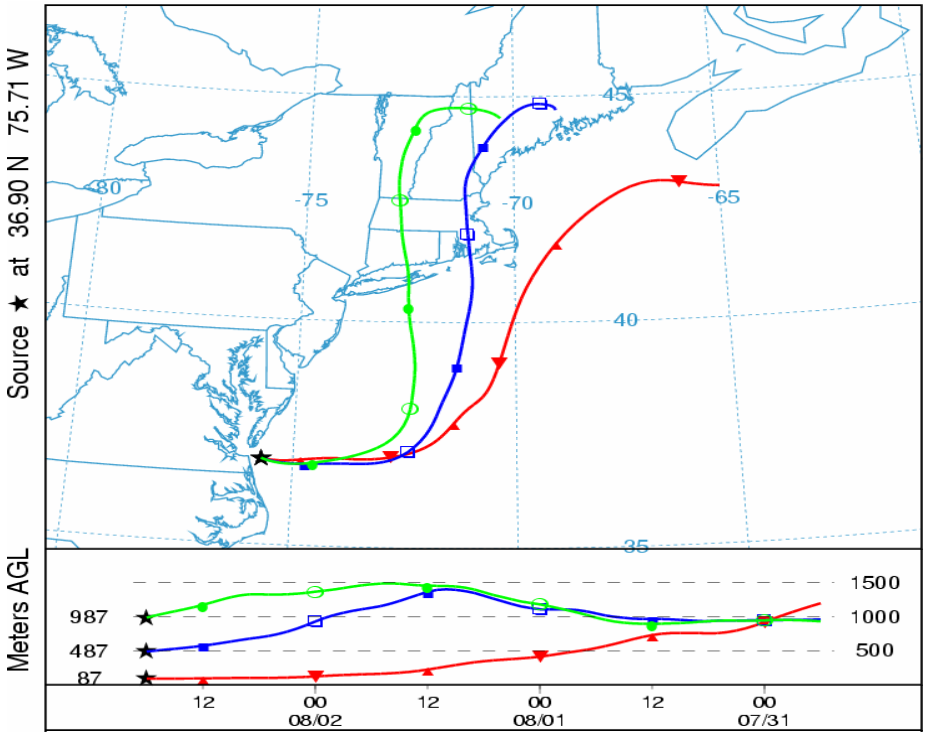

(b)

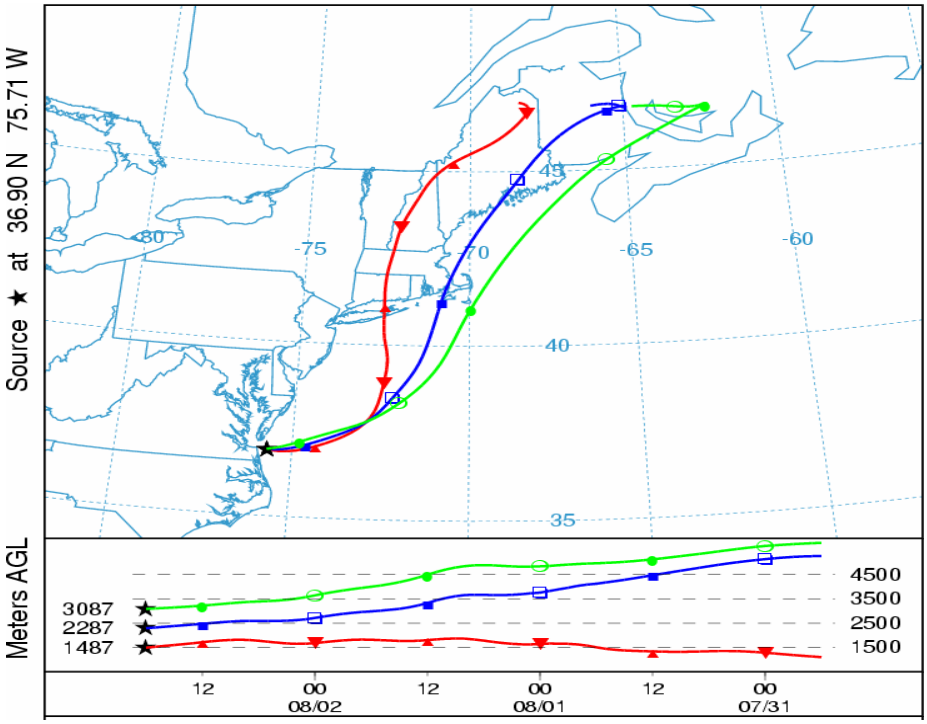

Figure 2.3 As in Figure 2.2, but for August 2, 2001.

Table 2.3 Fitting parameters "a" and "b" (derived from Kotchenruther et al. (1999)) used to correct dry light scattering coefficient values to account for hygroscopic growth; see Eqn. (4) in text. Single-scattering albedo (ω_0) values at ambient RH at a wavelength of 550 nm with one standard deviation are listed for all transects and profiles for the two Convair-580 flights of interest.

Date (2001)	**Profile**	**CV-580-derived ω_0** (mean ω_0 for entire profile)	**Transect**	**CV-580-derived ω_0** (mean ω_0 for entire transect)	**Airflow Backtrajectory**	
					Northerly/ Southerly (Easterly) a = 1.71±0.04 b = 3.41±0.16	*Westerly* a = 3.20±0.02 b = 3.78±0.04
July 17	1	0.97±0.01	A	0.95±0.01	Transects: B, C, D, E Profiles: 1(1.5-3.6 km), 2, 3 (1.5-2.1 km)	Transects: A, F, G, H, I, J Profiles: 1 (0.1-1.5 km), 3 (1.0-1.5 km), 4, 5, 6, 7, 8
	2	0.95±0.04	B	0.98±0.01		
	3	0.97±0.02	C	0.99±0.01		
	4	0.95±0.03	D	0.94±0.02		
	5	0.97±0.01	E	0.97±0.01		
	6	0.97±0.01	F	0.93±0.03		
	7	0.94±0.01	G	0.94±0.01		
	8	0.96±0.01	H	0.98±0.01		
			I	0.97±0.01		
			J	0.97±0.01		
August 2	1	0.88±0.02	A	0.91±0.03	Transects: A, B, C, D, E, F Profiles: 1, 2, 3	Transects: N/A Profiles: N/A
	2	0.93±0.03	B	0.88±0.02		
	3	0.89±0.03	C	0.89±0.02		
			D	0.94±0.01		
			E	0.93±0.01		
			F	0.92±0.04		

The nephelometer signals (photon counts) provide a relative measure of the light scattering coefficient, so that σ_{sp} can be derived only after the nephelometer has been calibrated with gases of known low and high scattering coefficients. The low span gas used for calibration purposes was standard dry air; the high span gas was CO_2. The calibration procedure is further detailed in Anderson et al. (1996). A correction was made to account for the offset, which can be thought of as photon counts due to scattering by internal surfaces (e.g., the walls of the nephelometer). These calibrations were carried

out prior to the CLAMS field campaign on April 17, 2001 and after CLAMS on October 15, 2001.

2.7 Light Absorption Coefficient (σ_{ap})

The dry aerosol light absorption coefficient, σ_{apd}, was measured at a wavelength of 567 nm (15 nm bandwidth) using a Particle and Soot Absorption Photometer (PSAP), custom-built for the UW Convair-580 by Radiance Research. This instrument compares the amount of light transmitted through a filter exposed to a sample airstream with that of an unexposed filter. The airstream to the PSAP was heated to dry the aerosol (down to ~ 30%). As discussed by Redemann et al. (2001), assuming a humidification factor of 1.00 for the light absorption coefficient, f_a, is not always acceptable. The model results by the authors suggest that maximum f_a values (at wavelengths ranging from 450 to 700 nm) range between 1.07 and 1.15 for humidification from 30 to 80% when assuming the particle is composed of a black carbon core (18% mass fraction) mixed internally with hygroscopic sulfate species forming a shell around these cores. Given the fact that ambient RH in CLAMS was, on average, significantly less than 80% (actually, 60%) and black carbon content was ≤ 4 % of the total mass fraction (Magi et al. 2005), we have used a f_a value of 1.00 in our analysis. Furthermore, as Magi et al. (2005) discuss, the value of f_a is likely to lie between 1 and f_s, where f_s is the humidification correction factor for light scattering coefficient measurements. Since $\sigma_{apd} << \sigma_{spd}$, we can assume $f_a = 1.00$, which implies $\sigma_{apd} = \sigma_{ap}$.

The PSAP provided 30 s running mean values of the light absorption coefficient of the dried aerosol, with outputs every second. An internal flow meter in the PSAP monitored the flow rate at standard temperature and pressure (STP), but the PSAP readings were adjusted to the ambient pressure and temperature. (Unfortunately, there is no documentation of a flow meter calibration prior to, during or after CLAMS; thus, the uncertainty in the flow rate cannot be accurately quantified.) The values of dry aerosol light absorption coefficient at ambient temperature and pressure were corrected for errors in sample spot size, instrument-to-instrument variability, instrument noise, and PSAP response to scattering and absorption, following the procedures described by Bond et al. (1999) and Bodhaine (1995), which implicitly account for a wavelength adjustment from 567 nm to 550 nm. The accuracy of the PSAP measurements is ~25%, with larger percentage errors at lower (i.e., $\sigma_{apd} < \sim 1.0 \times 10^{-6}$ m^{-1}) values of light absorption.

The PSAP was calibrated prior to the CLAMS field campaign (on April 17, 2001) as well as after the campaign (on October 15, 2001) by comparing PSAP measurements of absorption coefficient to the difference between independently measured values of light scattering coefficient from light extinction coefficient values (as described by Bond et al. (1999)) as measured with a nephelometer and optical extinction cell, respectively. The test aerosols were generated with a sonic jet bubbler in a solution of polyethylene glycol (non-absorbing) and small amounts of india ink (absorbing) to provide a variable absorption component. By varying the absorbing fraction of the solution, aerosols with single-scattering albedo values of 0.72 and 0.83 were generated at stable concentrations over several minutes. Primary calibrations were done using PallFlex type E70.2075W

filters, however, quartz and Teflon filters were also used. Results from both pre- and post-CLAMS calibrations showed that the PSAP was capable of providing accurate measurements of absorption coefficient over a wide range of filter loadings. Similar to the findings of Hartley et al. (2000), the instrumental uncertainty associated with σ_{apd} measurements from the PSAP was determined to be ~ 25 % given the low absorption values seen throughout CLAMS.

2.8 Particle Size Distributions

Particle size distributions were measured with a Particle Measuring Systems (PMS) Passive Cavity Aerosol Spectrometer Probe (PCASP) and a PMS Forward Scattering Spectrometer Probe (FSSP-300), both mounted under the wing of the Convair-580, as well as with a TSI Model 3320 Aerodynamic Particle Sizer (APS) located inside the aircraft (e.g., Willeke and Baron 1993). Total particle number concentrations were measured with a TSI Model 3022A condensation particle counter and a TSI Model 3025A ultrafine condensation particle counter (e.g., Alam et al. 2003), both located inside the aircraft.

2.9 Passive Cavity Aerosol Spectrometer Probe (PCASP)

The PCASP is an optical particle counter that detects single particles and sizes them by measuring the intensity of light the particles scatter when passing through a beam of light. A helium-neon laser beam is focused to a small diameter at the center of an aerodynamically focused particle-laden airstream. Particles that encounter this beam

scatter light in all directions and some of this light is collected by a mirror over angles of 35° to 120°. This collected light is focused onto a photodetector and the particle size is determined using Mie scattering theory. The PCASP sample chamber was heated throughout CLAMS, which raised the sampling temperature by 10-15° C above ambient, thereby reducing the sampling RH to less than ~30%.

The PCASP was calibrated prior to CLAMS on April 19, 2001. Non-absorbing polystyrene spheres of varying diameter (2.020, 1.530, 0.804, 0.343, 0.198, and 0.142 μm) were employed for the calibration. However, the diameter limits of the bins had to be adjusted to account for the difference between the expected aerosol refractive index and that of the calibrating polystyrene spheres (Liu et al. 1992). As Hartley et al. (2000) discuss, the channel diameter limits were corrected assuming an aerosol with a refractive index of $n = 1.46 - 0.0086i$. While the authors do not explicitly discuss uncertainty associated with the mean refractive index, n, they do state that the sensitivity of n to the assumed molecular-to-ion or molecular-to-carbon mass ratio was negligible (< 1 %). Thus, we conclude that any uncertainty associated with n would translate into a similarly negligible uncertainty in the bin size limits. As a result of this correction, the PCASP classified particles into one of fifteen size channels with diameters ranging from 0.11 to 4.52 μm. Liu et al. (1992) estimate an approximate uncertainty in the bin size limits of ± 5% when using a similar calibration procedure to the one described above. A mid-CLAMS calibration was performed on July 21, 2001 using polystyrene spheres of the same size as in the previous calibration (April 19, 2001). Results were sufficiently similar (within ~5 %) to retain the channel limit corrections already in place.

2.10 Forward Scattering Spectrometer Probe (FSSP-300)

The FSSP-300 is also an optical particle counter that determines particle size by measuring the intensity of light that a particle scatters when passing through a helium-neon laser beam. It differs from the PCASP in that the light scattered by the particles is directed through a condensing lens and onto a beam splitter. The beam splitter divides the scattered light into two components reaching different photodetectors. One of these detectors is optically masked to receive only scattered light when the particles pass through the laser beam within 0.5 mm on either side of the center of focus. This defines the sample volume needed to calculate particle concentrations. The FSSP-300 also differs from the PCASP in terms of the range of angles it samples. Light scattered by particles in the FSSP-300 are measured over angles of 4° to 12°, compared to 35° to 120° for the PCASP.

Measurements by the FSSP-300 are affected by Mie scattering, uncertainties in the index of refraction of the aerosol, non-uniform laser intensity, uncertainties in sample volume, and time response roll-off. After applying corrections for these uncertainties, as discussed by Baumgardner et al. (1992) and Kim and Boatman (1990), the uncertainties in the number concentrations reported here are ~25%.

The FSSP-300 was calibrated prior to CLAMS on May 2, 2001. Non-absorbing glass spheres (with diameters of 8.1, 15.7 and 21.9 μm) and polystyrene spheres (with diameters of 0.343 and 0.705 μm) were used in this calibration. However, the diameter limits of the channels were corrected to account for the differences in index of refraction between the encountered aerosol and that of the calibrating spheres. Using a mean RH in

CLAMS of ~60%, Table 1 in Kim and Boatman (1990) was used to determine the average index of refraction of the aerosol we sampled ($n \approx 1.47 - 0.034i$). Since the air sampled in CLAMS had both urban and marine properties, this mean value was obtained by averaging the refractive indices these authors employed for urban and maritime aerosol models, respectively. This index of refraction ($n \approx 1.47 - 0.034i$) was then used to determine channel size limits using Table 2 in Baumgardner et al. (1992). Again, as in our efforts to correct the channel size limits for the PCASP, neither Kim and Boatman (1990) nor Baumgardner et al. (1992) discuss any associated uncertainties in the refractive indices they use. Thus, we are unable to quantify the uncertainty in the correction to the bin size limits, as well. As a result, the FSSP-300 classified particles into one of thirty-one size channels with diameters ranging from 0.35 to 20.72 μm.

While the assumed aerosol refractive index used for the PCASP and FSSP-300 bin limits has an imaginary component that differs by almost an order of magnitude, any additional correction would have a small effect on the bin size limits, especially at the smaller size intervals (where the majority of particles in CLAMS were observed) since all the other previously discussed corrections resulted in relatively small changes to the bin size limits (range: 0.4-16.7 %, mean: 7.0 % change from the manufacturer's prescribed bin size limits). A mid-CLAMS calibration was performed on July 21, 2001 using glass spheres 15.7 μm in diameter and polystyrene spheres with diameters of 0.705 and 0.343 μm. Again, the results obtained were such as to retain the channel limit corrections already in place.

2.11 TSI Model 3320 Aerodynamic Particle Sizer (APS)

The TSI 3320 APS is a "time-of-flight" aerosol particle size spectrometer described by Wang et al. (2002). It measures the aerodynamic diameter of particles based on timing particle velocity between two laser beams. Because time-of-flight aerodynamic sizing accounts for particle shape and is unaffected by index of refraction, it is arguably superior to sizing by light scattering. However, the TSI 3320 APS is subject to problems such as counting "phantom" particles and recirculation, which may lead to some particles being counted more than once (Stein et al. 2002). Stein et al. (2002) state that these erroneous measurements affect measurements of particles with $D_p > 1.0$ μm. Since the TSI 3320 APS was located inside the Convair-580 (whereas the PCASP and FSSP-300 were mounted under the wing of the aircraft), channels above 1.0 μm are ignored, as discussed in Section 2.5. Thus, no correction was applied to account for the uncertainties discussed by Stein et al. (2002).

An adjustment was applied to the APS data, however. This instrument measures particle aerodynamic diameter, while the PCASP and FSSP-300 classify particles according to their optical diameter. As a result, the following correction was applied to the bin limits of the APS (Murphy et al. 2004):

$$D_{optical} = D_{aero} / (\rho)^{0.5} \quad (5)$$

where $D_{optical}$ is the optical diameter, D_{aero} the aerodynamic diameter and ρ the mean particle density, which was assumed to be 1.9 g/cm^3 based on compositional data showing a strong dominance of sulfate (Castanho et al. 2005). With this correction (and

the 1.0 μm cut-off), the TSI 3320 APS classified particles into one of fifteen channels with diameter limits ranging from 0.36 to 1.00 μm.

Since the APS was purchased only a year and a half prior to CLAMS, and was in relatively good agreement with the PCASP and the FSSP-300 measurements, it was assumed that the manufacturer's calibration was sufficient for data output from the TSI 3320 APS to be used in qualitative assessments of particle size distributions and total particle number concentrations.

2.12 TSI Model 3022A Condensation Particle Counter (CPC)

The TSI 3022A CPC was located inside the Convair-580 aircraft during CLAMS. Condensation particle counters take advantage of the fact that highly supersaturated vapor condenses onto nearly all of the particles in the air. For this particle counter, an internal pump drew the aerosol sample into the CPC. A linear-element flow meter controlled the flow volumetrically. Upon entering the instrument, the sample passed through a heated saturator, where butanol was evaporated into the air stream and saturated the flow. The aerosol sample then passed into a cooled condenser tube, where highly supersaturated vapor condenses onto nearly all of the airborne particles. This produced larger, more easily detectable droplets. The droplets were detected by a laser-diode light source and counted by an optical detector immediately after leaving the condenser. The TSI 3022A detected particles with diameters ≥ 0.007 μm and was capable of measuring concentrations up to 10^7 cm^{-3}. However, due to its location inside the aircraft, the TSI 3022A could not detect particles efficiently with $D_p > \sim 1.0$ μm. The

TSI 3022A operating manual (available at www.tsi.com/documents/1933763i-3022A.pdf) states, "In the real-time and live-time, single-particle counting modes (below 10,000 cm^{-3}), no calibration is required except for flow rate. The particle concentration is simply calculated from the flowrate, time and number of particles that pass through the sensing chamber". The flowrate was calibrated according to the operating manual prior to CLAMS, but no further calibration was necessary, since particle number concentrations in CLAMS were typically on the order of 1000 cm^{-3}.

2.13 TSI 3025A Ultrafine Condensation Particle Counter (CPC)

The TSI 3025A Ultrafine CPC was also located inside the Convair-580 during CLAMS (and, as a result, could not efficiently measure particles with $D_p > \sim 1.0$ μm). The CPC has similar operating principles to the TSI 3022A. The TSI 3025A also utilizes butanol to condense onto particles in the sample flow, creating aerosol droplets large enough to be detected using light-scattering. Due to the butanol vapor sheath, which confines the aerosol flowpath to near the centerline of the condenser, all particles experience nearly identical supersaturation conditions. The result is a nominal lower size-detection limit of 0.003 μm in diameter defined by a sigmoid counting efficiency curve ranging from 0% at about 2 nm to 100% at about 7 nm. Droplets are counted individually (in concentrations up to 10^5 cm^{-3}) as they scatter light onto a photodetector. Sensitivity to particles as small as 3 nm in diameter is important for nucleation, combustion, condensation and growth studies. A flowrate calibration of the TSI 3025A CPC was conducted according to the operating manual

(www.tsi.com/documents/1933762i-3025A.pdf) prior to CLAMS. The TSI 3025A uses a single photometric calibration point to check the overrange status of the counter in single-count mode. This calibration point, 0.5 V, was achieved accurately.

2.14 NASA Ames Airborne 14-channel Tracking Sunphotometer (AATS-14)

The AOD values discussed here were derived from measurements made by the 14-channel Ames Airborne Tracking Sunphotometer (AATS-14) aboard the Convair-580 aircraft. Redemann et al. (2005) discuss the operating principles of and methods for data reduction, calibration and error analysis applied to AATS-derived AOD data in CLAMS. In brief, the AATS-14 measures direct solar beam transmission in narrow channels by using sensors in a tracking head that can rotate about two axes. The instrument's tracking head mounts external to the aircraft skin to minimize blockage by aircraft structures and also to avoid data contamination by aircraft-window effects.

Since sunphotometers have a non-zero field of view, they measure some diffuse light in addition to the direct solar beam. As a result, uncorrected sunphotometer measurements can overestimate direct-beam transmission and, thus, wavelength-dependent AOD values. This effect is amplified as wavelength decreases and as particle size increases in the column. However, since very small particles dominated size distributions in CLAMS, Redemann et al. (2005) state that these diffuse light corrections were generally negligible. AATS-14 was calibrated prior to (in June 2001) and after (in September 2001) CLAMS at the Mauna Loa Observatory, Hawaii, using the Langley plot technique (Schmid and Wehrli 1995).

2.15 Multiangle Imaging Spectro-Radiometer (MISR)

The Multiangle Imaging Spectro-Radiometer (MISR) produces 36 simultaneous views of the Earth, in a combination of nine angles ranging from +70°, through nadir, to -70° in the along-track direction, in each of four spectral bands centered at 446, 558, 672, and 866 nm (Diner et al. 1998). It takes seven minutes for all nine MISR cameras to view a fixed, 400 km wide line on the surface, which sets the swath width and effective temporal resolution for coincident observations. At mid-latitudes, a given location is imaged about once per week in the MISR standard Global Imaging mode, providing 275 m spatial resolution data in all four nadir channels, and in the red channels, centered at a wavelength of 672 nm, of the other eight cameras. The remaining 24 channels of data are averaged on board the spacecraft to 1.1 km resolution.

The MISR aerosol retrieval algorithm compares observed, calibrated, multi-angle radiances with those simulated for a range of particle mixtures and amounts. Column, spectral optical depth and column effective aerosol mixture type are reported at 17.6 km resolution in the MISR standard aerosol product, which incorporates cloud screening and other considerations. Different algorithm approaches are used for over-land and dark-water retrievals; over land, aerosol and surface reflectance characteristics are retrieved self-consistently (Martonchik et al. 1998, 2002).

Pre-launch theoretical studies indicated that MISR spectral radiances, measured at precisely known air-mass factors ranging from 1 to 3, could provide tight constraints on aerosol column optical depths over land and water. (The air-mass factor is the ratio of the slant path from the satellite through the atmosphere to the path along the nadir view.

Said another way, the air-mass factor is $1/[\cos \phi]$, where ϕ is the zenith angle of observation.) Along with the wide range of scattering angles sampled (about 60° to 160° at mid-latitudes), MISR provides constraints on particle shape, size distribution, and to a lesser degree ω_0 values, particularly over dark, uniform ocean surfaces (Kahn et al. 1998, 2001). Generally, these studies predicted a column aerosol optical depth accuracy of at least 0.05 or 20%, whichever is larger. For good viewing conditions over ocean, this work predicted an ability to distinguish three-to-five size bins between about 0.1 and 2.5 μm diameter, two-to-four groupings of particle single-scattering albedo between about 0.8 and 1.0, and spherical particles from randomly oriented non-spherical particles, amounting to about a dozen categories of particle types. The predicted column optical depth sensitivity has been tested and verified globally (Kahn et al. 2005 and references therein), and has been analyzed in detail specifically for the CLAMS days discussed here (Redemann et al. 2005). Particle property retrieval validation is more challenging, since column-effective values of particle size distributions and single-scattering albedo values must be derived for comparison with the MISR results. The most reliable way of achieving this is to measure particle properties at multiple levels within the atmosphere and, to the degree possible, construct environmental snapshots of the entire column (e.g., Kahn et al. 2004). When utilizing such an approach with in situ aircraft data, the aerosol above the highest flight level must be accounted for in some way. Here, we determine the percent of AOD above the top flight level by using AATS measurements to account for the aerosol aloft.

CHAPTER 3

RESULTS AND DISCUSSION

3.1 General Characterization of Aerosol Properties from Airborne In Situ Measurements

The data presented herein is a summary of the optical properties and size distributions of the aerosols measured from the Convair-580 on July 17 and August 2, 2001. Coincident MISR results are available for these two days.

3.1.1 State Parameters

The hypsometric altitude of the aircraft allowed time/height cross-sections to be constructed for the July 17 (Fig. 2.1a) and August 2 (Fig. 2.1b) flights. These figures illustrate the vertical profiles and horizontal transects made by the Convair-580 on July 17 and August 2. Similar flight patterns, consisting of multiple transects (at altitudes ranging from ~0.05 to ~3.0 km MSL) and vertical profiles (covering roughly the same altitude range), were conducted during the nine other flights of the Convair-580, allowing a thorough characterization of the atmospheric aerosol in the lower troposphere. Basic meteorological parameters (temperature, RH, potential temperature and latitudinal/longitudinal variability) were derived from the measurements obtained in the vertical profiles and horizontal transects of both flights. Concentrations of O_3 and SO_2 versus altitude for all profiles and horizontal transects of both flights are available, but are not discussed here.

3.1.2 Optical Properties

The aerosol single-scattering albedo is an important input to radiative forcing calculations. The single-scattering albedo (ω_0) was determined at a wavelength of 550 nm using Eqn. (1). Figures 3.1a-b show measurements of the dry aerosol light absorption coefficient (σ_{apd}), the ambient light scattering coefficient (σ_{sp}) derived from Eqn. (4) and the ω_0 at 550 nm for the primary profile of the July 17 (Fig. 3.1a) and August 2 (Fig. 3.1b) flights. Table 2.3 shows ω_0 values at 550 nm (with one standard deviation) for all transects and profiles of both flights, as well as the air parcel backtrajectory-dependent humidification correction factors (derived by Kotchenruther et al. 1999) applied to the σ_{spd} data. The σ_{apd} measurements were not corrected for RH, since these are expected to be smaller than other uncertainties. Therefore the measured dry values of the absorption coefficient are used. The PSAP provided 30 s running means of σ_{apd} with outputs every second. Therefore, the nephelometer measurements of σ_{sp} were also averaged over 30 s with outputs every second. The effect of this averaging on spatial resolution is discussed in Section 3.3.1.

After applying the corrections discussed in Sections 2.6 and 2.7, and when the air was quite clean, the values of scattering and/or absorption sometimes bordered on the detection limit of the instruments (i.e., the signal to noise ratio decreased dramatically). In these cases (usually at altitudes > 2-3 km), the σ_{apd} values often exceeded the σ_{sp} values. Castanho et al. (2005) state that the black carbon (i.e., absorbing) content of the aerosol measured in CLAMS accounted for 3 ± 1% of those particles with $D_p < 2.5$ μm. In view of the relatively low concentrations of absorbing aerosol, ω_0 values

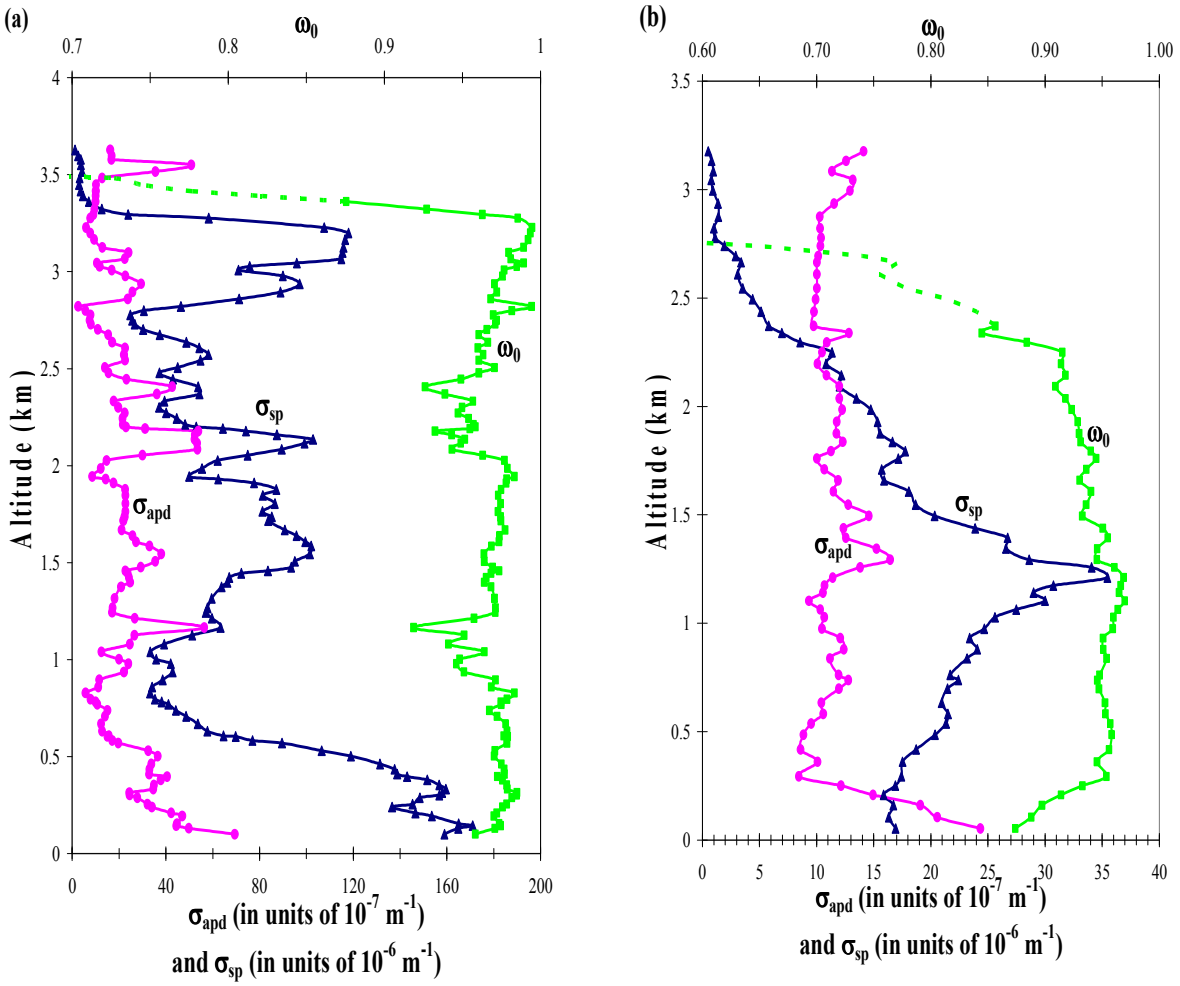

Figure 3.1 Vertical profiles of σ_{apd} (magenta), σ_{sp} (navy), and ω_0 (green) at a wavelength of 550 nm for (a) aircraft profile #1 of the July 17, 2001 flight and (b) aircraft profile #2 of the August 2, 2001 flight. The dotted line in the single-scattering albedo (ω_0) profiles represent values of ω_0 that are less than 0.85; we have much less confidence in these values since both σ_{sp} and σ_{apd} values were so low at these altitudes (see Section 3.1.b). Uncertainties associated with these parameters are discussed in Sections 2.6-2.7.

were unlikely to have been below 0.85 at altitudes lower than 2-3 km. Therefore, we ignored values of absorption coefficient < 3.0 x 10^{-6} m^{-1} when scattering coefficient values were < 17.0 x 10^{-6} m^{-1}; these limits correspond to an aerosol single-scattering albedo of 0.85 and 550 nm (Magi et al. 2005). The sharp decrease in ω_0 at high altitudes

is illustrated in profile #1 on July 17 (Fig. 3.1a) and in profile #2 on August 2 (Fig. 3.1b) by a dashed green line. It should be pointed out that it is possible that ω_0 values < 0.85 exist for the aerosol aloft (i.e., > 2-3 km). However, the signal for both σ_{sp} and σ_{apd} (and particle number concentration, see Fig. 3.8) was quite low and/or began to decrease dramatically at these altitudes and, therefore, we do not have confidence in the accuracy of these measurements and the subsequent derived ω_0 values.

Figure 3.1 captures the key features seen in profiles not presented here. For example, haze layers are evident where there is a sharp increase in the σ_{sp} profile (e.g., at ~0.3 km in Fig. 3.1a and at ~1.2 km in Fig. 3.1b). In Fig. 3.1a low aerosol loadings are present at ~1.0 km and ~2.8 km, where both σ_{apd} and σ_{sp} are relatively small. The sharp fall-off in σ_{sp} (and RH) seen in some profiles at higher altitudes (e.g., at altitudes > 0.5 km in Fig. 3.1a) marks the base of the free troposphere. Another interesting feature can be seen in Fig. 3.1b where the scattering coefficient halves between ~1.5 and ~2.25 km, the absorption coefficient changes by no more than 30%, but ω_0 changes little over this altitude range because it is already so close to unity.

It is noteworthy that some, but not all, of the profiles (including those in Fig. 3.1) show ω_0 decreasing with height, in particular at altitudes above 2-3 km MSL. This could be due to the typically decreasing RH with altitude and/or an increase in the relative amounts of carbonaceous to sulfate compounds with altitude, as suggested by Novakov et al. (1997). The values of ω_0 on August 2 are lower than on July 17 (see Table 2.3), indicating that the aerosol was more absorbing on August 2. A possible cause of this is that two very different air samples were studied on these days. As the air parcel

backtrajectories (Fig. 2.2 and 2.3) show, the airflow at the surface was from the south and from the northwest aloft on July 17. On August 2, the airflow was easterly/northeasterly at all level up to ~3.0 km. This difference in the amount of absorbing aerosol is supported by results from Magi et al. (2005), who found there was a general trend of increasing carbon fraction with height for both July 17 and August 2, as well as higher total carbon fraction on August 2. This latter result is particularly interesting, since the total column AOD values (at 525 nm) were significantly lower on August 2 (0.09) than on July 17 (0.41). However, the total carbon concentration (and mass concentration) on July 17 was 2-3 times greater than on August 2 (Magi et al. 2005). This is also shown implicitly by the differing magnitudes of the x-axes in Fig. 3.1 (i.e., higher σ_{apd} and total extinction values on July 17 than on August 2). Thus, we expect lower ω_0 values on August 2 (because of the higher *fraction* of absorbing aerosol), even though there was significantly more light extinction on July 17.

3.1.3 Particle Size Distributions

Particle size distributions are illustrated here in three ways: distributions of particle number, $dN/d(\log D_p)$; distributions of particle surface area, $dS/d(\log D_p)$; and distributions of particle volume, $dV/d(\log D_p)$, where D_p is the aerosol diameter, dN the total number concentration of aerosol with diameters $\geq D_p$ and $\leq D_p + dD_p$, dS the total surface area of aerosol with diameters $\geq D_p$ and $\leq D_p + dD_p$, and dV the total volume of aerosol with diameters $\geq D_p$ and $\leq D_p + dD_p$. Particle size distributions are presented here for various layers from the flights on July 17 and August 2. Plots represent time-

averaged size distributions over the course of the individual transects comprising each layer.

Recall that in order to provide the most useful results for comparisons of MISR retrievals with our airborne in situ measurements, as close to a total column characterization as possible is needed. To obtain the most representative total column particle size distributions from our aircraft data, a "layer analysis" was used. The vertical profiles flown in CLAMS do not produce reliable particle size distribution data from the PCASP or FSSP-300 measurements, since the pitch angle of the Convair-580 in these profiles affected the flow of particles through these instruments. Consequently, we divided the July 17 and August 2 flights into layers represented by various horizontal transects. For the July 17 flight, we grouped transects to define layers as follows (recall Fig. 2.1a): a) sea level to 0.5 km MSL (transects H and I); b) 0.5-1.0 km MSL (transects A and F); c) 1.0-2.0 km MSL (transects D, G and J); and, d) 2.0-3.0 km MSL (transects B, C and E). Similarly, the August 2 flight was divided into the following layers (recall Fig. 2.1b): a) sea level to 0.5 km MSL (transects B and C); b) 0.5-1.0 km MSL (transect F); c) 1.0-1.5 km MSL (transects D and E); and, d) 1.5-2.0 km MSL (transect A). Since this approach may have masked a large atmospheric variability factor, we will analyze the small-scale horizontal variability of the derived size parameters in Section 3.3.3.

The size distribution of tropospheric aerosols is usually characterized by three modes: the nucleation ($0.001\ \mu m < D_p < 0.1\ \mu m$), the accumulation ($0.1\ \mu m < D_p < 1.0\ \mu m$), and the coarse particle ($D_p > 1.0\ \mu m$), which can be used to describe a mix of airmass types, such as polar, maritime, continental, and urban (Jaenicke 1993). The

accumulation and coarse particle modes are evident in the particle size distributions shown here. However, the instruments employed in this study were unable to measure size distributions for the nucleation mode.

Castanho et al. (2005) discuss the main sources of accumulation and coarse mode particles in CLAMS based on filter measurements made aboard the Convair-580 and from surface sites. For the majority of flights, the main contribution to particle composition was from sulfate, although there were some days (most notably July 24-26) when airflow backtrajectories indicated long range transport of Saharan dust to the site of our measurements.

The particle number, surface area and volume distribution plots shown here contain log-normal curves fitted to the PCASP and FSSP-300 data based on calculated values of D_g (the geometric mean diameter), D_{smd}(the surface median diameter), or D_{vmd} (the volume median diameter), depending on whether the figure is a number, surface or volume size distribution, respectively and σ_g, the geometric standard deviation (Reist 1993). For a log-normal distribution, a geometric standard deviation of 2 indicates that 67% of the values fall within a factor of 2 of the geometric mean. Several authors have discussed the applicability of a log-normal distribution to describe aerosol size distributions (e.g., Hoppel et al. 1994; Reid and Hobbs 1998). Since the use of log-normal curves to approximate aerosol distributions has been widely used, they are employed here.

The curve representing the PCASP data is bimodal, indicating the presence of an accumulation mode and a coarse mode. For PCASP data, the accumulation mode covers

a range of particle diameters from 0.11 to 1.00 μm, while the coarse mode covers particles with diameters from 1.00 to 4.52 μm. The FSSP-300 did not detect particles small enough to fully capture the accumulation mode. As a result, the log-normal curve was determined only for the coarse mode, defined as particle diameters ranging from 0.92 to 4.33 μm. While these coarse mode bin limits for the PCASP and FSSP-300 are not exactly the same, they represent the closest particle diameter ranges given the bin limits of each instrument. The detection limits of the TSI 3320 APS prevented either the accumulation or the coarse particle modes from being captured fully. In all cases, the log-normal distributions for number, surface and volume were determined using (Seinfeld and Pandis 1998; Makela et al. 2000):

$$dN_{fit}/d(\log D_p) = \left[\sum\left(n_i/(2\pi)^{0.5}\log(\sigma_{g,i})\right)\right] \exp\left[-\left(\log(D_p)-\log(D_{g,i})\right)^2/\left(2\log^2(\sigma_{g,i})\right)\right] \quad (6)$$

$$dS_{fit}/d(\log D_p) = \left[\sum\left(\pi D_p^{\,2} n_i/(2\pi)^{0.5}\log(\sigma_{g,i})\right)\right] \exp\left[-\left(\log(D_p)-\log(D_{smd,i})\right)^2/\left(2\log^2(\sigma_{g,i})\right)\right] \quad (7)$$

$$dV_{fit}/d(\log D_p) = \left[\sum\left(\pi D_p^{\,3} n_i/6(2\pi)^{0.5}\log(\sigma_{g,i})\right)\right] \exp\left[-\left(\log(D_p)-\log(D_{vmd,i})\right)^2/\left(2\log^2(\sigma_{g,i})\right)\right] \quad (8)$$

where the summation is taken for all bins in mode i, D_p is the particle diameter, and n_i the total number concentration of particles in mode i. Table 3.1 shows the particle size distribution results for each transect of both flights. Table 3.2 lists the particle size

distribution results for each layer of the July 17 and August 2 flights, as well as for the "total layer mean", which was derived by weighting the component layers by their respective AOD values. As will be discussed in Section 3.3.3, comparison of the values in Table 3.1 with those in Table 3.2 reveals any spatial variability introduced by averaging the various horizontal transects into a layer. However, there is little variability in the derived accumulation mode microphysical parameters when using this approach.

The effective particle radius (r_{eff}) of the particle size distribution was calculated with accumulation mode PCASP data using (van de Hulst 1981):

$$r_{eff} = \left[\sum\left(r_p^3 n_i\right)\right] \Big/ \left[\sum\left(r_p^2 n_i\right)\right] \tag{9}$$

where the summation is taken over all bins in the mode i, and r_p is the particle radius. Values of effective radius using Convair-580 data are listed in Table 3.1 (for each transect of the July 17 and August 2, 2001 flights) and in Table 3.2 (for the layers of both flights). Like the total layer mean values of D_g, D_{smd} and D_{vmd}, the total layer mean values of r_{eff} were calculated by weighting the component transects by their respective AOD values. The r_{eff} values (as well as the other accumulation mode size parameters) shown in Tables 3.1 and 3.2 show a general trend of slightly larger particles on July 17 than on August 2. This is possibly attributable to the airparcel backtrajectories on July 17. At lower levels, the air had previously recirculated around the region of study for several days, allowing small particles to grow larger by condensation of trace atmospheric gases and coagulation with other particles.

3.1.3.1 Particle Number Size Distributions

Particle number size distributions show the number of particles per cm^3 of air having diameters in the range D_p to $D_p + dD_p$. The magnitude of number size distributions can yield information regarding the expected aerosol loading, or AOD. Figures 3.2a-e show particle number size distributions for the four layers, as well as the total layer mean, for the July 17 flight. A consistent accumulation mode can be seen in the PCASP data (which has a lower detection limit than the FSSP-300 or TSI 3320 APS) at $D_g \approx 0.20$ μm in all the analyzed layers. These peaks are primarily due to the growth of Aitken nuclei by coagulation into larger particles that have long residence times (e.g., Covert et al. 1996; Birmili et al. 2001). The FSSP-300 results show a consistent coarse mode at $D_g \approx 2.0$ μm can be seen at all layers up to 2.0 km (Fig. 3.2d), where the coarse mode D_g shifts to a slightly smaller value of ~1.4 μm. However, the PCASP coarse mode data do not fit a log-normal distribution as well as the FSSP-300 data, even though both instruments were mounted under the wing of the aircraft and provided simultaneous measurements. Despite these differences, the coarse mode D_g values agree quite well, showing a general trend of decreasing D_g with height and a total layer mean D_g value of ~1.80 μm.

Table 3.1 Particle geometric median diameter (D_g), surface median diameter (D_{smd}), volume median diameter (D_{vmd}), geometric standard deviation (σ_g), effective particle radius (r_{eff}), and total particle number concentration (N) for each transect of the July 17 and August 2 flights. Accumulation mode D_g, D_{smd}, D_{vmd} and σ_g values were derived using PCASP data, whereas coarse-mode values were derived with both PCASP and FSSP-300 data. The PCASP value is listed atop the FSSP-300 value for the coarse mode of each transect. Particle number concentration, as measured by the TSI 3025A particle counter, is listed (with one standard deviation) since the TSI 3025A can detect the smallest (and, therefore, majority of) particles. Some of the standard deviations associated with N are very large. This is due to strong, localized enhancements within the transect.

Date (2001)	**Transect**	**D_g (μm)**		**D_{smd} (μm)**		**D_{vmd} (μm)**		**σ_g**		**r_{eff} (μm)**	**N (cm^{-3})**
		Accum.	Coarse	Accum.	Coarse	Accum.	Coarse	Accum.	Coarse		
		PCASP	PCASP FSSP-300	PCASP	PCASP FSSP-300	PCASP	PCASP FSSP-300	PCASP	PCASP FSSP-300		
July 17 "Golden Day"	A	0.19	1.82 2.03	0.24	2.66 2.32	0.27	3.08 2.47	1.38	1.53 1.29	0.13	4522 ± 1491
	B	0.22	1.61 1.41	0.30	2.52 1.71	0.34	3.04 1.97	1.48	1.59 1.38	0.16	2101 ± 255
	C	0.22	1.51 1.40	0.30	2.26 1.62	0.35	2.79 1.81	1.50	1.57 1.33	0.16	2042 ± 279
	D	0.20	1.86 1.90	0.25	2.81 2.49	0.28	3.21 2.78	1.40	1.55 1.44	0.13	2529 ± 694
	E	0.20	1.84 1.90	0.26	2.77 2.46	0.29	3.20 2.74	1.41	1.55 1.43	0.14	3129 ± 187
	F	0.19	1.82 1.99	0.23	2.74 2.36	0.26	3.19 2.56	1.37	1.56 1.34	0.12	2428 ± 1178
	G	0.19	1.82 2.03	0.23	2.72 2.46	0.26	3.15 2.67	1.37	1.55 1.36	0.12	3433 ± 889
	H	0.20	1.80 1.95	0.26	2.66 2.46	0.28	3.08 2.71	1.40	1.54 1.40	0.13	6824 ± 919
	I	0.21	1.89 1.96	0.27	2.77 2.37	0.30	3.15 2.59	1.43	1.53 1.36	0.14	13723 ± 4750
	J	0.21	1.91 1.95	0.27	2.78 2.37	0.30	3.17 2.60	1.42	1.53 1.37	0.14	23273 ± 24143

Table 3.1 (continued)

Date (2001)	Transect	D_g (μm)		D_{smd} (μm)		D_{vmd} (μm)		σ_g		r_{eff} (μm)	N (cm^{-3})
		Accum.	Coarse	Accum.	Coarse	Accum.	Coarse	Accum.	Coarse		
		PCASP	PCASP FSSP-300	PCASP	PCASP FSSP-300	PCASP	PCASP FSSP-300	PCASP	PCASP FSSP-300		
August 2	A	0.20	1.71 2.05	0.25	2.50 2.54	0.28	2.93 2.77	1.36	1.54 1.38	0.13	1431 ± 423
	B	0.18	1.69 1.97	0.22	2.25 2.55	0.25	2.60 2.82	1.34	1.46 1.42	0.12	4981 ± 693
	C	0.17	1.71 1.98	0.21	2.42 2.54	0.25	2.85 2.79	1.34	1.52 1.41	0.11	5786 ± 675
	D	0.18	1.85 2.01	0.23	2.69 2.52	0.26	3.09 2.75	1.37	1.53 1.39	0.12	3534 ± 227
	E	0.18	1.79 1.97	0.23	2.63 2.49	0.26	3.05 2.74	1.36	1.54 1.40	0.12	3087 ± 480
	F	0.18	1.83 2.00	0.22	2.67 2.53	0.25	3.08 2.78	1.35	1.53 1.40	0.12	2010 ± 259

Table 3.2 As in Table 3.1 but for each of the previously defined layers for the July 17 and August 2, 2001 flights.

Date (2001)	**Layer (km MSL)**	**D_g (μm)**		**D_{smd} (μm)**		**D_{vmd} (μm)**		**σ_g**		**r_{eff} (μm) [MISR total column mean r_{eff}]**	**N (cm^{-3})**
		Accum. PCASP	Coarse PCASP FSSP-300	Accum. PCASP	Coarse PCASP FSSP-300	Accum. PCASP	Coarse PCASP FSSP-300	Accum. PCASP	Coarse PCASP FSSP-300		
July 17 "Golden Day"	0.0-0.5	0.21	1.86 1.95	0.26	2.73 2.41	0.29	3.13 2.64	1.42	1.53 1.38	0.14	11310 ± 5079
	0.5-1.0	0.19	1.82 2.01	0.23	2.71 2.34	0.26	3.15 2.52	1.37	1.55 1.32	0.12	3529 ± 1709
	1.0-2.0	0.20	1.88 1.96	0.26	2.77 2.41	0.29	3.17 2.64	1.41	1.54 1.38	0.14	10767 ± 14465
	2.0-3.0	0.21	1.63 1.43	0.29	2.52 1.76	0.33	3.02 2.03	1.47	1.59 1.39	0.15	2333 ± 518
	Layer Mean	**0.21**	**1.84 1.80**	**0.26**	**2.73 2.29**	**0.29**	**3.13 2.55**	**1.42**	**1.54 1.41**	**0.14 [0.12]**	**6955 ± 8899**
August 2	0.0-0.5	0.18	1.70 1.98	0.22	2.34 2.55	0.25	2.74 2.80	1.34	1.49 1.42	0.12	5375 ± 794
	0.5-1.0	0.18	1.83 2.00	0.22	2.67 2.53	0.25	3.08 2.78	1.35	1.53 1.40	0.12	2010 ± 259
	1.0-1.5	0.18	1.81 1.98	0.23	2.65 2.50	0.26	3.07 2.74	1.37	1.53 1.40	0.12	3221 ± 468
	1.5-2.0	0.20	1.71 2.05	0.25	2.50 2.54	0.28	2.93 2.77	1.36	1.54 1.38	0.13	1431 ± 423
	Layer Mean	**0.18**	**1.78 1.99**	**0.22**	**2.57 2.53**	**0.25**	**2.99 2.78**	**1.36**	**1.53 1.41**	**0.12 [0.12]**	**3006 ± 1551**

It should also be noted that there is generally good agreement among the two optical particle sizers (the PCASP and FSSP-300) in the 0.4-1.0 μm diameter range, where incident sunlight scattering is most efficient, and therefore most important. However, the TSI 3320 APS results do not agree as well, especially in the smaller particle diameter range. This could possibly be attributable to three factors. First, the APS counting efficiency drops to << 1 for particles $D_{optical} < \sim 0.5$ μm. Second, the TSI 3320 APS is an aerodynamic particle sizer, so it utilizes different operating principles than the PCASP or FSSP-300. As a result, one might expect the PCASP and FSSP-300 sizers, which both use an optical technique to size particles, to yield measurements which are more similar. Third, the TSI 3320 APS was located inside the aircraft, while the PCASP and FSSP-300 were located under the wing of the aircraft. McMurry (2000) states that inlet losses during aircraft sampling of super-μm particles can be as high as 50-90%, while Huebert et al. (1990) found that underestimates of ambient values of submicron particles due to inlet losses may be as great as a factor of 2-10. While we acknowledge losses may be this great for the TSI 3320 APS (and the TSI 3022A and 3025A particle counters, which were all located inside the aircraft), a laminar flow device was employed in front of the PCASP and FSSP-300 which likely kept particle losses on the lower end of these ranges. There is also minimal variability in the magnitude of the number size distributions with height, indicating a well-mixed lower troposphere.

Figures 3.3a-e show the particle number size distributions for the four layers, as well as the total layer mean, for the August 2, 2001 flight.

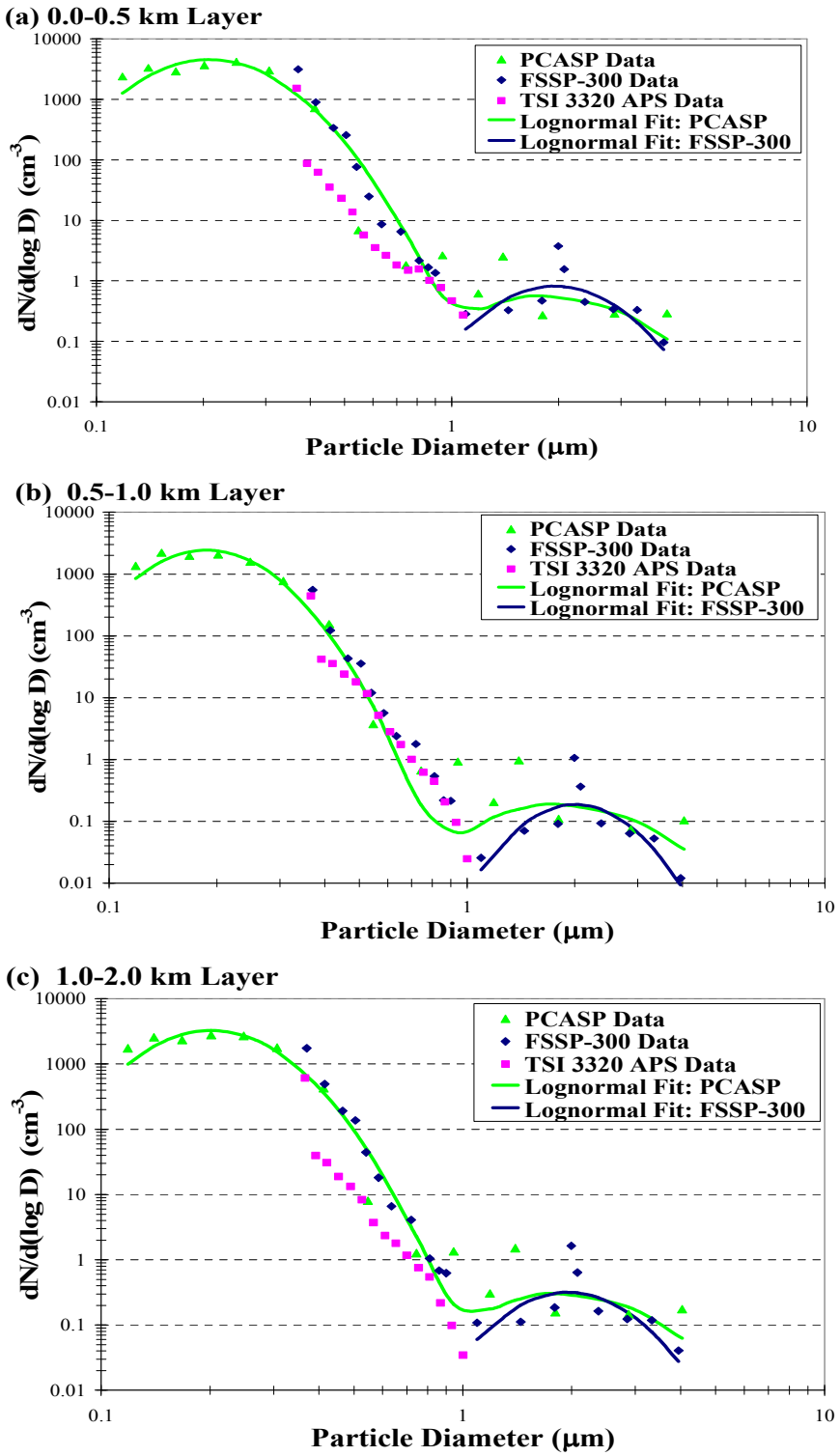

Figure 3.2 Particle number size distributions for the four layers and total layer mean of the July 17, 2001 flight. Uncertainties associated with the measured particle number concentration from the three particle sizers are discussed in Section 3.1.3.1.

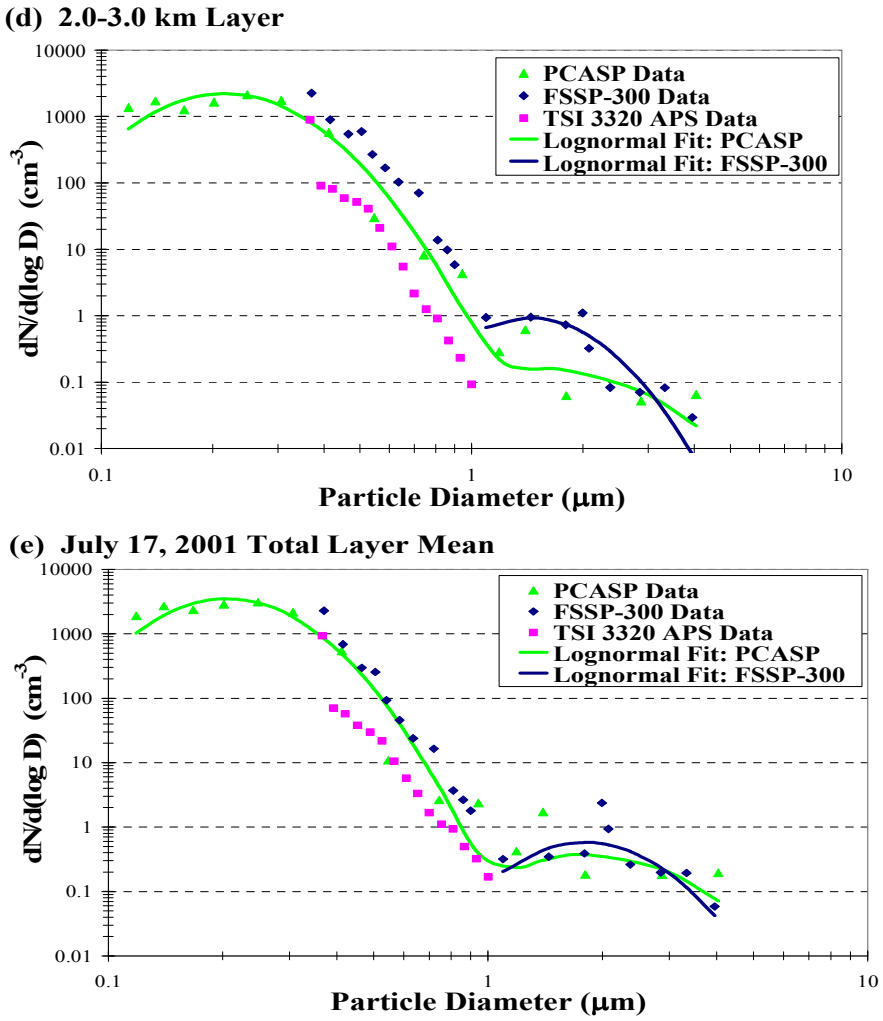

Figure 3.2 (continued)

Similar to the number size distribution plots for the July 17 flight, a consistent accumulation mode is seen at $D_g \approx 0.20$ µm in all layers. There is a sudden drop off in the TSI 3320 APS data, which is likely due to this instrument being located inside the aircraft and the inlet tubes preventing particles with diameters much larger than ~1.0 µm from entering the instrument (this was also seen in the July 17 data). The coarse mode D_g is again at ~2.0 µm for all layers up to 2.0 km. There are also displacements of the

PCASP and FSSP-300 data beyond $D_p \approx 1.0$ μm, possibly due to the assumptions made in correcting the channel limits (i.e., index of refraction estimations).

There appears to be a more pronounced trend of decreasing contributions from coarse mode particles with increasing height to the number size distribution on August 2 than there was on July 17. This is likely attributable to large sea salt particles that settle out at low altitudes; the lower troposphere was not as well-mixed on this day as it was on July 17. This is supported by near-surface wind speed measurements made aboard the Convair-580, as well as data acquired from the Chesapeake Lighthouse. The mean near-surface wind speed on July 17 was 5.5 ± 2.1 m s^{-1} from the Convair-580 measurements, while mean surface winds of 8.2 ± 2.2 m s^{-1} were measured at the lighthouse. Comparing these values with those measured on August 2 (Convair-580: 3.7 ± 1.2 m s^{-1} and lighthouse: 4.4 ± 1.1 m s^{-1}), we see that significantly stronger surface winds were present on July 17, supporting our conclusion that more sea salt particles were present in the lowest layer of the troposphere on July 17.

Recall that the magnitude of the particle number size distributions can provide a measure of the aerosol loading. Thus, in comparing the number size distributions for both days, it can be seen that the aerosol loading on August 2 was significantly lower than on July 17. The AATS results support this, yielding total column AOD values (at a wavelength of 525 nm) for July 17 and August 2 of 0.40 and 0.10, respectively.

It should be noted that in Fig.s 3.2-3.3 there is an interesting feature in the FSSP-300 coarse mode data; there are two data points that lie above the coarse mode curve with the left point above the right by roughly the same amount. A possible cause of this

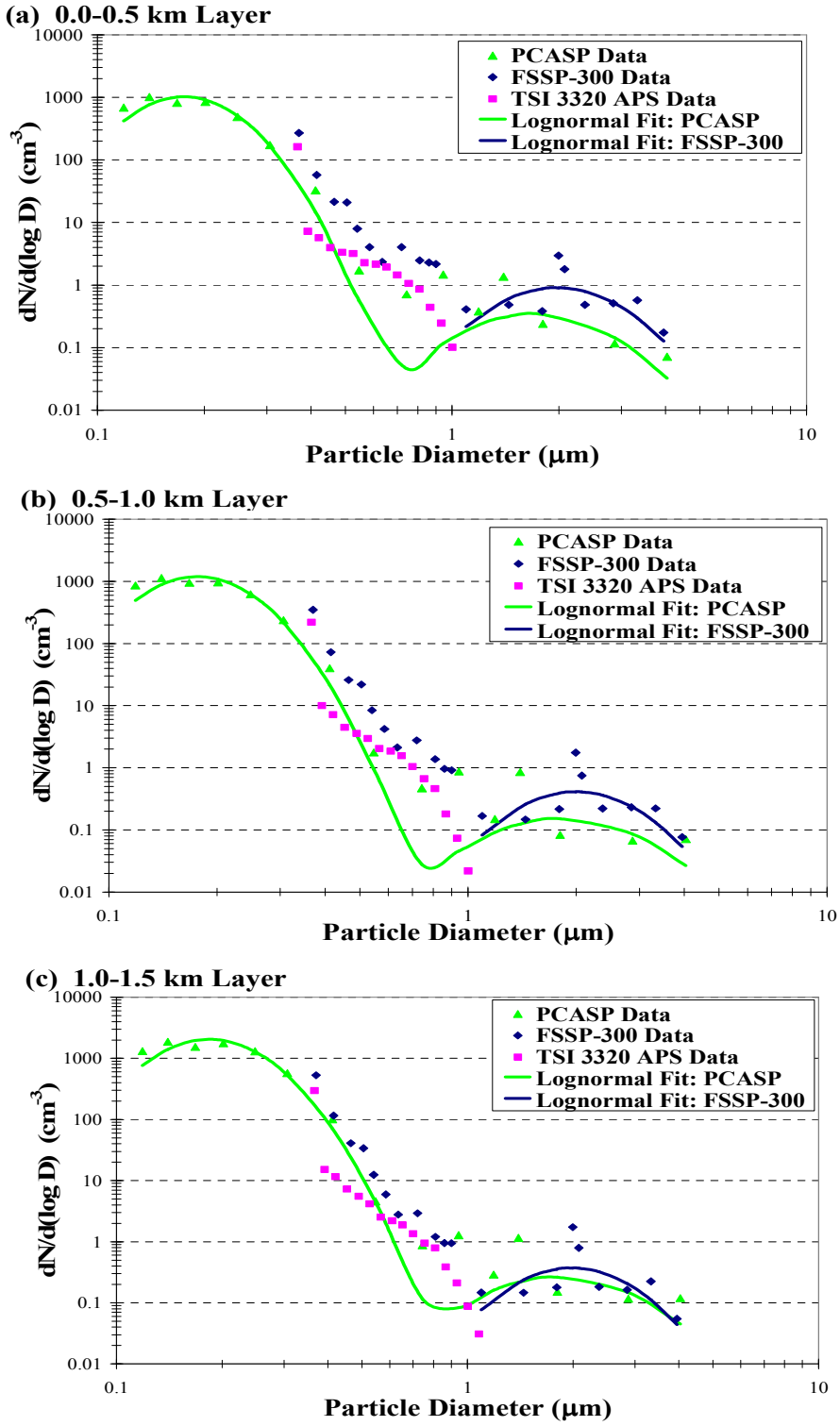

Figure 3.3 Particle number size distributions for the four layers and total layer mean of the August 2, 2001 flight. Uncertainties associated with the measured particle number concentration from the three particle sizers are discussed in Section 3.1.3.1.

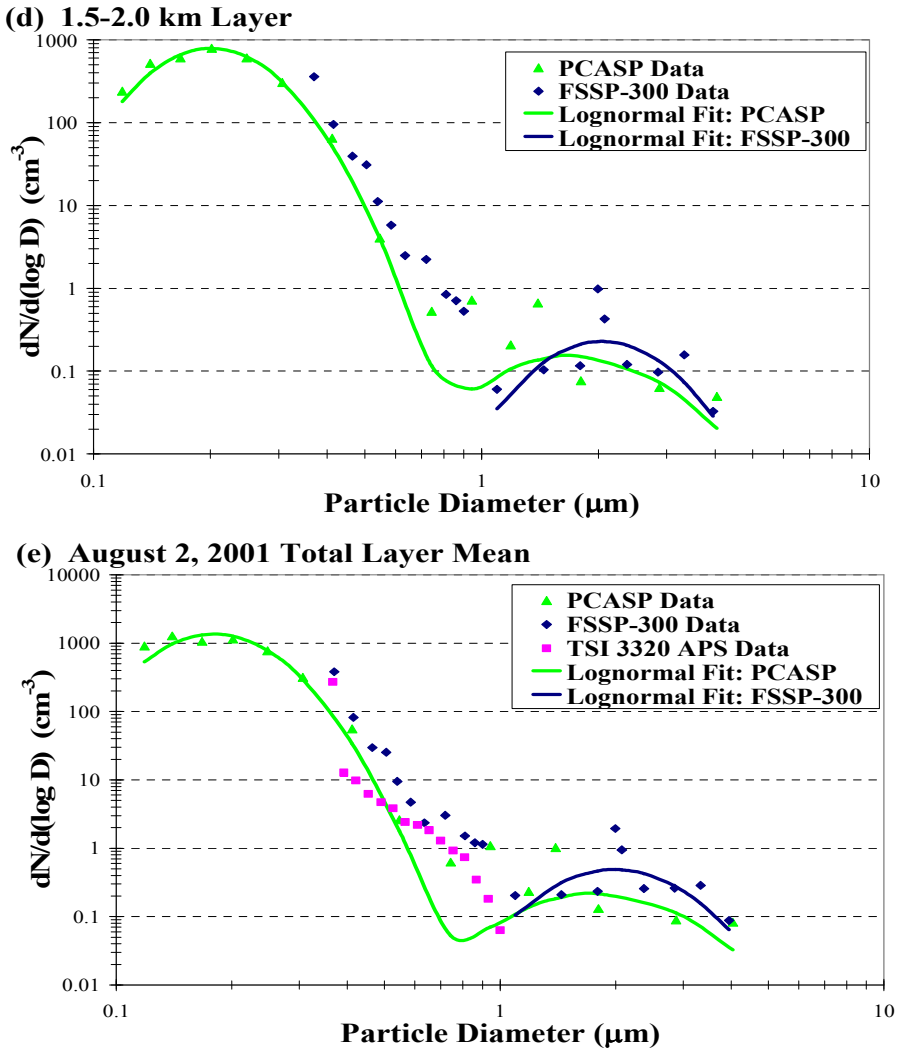

Figure 3.3 (continued)

anomalous looking feature is the fact that the bin size limits we used from Table 2 of Baumgardner et al. (1990) actually list the same size limits for the three bins to the left and the three bins to the right of this distinct feature. In post-analysis, we have subdivided these bin ranges, hence there is very little variation in the magnitude of the three points to the left and right of this "spike" in the FSSP-300 coarse mode data. Furthermore, these coarse mode particles were extremely low in terms of number concentration and, as will be discussed in Section 3.3.3, much of this data is likely to be

instrument noise. Still, we find it of some use to present this data as well as the derived coarse mode size parameters as a means of describing, as fully as possible, the aerosol properties on these two days.

Table 3.3 lists the correlation coefficients, R^2, for the nonlinear regressions between the log-normal curves and the PCASP, FSSP-300 results for the number size distributions on the July 17 and August 2 flights. If the R^2 value is greater than, say, 0.75 we can conclude that the log-normal curve does a good job in representing the results from that particular optical particle sizer and, thus, the aerosol in that mode are log-normally distributed. The R^2 values in Table 3.3 indicate that the accumulation mode particles certainly appear to be log-normally distributed. However, the coarse mode particles do not exhibit such a distribution.

Table 3.3 The R^2 values for nonlinear correlations between (accumulation and coarse mode) log-normal curves and PCASP, FSSP-300 results for the number size distributions. Values of R^2 that are > ~0.75 indicate that the log-normal curve does a good job in representing the results as determined from PCASP and FSSP-300 measurements.

Flight Date	Layer	Accumulation Mode	Coarse Mode	
			PCASP	FSSP-300
July 17, 2001	0.0-0.5 km	0.8623	0.0891	0.3544
	0.5-1.0 km	0.9032	0.1256	0.3634
	1.0-2.0 km	0.8936	0.0733	0.3399
	2.0-3.0 km	0.7863	0.2864	0.7541
	Total Layer Mean	0.8611	0.1188	0.3332
August 2, 2001	0.0-0.5 km	0.8893	0.3082	0.3486
	0.5-1.0 km	0.8797	0.1236	0.3249
	1.0-1.5 km	0.8796	0.1398	0.3243
	1.5-2.0 km	0.9738	0.2337	0.34
	Total Layer Mean	0.8922	0.1968	0.339

3.1.3.2 Particle Surface Area Distributions

The differences between aerosol samples can be highlighted by comparing the contributions of given size intervals to the total particulate surface area or volume, rather than to the total number of particles (e.g., Rogers and Yau 1989). Particle surface area distributions show the total surface area of particles per cm^3 of air having diameters in the range D_p to $D_p + dD_p$. The value of D_{smd} is larger than D_g by a factor of $\exp[2\ln^2(\sigma_g)]$ and, as a result, regions of the number distribution data where discrepancies exist among the three particle detectors are enhanced in the surface area distribution plots. The surface area of the particles was derived from measured values of D_p assuming that the particles are spherical. The magnitude of the particle surface area distribution provides information about the expected light extinction (since light scattering and absorption are related to the size and surface area of atmospheric particles). Figures 3.4a-e show particle surface area distributions for the four layers and the total layer mean of the July 17 flight. Figures 3.5a-e show the surface area distributions for the four layers and the total layer mean of the August 2 flight. In general, there is a much larger contribution from coarse mode particles to the surface area distributions than to the number size distributions. An accumulation mode centered around $D_{smd} \approx 0.25$ μm and a median value of coarse mode $D_{smd} \approx 2.50$ μm can be seen in all layers on both flights.

The particle surface area distributions on July 17 show that the accumulation mode aerosols dominated the total particle surface area for all layers analyzed. Furthermore, the majority of particle surface area was contained within the lowest layer of the troposphere, as seen in Fig. 3.4a where the magnitude of both the accumulation and

coarse modes are greater than those in higher layers. The unique distribution of the particle coarse mode FSSP-300 data in the highest layer (2.0-3.0 km MSL; Fig. 3.4d) skews the coarse mode D_{smd} to a smaller value of ~1.75 μm, while coarse mode FSSP-300 data at lower levels indicates a consistent D_{smd} value of ~2.4 μm. The values of D_{smd}, as determined by PCASP and FSSP-300 coarse mode data, agree fairly well, especially at lower altitudes.

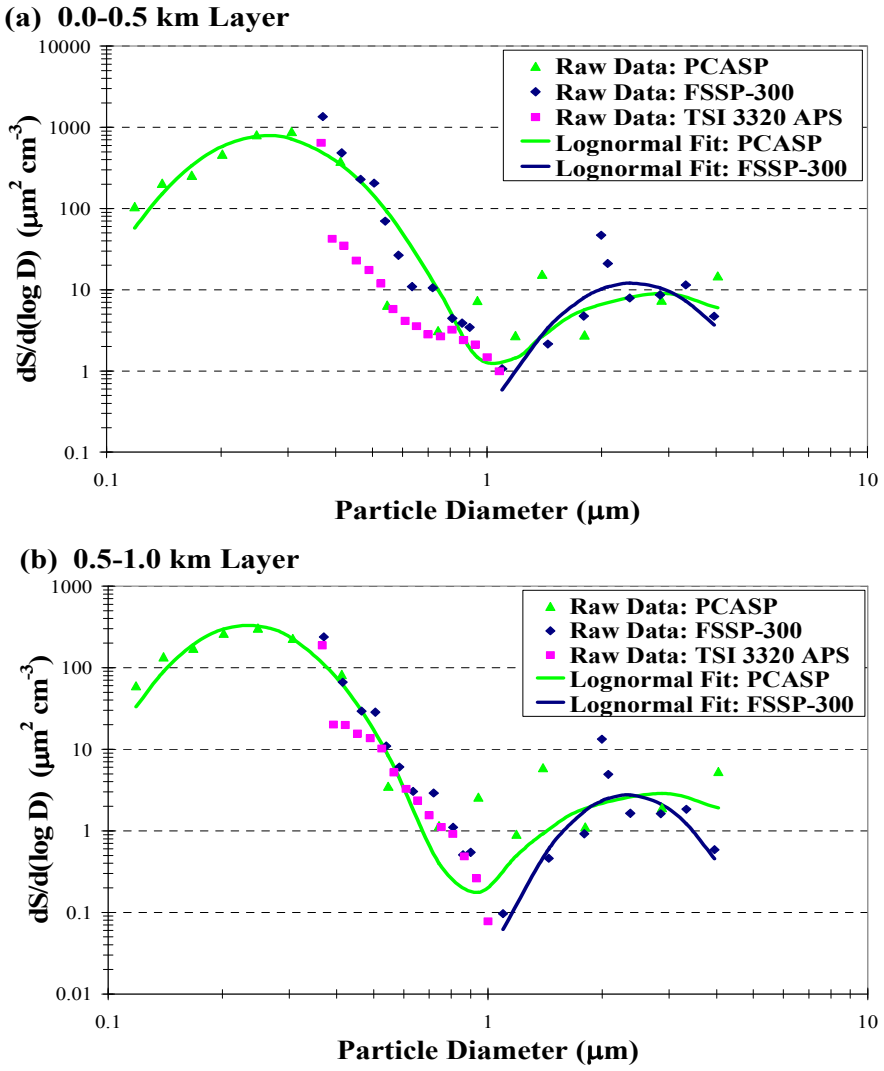

Figure 3.4 Particle surface area distributions for the four layers and total layer mean of the July 17, 2001 flight. Uncertainties associated with the measured particle number concentration from the three particle sizers are discussed in Section 3.1.3.1.

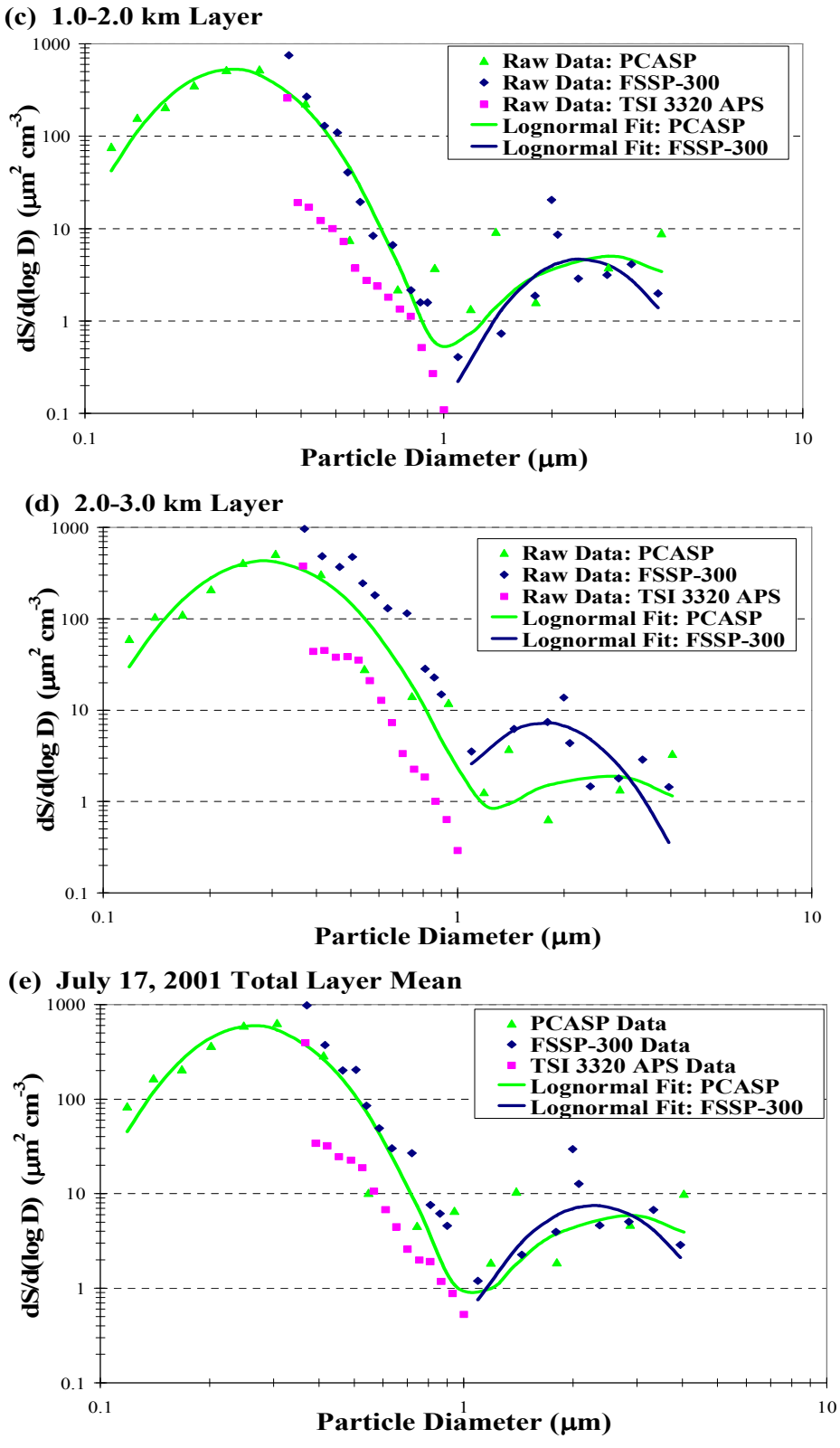

Figure 3.4 (continued)

For the particle surface area distributions measured on August 2, the layer nearest the surface (Fig. 3.5a) shows approximately equal contributions to the surface area distributions from the accumulation mode and coarse mode aerosols, whereas layers aloft (Fig.s 3.5b-d) illustrate the trend of increasing dominance of accumulation mode aerosols with increasing altitude. As mentioned previously, this is likely attributable to the presence of sea spray particles at lower altitudes. There is very little variation with

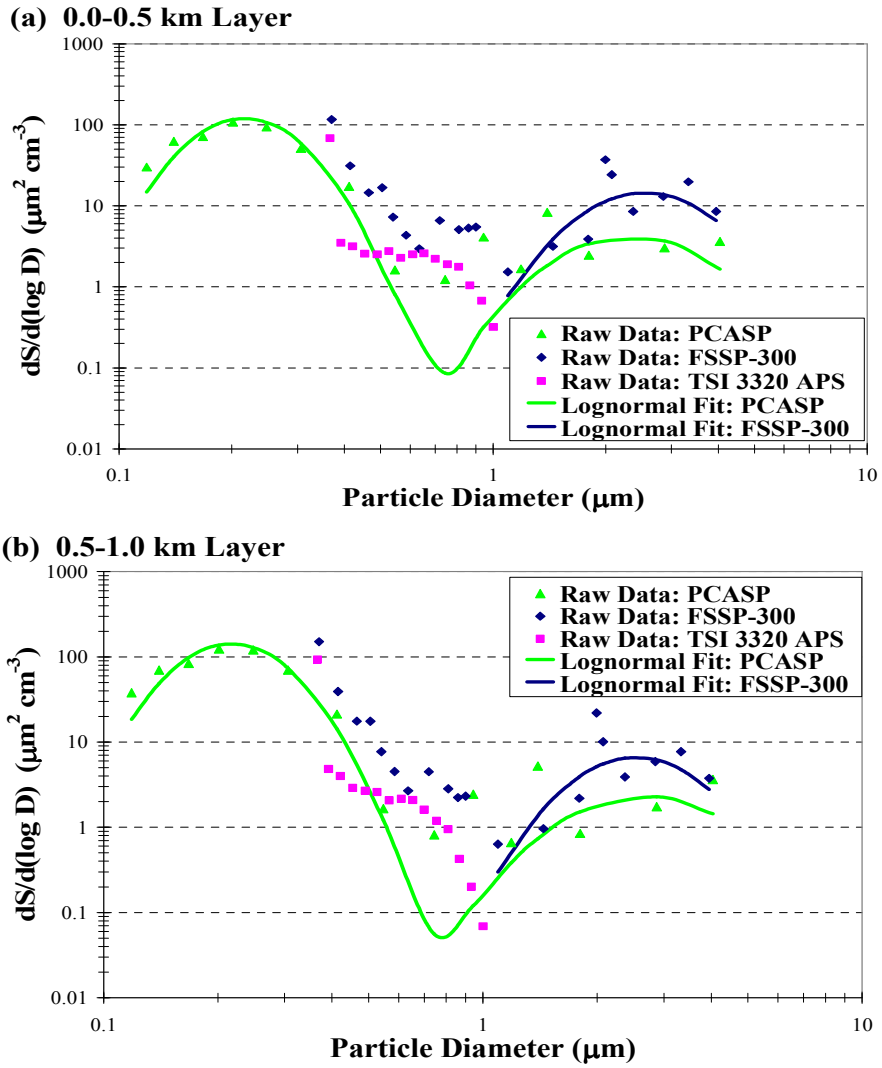

Figure 3.5 Particle surface area distributions for the four layers and total layer mean of the August 2, 2001 flight. Uncertainties associated with the measured particle number concentration from the three particle sizers are discussed in Section 3.1.3.1.

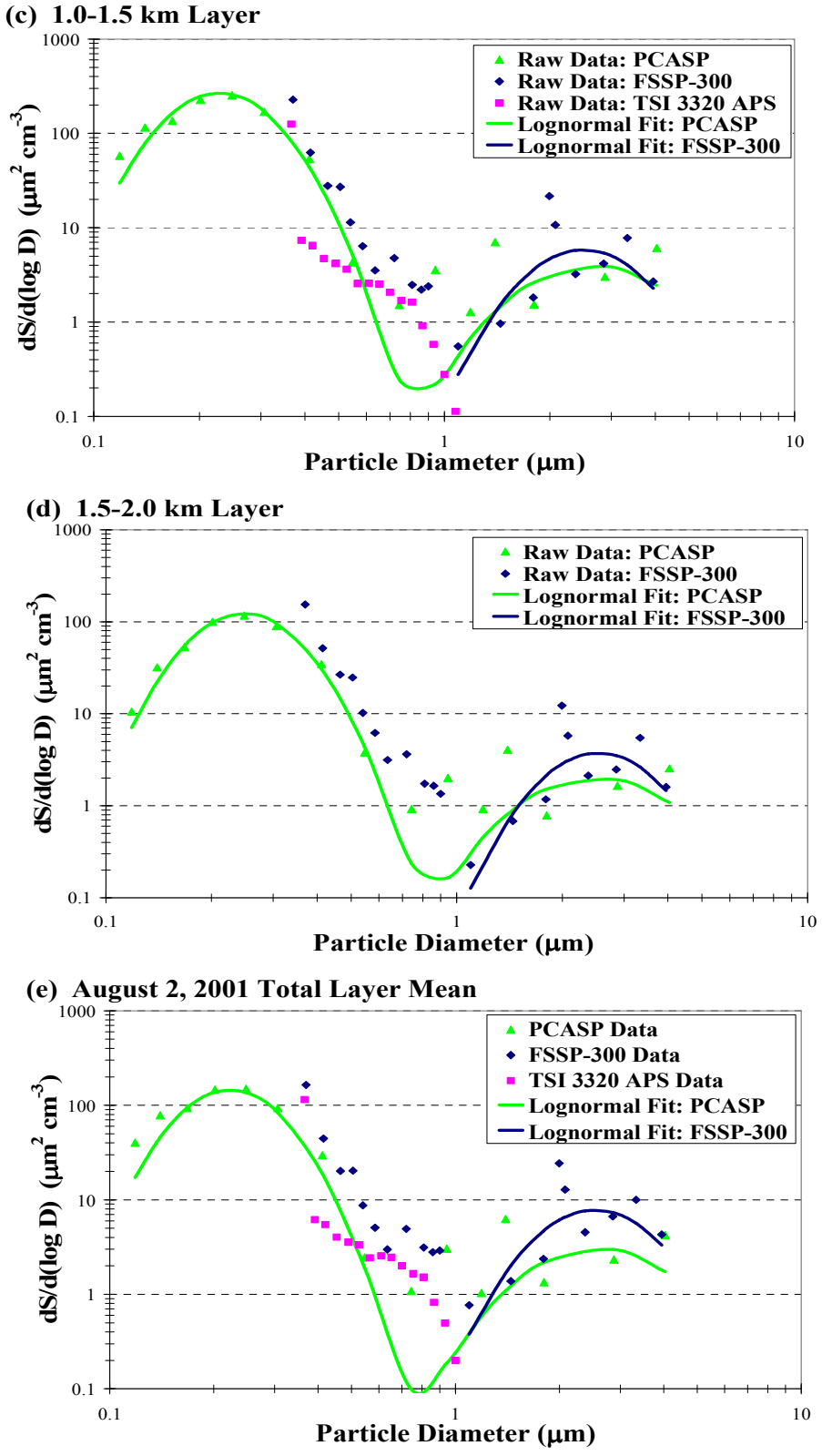

Figure 3.5 (continued)

altitude in the values of D_{smd} for the accumulation or coarse modes. The values of coarse mode D_{smd} from the PCASP and FSSP-300 agree very well (total layer mean D_{smd} from the PCASP was 2.57 μm and that from the FSSP-300 was 2.53 μm).

In comparing the particle surface area distribution results for these two flights, the accumulation mode dominated the particle surface area distributions at all levels where measurements were made (0.04 - 3.0 km MSL) on July 17, indicating a more well-mixed lower troposphere on this day than on 2 August 2001. As expected, there is a greater contribution to the magnitude of the surface area distributions from coarse mode particles (when compared to the number size distributions). Since most of the surface area of the particles was contained in the accumulation mode for the majority of the layers analyzed, aerosols in this size range (0.1 μm < D_p < 1.0 μm) dominated visible light scattering. The magnitude of the surface area distribution in this region where light extinction is most important is significantly greater on July 17 than on August 2, indicating that more scattering/absorption of incident light occurred on July 17. This supports the results shown in Fig. 3.1.

Maxima and minima in the surface (and volume) distribution curves can be associated with the sources and sinks of the aerosol (e.g., Wallace and Hobbs 1977). The mode near $D_{smd} \approx 0.25$ μm in each layer indicates that Aitken nuclei were present in appreciable concentrations, since it is these smallest particles that coagulate to form the accumulation modes noticed here. These sub-micron particles derive primarily from gas-to-particle conversion, a process that was likely enhanced during CLAMS due to the relatively high RH values (mean RH ~60%; see Table 2.2) encountered throughout the

campaign. Gas-to-particle conversion can provide additional mass, and consequently increase the size of the existing aerosol particles through condensation and heterogeneous conversion processes (O'Dowd et al. 1997). The peak(s) at $D_p > 1$ μm are probably due to sea salt particles and further growth by collision and coagulation.

Table 3.4 lists the R^2 values for the nonlinear correlations between the log-normal curves and the PCASP, FSSP-300 results for the particle surface area distributions on both dates. Again, we see that the log-normal curves do a very good job in representing the accumulation mode data on both dates since the R^2 values are much greater than 0.75 (and are actually close to unity), but the coarse mode results exhibit little resemblance to a log-normal distribution.

Table 3.4 As in Table 3.3, but for the surface area distributions.

Flight Date	**Layer**	**Accumulation Mode**	**Coarse Mode**	
			PCASP	FSSP-300
July 17, 2001	0.0-0.5 km	0.9374	0.0009	0.2620
	0.5-1.0 km	0.9718	0.0096	0.2592
	1.0-2.0 km	0.9596	0.0005	0.2358
	2.0-3.0 km	0.9186	0.2872	0.4652
	Total Layer Mean	0.9462	0.0017	0.3049
August 2, 2001	0.0-0.5 km	0.9479	0.0220	0.3074
	0.5-1.0 km	0.9598	0.0201	0.2386
	1.0-1.5 km	0.9677	0.0046	0.2197
	1.5-2.0 km	0.9926	0.0503	0.2165
	Total Layer Mean	0.9713	0.0340	0.2560

3.1.3.3 Particle Volume Distributions

Volume distributions show the total volume of particles per cm^3 of air having diameters in the range D_p to $D_p + dD_p$. The magnitude of the particle volume distribution

provides information about the expected aerosol loading and particle mass concentration, if a particle density is assumed. The value of D_{vmd} is greater than D_g by a factor of $\exp[3\ln^2(\sigma_g)]$ and, as a result, regions of the number size distribution data where discrepancies exist among the three particle detectors are enhanced in the volume distribution plots. Figures 3.6a-e show particle volume distributions for the four layers and total layer mean for the July 17 flight, and Figures 3.7a-e show volume distributions for the four layers and total layer mean of the August 2 flight. There is a significant contribution from aerosols with $D_p \approx 0.3$ μm. The coarse modes in many of the layers do not appear to be fully captured (at least in the PCASP data, which ends at $D_p \approx 4.5$ μm). Furthermore, and perhaps most importantly, there is a much greater contribution from the larger particles ($D_p > 2$ μm) to the overall volume of particles than there is from either the number or surface area distributions. This suggests that while there were relatively few large particles ($D_p >$ 1-4 μm), those that were present made up a significant portion of the total volume occupied by all the particles that were sampled. However, a majority of the particle volume (and therefore mass) is still contained in the accumulation mode, typically found between $D_{vmd} \approx$ 0.25-0.30 μm for all layers. The coarse mode is consistently located around $D_{vmd} \approx$ 2.5-3.0 μm.

The particle volume distribution results from July 17 show little variation with height in the values of D_{vmd} for the accumulation or coarse modes (except the FSSP-300 data for the 2.0-3.0 km MSL layer). This reinforces the conclusion that the lowest part of the troposphere was very well-mixed on July 17. The August 2 particle volume distributions show a trend of decreasing coarse mode contribution to the total particle

volume with increasing altitude. This shows that there were large (most likely sea salt) particles near the surface and that the lower troposphere was not as well-mixed on August 2 as it was on July 17. As has been shown, wind speed measurements made aboard the Convair-580 and at the Chesapeake Bay Lighthouse show that near-surface wind speeds were greater on July 17 than on August 2.

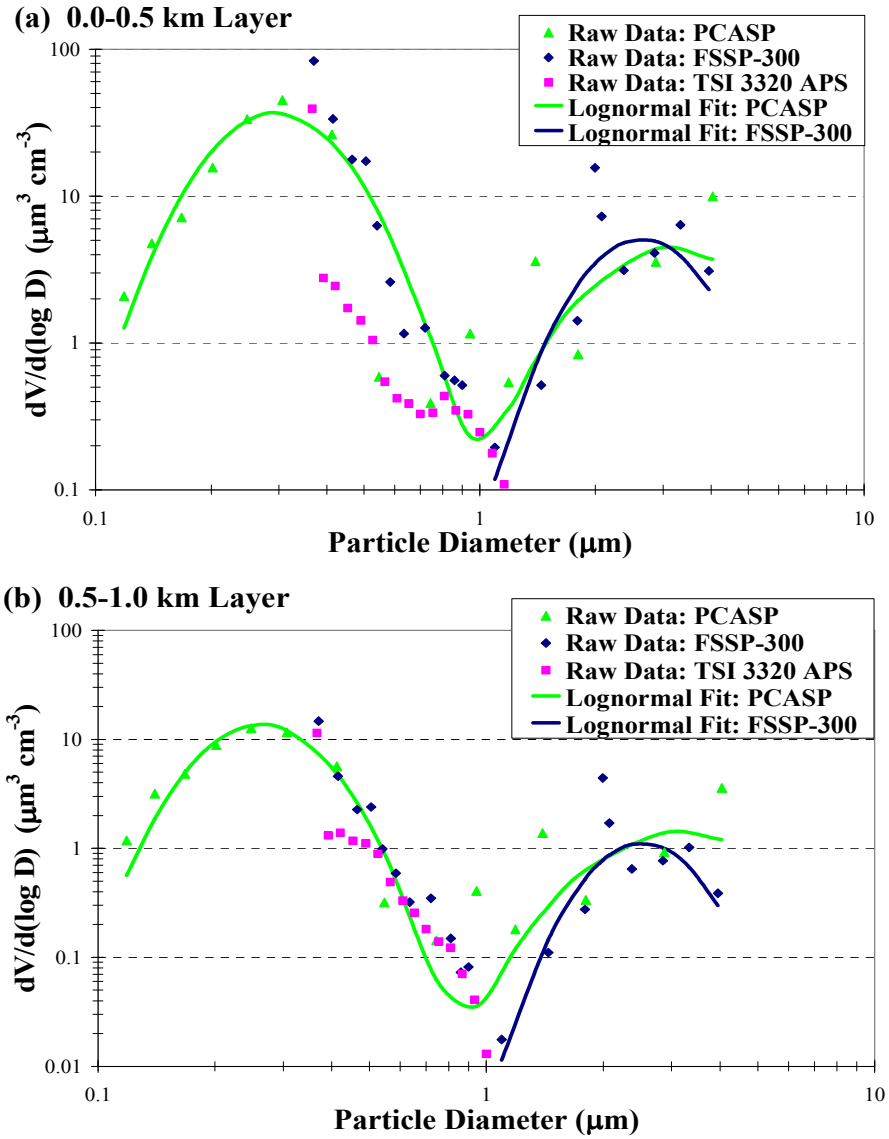

Figure 3.6 Particle volume distributions for the four layers and total layer mean of the July 17, 2001 flight. Uncertainties associated with the measured particle number concentration from the three particle sizers are discussed in Section 3.1.3.1.

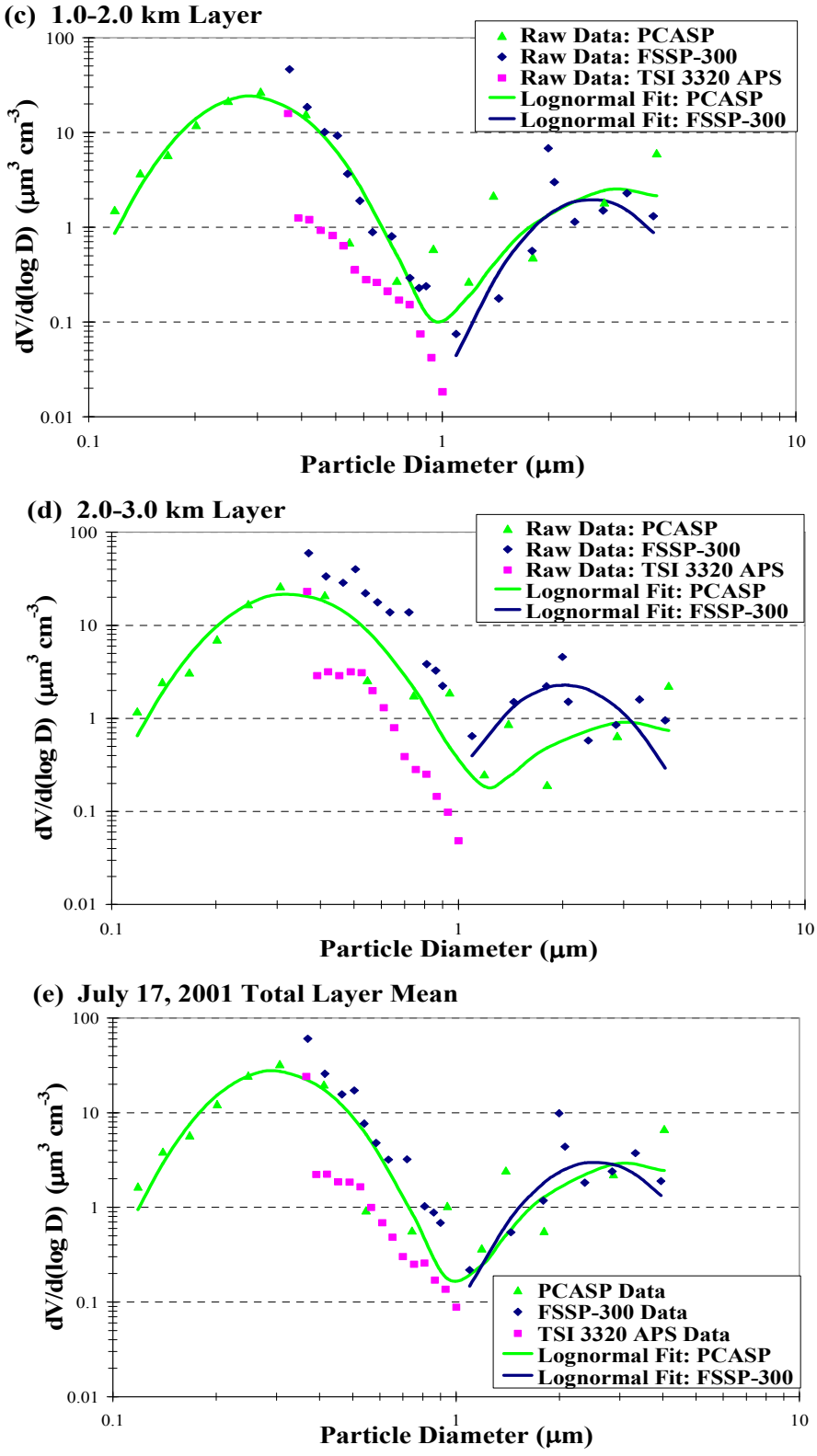

Figure 3.6 (continued)

Therefore, although sea salt particles were probably present at low levels on both days, their effects on the particle size distributions can be seen more explicitly at lower levels on August 2, where fewer particles of other types were present, than on July 17. Furthermore, comparing the July 17 results with those of August 2, it can be seen that the total particle volume (and therefore mass if we assume the same mean particle density on both days) on August 2 was almost an order of magnitude lower than on July 17. This is supported by the results from filter measurements by Magi et al. (2005), which show total particle mass concentrations were 2-3 times greater on July 17 than on August 2.

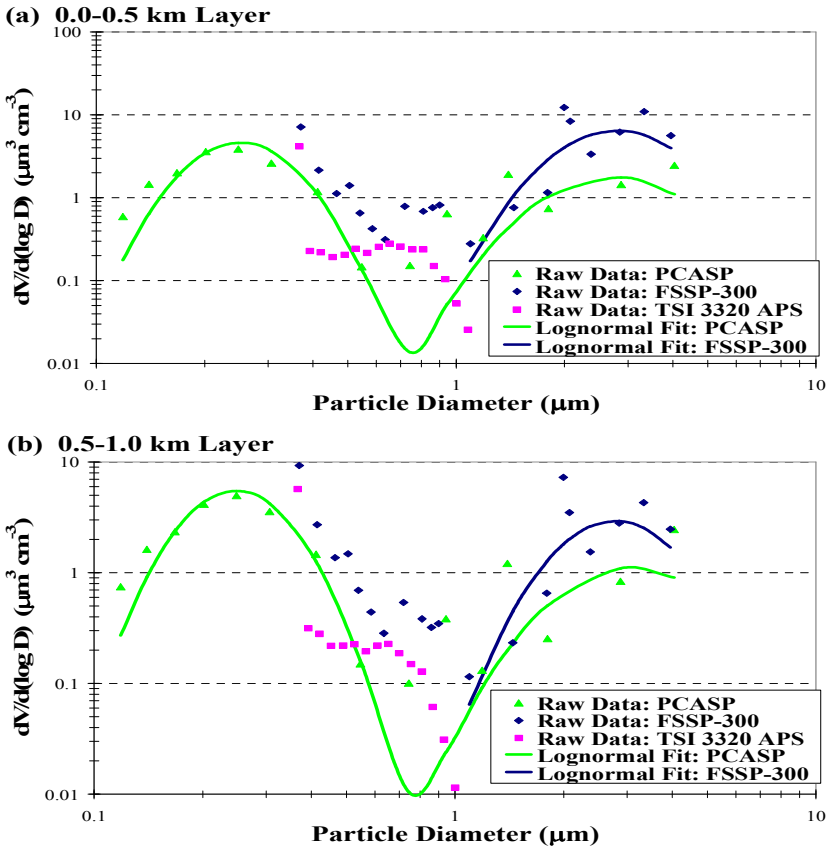

Figure 3.7 Particle volume distributions for the four layers and total layer mean of the August 2, 2001 flight. Uncertainties associated with the measured particle number concentration from the three particle sizers are discussed in Section 3.1.3.1.

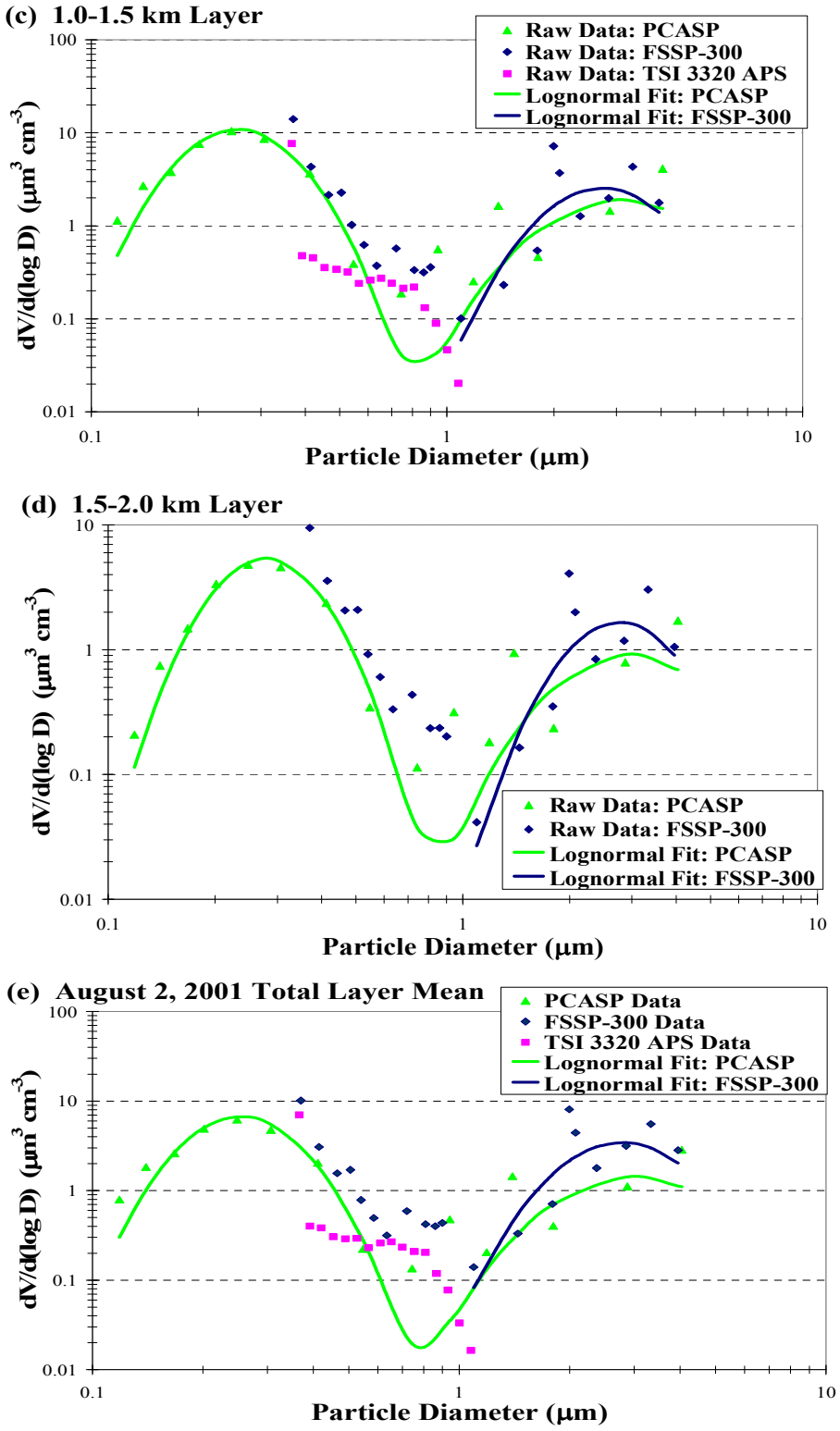

Figure 3.7 (continued)

Table 3.5 lists the correlation coefficients, R^2, for the nonlinear regressions between the log-normal curves (at both modes) and the PCASP, FSSP-300 results for the particle volume distributions from the July 17 and August 2 flights. As was the case for the number and surface area distributions, we see that the log-normal curves do a very good job in representing the accumulation mode data on both flight dates, but the coarse mode results exhibit much less resemblance to a log-normal distribution.

Table 3.5 As in Table 3.3, but for the volume distributions.

Flight Date	**Layer**	**Accumulation Mode**	**Coarse Mode**	
			PCASP	FSSP-300
July 17, 2001	0.0-0.5 km	0.9409	0.3521	0.2145
	0.5-1.0 km	0.9858	0.2581	0.1752
	1.0-2.0 km	0.9626	0.3307	0.1707
	2.0-3.0 km	0.9081	0.1897	0.2624
	Total Layer Mean	0.9473	0.3145	0.2366
August 2, 2001	0.0-0.5 km	0.9265	0.1005	0.3908
	0.5-1.0 km	0.9783	0.2326	0.2727
	1.0-1.5 km	0.9883	0.2932	0.2147
	1.5-2.0 km	0.9895	0.2082	0.2352
	Total Layer Mean	0.9863	0.2109	0.3079

3.1.4 *Total Number Concentration of Particles*

The total number concentrations of particles (N) were measured for the main profile on July 17 (Fig. 3.8a) using the TSI 3320 APS (detectable size range: 0.5 μm < D_p < 1.00 μm), the FSSP-300 (0.35 μm < D_p < 20.72 μm), the PCASP (0.1 μm < D_p < 4.0 μm), and the TSI 3025A (3 nm < D_p < 1.00 μm). During the August 2 flight, a fifth particle counter, the TSI 3022A (7 nm < D_p < 1.00 μm), was in operation for the flight's main profile (Fig. 3.8b). The TSI 3320 APS, the TSI 3022A and the TSI 3025A were

located inside the Convair-580, which limited the maximum size particles that they could detect; the PCASP and FSSP-300 were mounted under the wing of the aircraft.

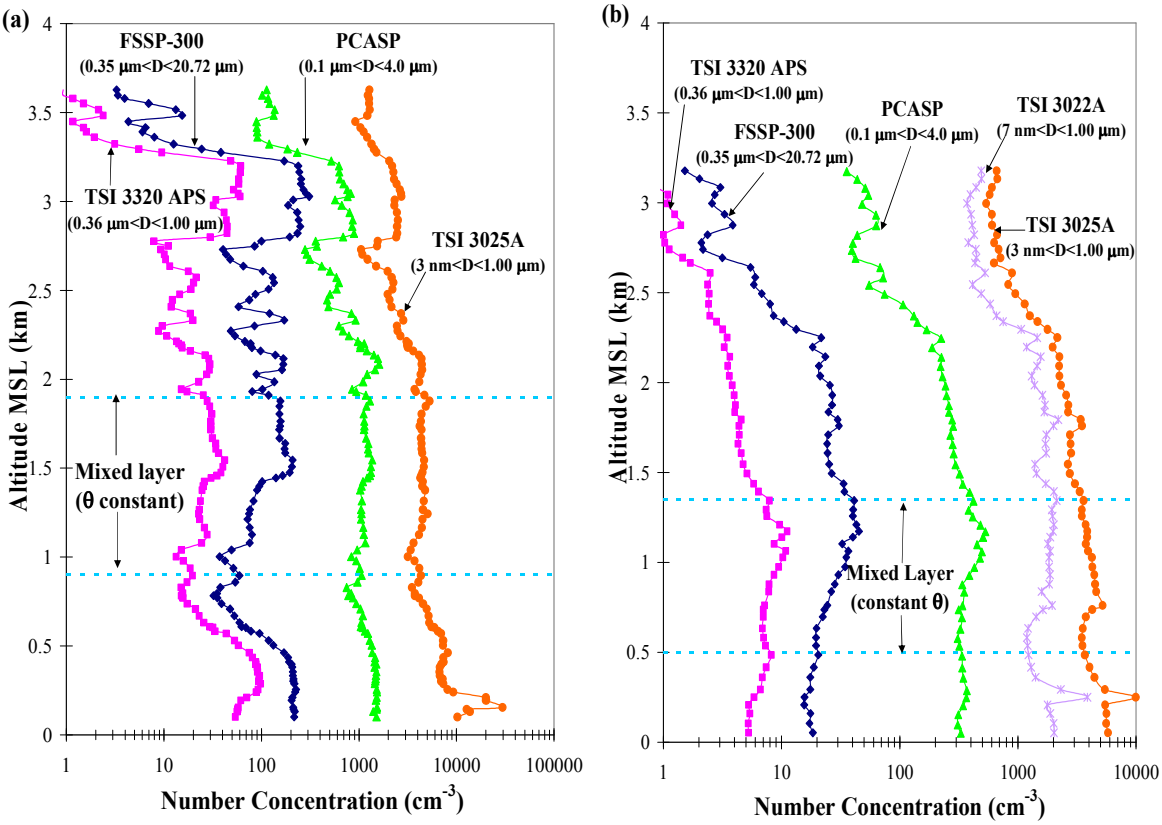

Figure 3.8 Vertical profiles of particle number concentration for (a) aircraft profile #1 of the July 17, 2001 flight and (b) aircraft profile #2 of the August 2, 2001 flight. Uncertainties associated with these instruments are discussed in Section 3.1.3.1.

Typical mean total particle number concentrations measured in CLAMS were ~10^3 to 10^4 cm^{-3} when measured with the most sensitive particle counter, namely the TSI 3025A. Since marine atmospheric particle concentrations are ~100-300 cm^{-3}, there was some continental and/or anthropogenic contributions to the particle sampled in CLAMS. This is supported by the composition data presented by Magi et al. (2005). Table 3.1 summarizes total particle number concentrations, N, for each horizontal transect on the July 17 and August 2 flights measured with the TSI 3025A particle counter. Table 3.2

lists N values for the previously defined layers of both flights. Some of the listed values of N have associated standard deviations that are quite large relative to the mean value. This is a result of strong, localized enhancements in N values at certain points in the component transect(s). Referring to Table 2.2, it can be seen on which transects large spatial areas were sampled, and therefore non-homogeneous air was likely sampled.

In many of the particle number concentration profiles (including the two shown here), a well-defined mixed layer can be seen (shown by the dashed blue lines in Fig. 3.8). This layer is defined by regions where the potential temperature, θ, is steady with height, indicating that the air was well-mixed and, as a result, particle number concentrations were fairly constant with height. Also, in comparing the PCASP and TSI 3025A measurements and knowing the respective detection limits of these particle counters, it can be concluded that there was a predominance of particles with $D_p < 0.1$ μm throughout CLAMS. This suggests nucleation processes, such as gas-to-particle conversion dominated during the campaign.

July 17 was the more polluted of the two days, with a total layer mean particle number concentration of ~7000 cm^{-3}; the total layer mean particle number concentration on August 2 was ~3000 cm^{-3}. The airflow backtrajectories shown in Figs. 2.2-2.3 provide insights as to why this was the case. At low levels on July 17 (Fig. 2.2a) the air recirculated over the coast for at least three days, allowing particle concentrations to build up in the region of our measurements. Further aloft on July 17 (Fig. 2.2b) the airflow was over the Great Lakes, and therefore carried continental (and thus anthropogenically-enhanced) aerosols. In contrast, the airflow backtrajectories on August 2 had a strong

easterly/northeasterly component at all levels up to ~ 3 km (Fig. 2.3). This marine influence led to the much lower particle number concentrations (and AOD values) on August 2.

3.2 Comparison of CLAMS Results to those from the Tropospheric Aerosol Radiative Forcing Observational EXperiment (TARFOX)

The Cloud & Aerosol Research Group (CARG) at the University of Washington has participated in many field campaigns over the past several decades. During the summer of 1996 (July 10-31), the UW Convair-131A aircraft took part in the Tropospheric Aerosol Radiative Forcing Observational EXperiment (TARFOX) over the East Coast of the United States. The primary objective of TARFOX was to obtain data needed to determine the magnitude and uncertainty of direct radiative forcing by aerosols in an airshed dominated by anthropogenic pollution (Hobbs 1999). Since TARFOX occurred during the same time of year and in the same general area as CLAMS, and since the CARG employed similar sampling techniques in both campaigns, there was the unique opportunity to compare the results from both field experiments obtained, of course, under different meteorological conditions. A comparison of the derived aerosol properties from both campaigns is presented in Table 3.6.

The ω_0 values during TARFOX were slightly lower than those found in CLAMS, indicating that the aerosol present during TARFOX were more absorbing (these campaign-average ω_0 values are for polluted layers, where polluted layers are defined as those having $\sigma_{sp} > 30 \times 10^{-6}$ m^{-1}). However, this is not necessarily the case since Hartley

et al. (2000) did not apply the PSAP corrections suggested by Bond et al. (1999), which would have decreased the σ_{apd} values, and thus increased ω_0 values.

Table 3.6 Comparison of aerosol properties from the TARFOX and CLAMS field campaigns.

Parameter	TARFOX	CLAMS
ω_0 (550 nm, ambient RH)	**0.94 (± 0.03)** [Hartley et al. 2000]	**0.96 (± 0.03)**
Accum. Mode r_{eff}	**0.12 μm** [Tanre et al. 1999]	**0.13 μm**
Accum. Mode D_g	**0.19 μm** [Hartley & Hobbs 2001]	**0.20 μm**
Accum. Mode D_{smd}	**0.24 μm** [Russell et al. 1999]	**0.24 μm**
Accum. Mode D_{vmd}	**0.27 μm** [Smirnov et al. 2000]	**0.28 μm**
N (PCASP; 0.1 μm < D_p < 4.0 μm)	**~1600 cm^{-3}** [Hegg & Kaufman 1998]	**800 ± 600 cm^{-3}**
AOD (550 nm vs. 525 nm)	**0.30 ± 0.20** [Hegg et al. 1997]	**0.13 ± 0.10**
Apportionment of AOD	**C > H_2O > SO_4^{2-} (BC~7%)** (40±15)%>(35±23)%>(19±8)% [Hegg et al. 1997]	**SO_4^{2-} > H_2O > C (BC≤ 4%)** (38±8)%>(32±9)%>(26±9)% [Magi et al. 2005]

The accumulation mode size parameters were virtually identical for both campaigns. The largest differences in the aerosol properties of both experiments are in the particle number concentrations (N) and in the particle composition. As measured by the PCASP, N values were twice as high in TARFOX than they were in CLAMS. This is also reflected in the mid-visible wavelength AOD values which were 2-3 times greater in TARFOX.

Some of the largest differences in aerosol properties can be seen when comparing the chemical apportionment of AOD from both experiments. The carbonaceous and condensed water components dominated composition in TARFOX, while the sulfate component was greatest during CLAMS. In both campaigns, though, the black carbon (BC), or absorbing component, was very low, hence the relatively high ω_0 values.

These differences are attributable to the differing airflow backtrajectories and meteorological conditions present in the two experiments. During TARFOX, air parcel backflows were mainly from the west or southwest, having passed over industrial, agricultural and urban areas in the midwestern and southern U.S. Conversely, during CLAMS air parcel backtrajectories typically had a strong northerly/northeasterly component, having passed over Quebec and the northern Atlantic Ocean. Also, the summer of 2001 (when CLAMS was conducted) was atypical for the East Coast of the U.S. An unusual number of cold frontal passages occurred, bringing cleaner air to the study region.

3.3 Small-scale Horizontal Variability of Aerosol Properties

Of considerable interest to satellite retrievals of aerosol properties is the small-scale spatial and temporal variability of these properties. An analysis of the small-scale spatial variability of aerosol properties provides an answer to the question of whether or not an average radiance in a given scene, as measured by a satellite sensor such as MISR, can be readily translated into an average aerosol parameter over the scene. This analysis

allows a determination of the effect of spatiotemporal offsets on the validation results. In the process, we will be able to conclude whether or not the resolution of the MISR aerosol retrieval algorithm (~17.6 km) allows small-scale spatial changes in aerosol properties to be accurately captured. Also, an analysis of this sort shows whether or not the "layer method" employed in the particle size distributions is justified (i.e., does grouping horizontal transects from different areas in space mask any atmospheric variability). This analysis was performed by dividing each transect of both flights into 10 s intervals, which correspond to a horizontal distance of ~1 km (since the mean aircraft speed was ~100 m/s).

Anderson et al. (2003a) discuss the mesoscale variations of tropospheric aerosols and conclude that significant variability was present on timescales of <10 h and on spatial scales of ~200 km or less. Here, the concern is not with the temporal variability of the aerosol, since our flights were only 3-6 h in duration. Rather, the focus is on the potentially significant role of spatial variability, since the Convair-580 flights typically covered areas of hundreds of kilometers, both zonally and meridionally. Table 2.2 shows that the vertical profiles were flown in tight spiral ascents/descents, virtually eliminating any horizontal inhomogeneities; however, the horizontal transects often covered hundreds of kilometers in the horizontal. Unlike the data sets discussed by Anderson et al. (2003a), the Convair-580 flights did not seek out aerosol plumes, but rather concentrated on flying simultaneous and coordinated flight paths with other measuring platforms.

Measured variability is the sum of ambient variations and measurement noise (Anderson et al. 2003a). Therefore, as Anderson et al. (2003a) explain, variability in

aerosol properties can be studied only if: 1) instrument noise is known to be negligible or 2) instrument noise can be quantified and a correction applied. Here, we examine the lag-1 autocorrelation coefficient, r(1), to evaluate instrument noise. For our analysis, we have chosen a time lag interval of 10 s, corresponding to a spatial resolution of ~1 km. If the correlation is extremely high (i.e., r(1) > ~0.99), the measurement is free of noise at the specified resolution *and* there is no significant ambient variability at this spatiotemporal scale. However, if r(1) < ~0.97, then the cause could be *either* instrumental noise or ambient variability (personal communication, T. Anderson 2005).

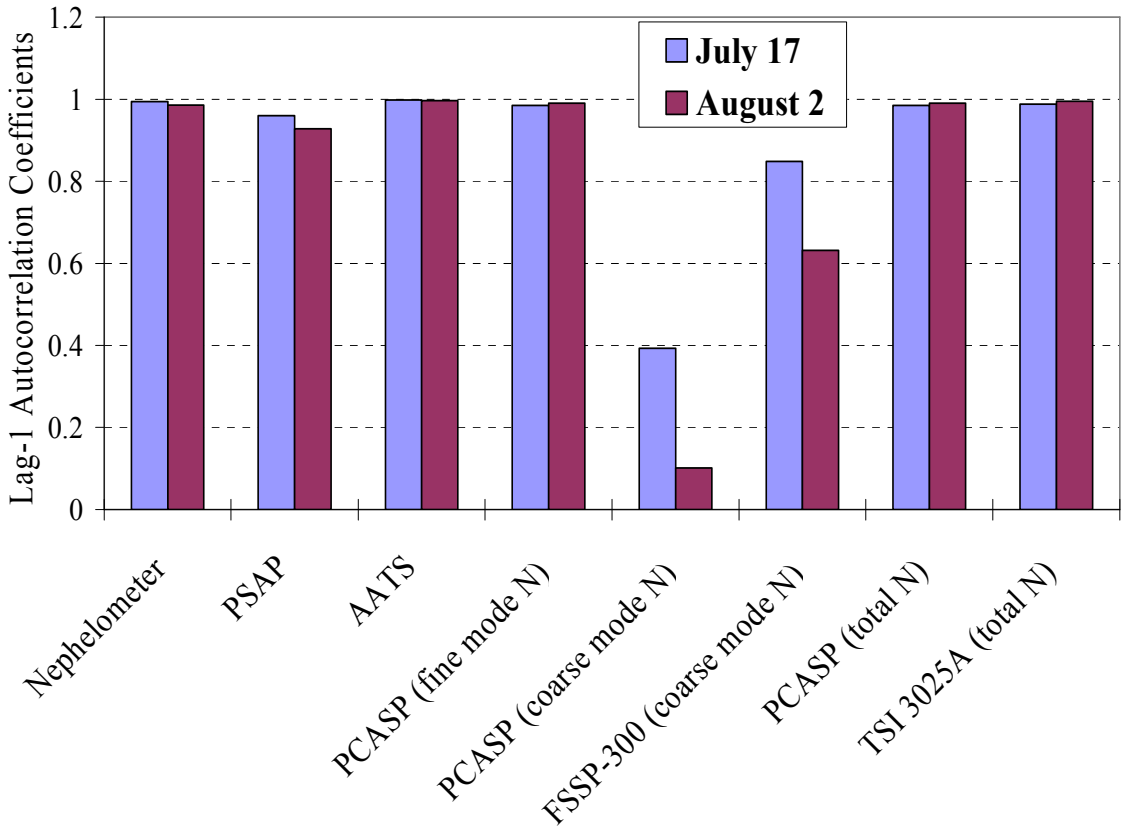

Fig. 3.9 Lag-1 autocorrelation coefficients, r(1), for the instruments used in the analysis of small-scale horizontal variability. A 10 s lag has been used for all instruments (though the PSAP has an inherent 30 s running average, which is discussed in Section 3.3.1). For the particle counting/sizing instruments, the specific size classification is denoted in parentheses.

Figure 3.9 illustrates graphically what will be discussed in the following few sections- mainly, that the r(1) values for all parameters except coarse mode N, are large enough to rule out instrumental noise as a source of observed variability.

3.3.1 Optical Parameters

Figure 3.10 shows the results from the autocorrelations for both σ_{sp} on July 17 (Fig. 3.10a) and August 2 (Fig. 3.10b), as well as σ_{apd} on July 17 (Fig. 3.10c) and August 2 (Fig. 3.10d). On both days the r(1) value is $\geq$ ~0.99 for the σ_{sp} data, so we are confident there is no noise or significant variability in this parameter at spatial scales of ~ 4 km. (The resolution is stated as ~ 4 km since the PSAP and nephelometer data were processed with 30 s smoothing in order to reduce instrument noise. In addition, these 30 s running averages were averaged over 10 s intervals for the autocorrelation analysis. Therefore, the spatial resolution is ~ 4 km assuming an aircraft speed of ~ 100 m s^{-1}.) However, the r(1) values for σ_{apd} were 0.9604 on July 17 and 0.9284 on August 2. Given the relative homogeneity in particle composition reported by Castanho et al. (2005) along with the very low σ_{apd} values throughout CLAMS (often times bordering on the detection limit of the PSAP, 1 x 10^{-7} m^{-1}), this poor correlation is likely a result of instrument noise rather than ambient variability in σ_{apd}. These findings are supported by the results of Anderson et al. (2003b) which show that the instrumental noise associated with: 1) PSAP measurements of σ_{apd} in ACE-Asia was 0.72 x 10^{-6} m^{-1} for all sampled particles and 0.33 x 10^{-6} m^{-1} for sub-μm particles and 2) nephelometer measurements of σ_{sp} in ACE-Asia

was 0.15 x 10^{-6} m^{-1} for all sampled particles and 0.14 x 10^{-6} m^{-1} for sub-μm particles. While these results confirm the findings presented here that there is minimal instrumental noise in PSAP and nephelometer measurements of σ_{apd} and σ_{sp}, respectively, it should be noted that the Anderson et al. (2003b) analysis used a time resolution of 240 s for both instruments (we have used a time resolution of 40 s for the PSAP and 10 s for the nephelometer) and measurements from TSI Model 3563 nephelometers (we have used an MS Electron nephelometer). It should also be pointed out that the nephelometer was typically run at a flow rate of 30 L/min. Given the ~2 L sampling volume, there is the potential for a ~4 s lag between sampling volumes, and therefore some variability in σ_{sp} may be masked because of residual air remaining in the sampling volume from the previous averaging time.

Figure 3.11 illustrates the small-scale horizontal variability of σ_{apd}, σ_{sp} and ω_0 at a wavelength of 550 nm for a few selected transects at various levels of the atmosphere from both the July 17 and August 2 flights. These transects are representative of ~ 4 km variability in aerosol optical properties in the other transects not presented here. One of the most notable features of the measurements shown in these figures is the relatively uniform values of ω_0 throughout a given transect, regardless of the altitude of the transect. While σ_{sp} and σ_{apd} vary, often times an increase in σ_{sp} has a corresponding increase in σ_{apd} (or there is a coincident decrease in both parameters), and thus ω_0 remains fairly constant. This alludes to the fact that σ_{sp} and σ_{apd} are extensive parameters (i.e., they depend upon the amount of aerosol present), while ω_0 is an intensive property (i.e., one that does not depend upon the amount of aerosol present). Where this is

observed, we can conclude that the population of particles being sampled is of a similar aerosol type, but that the aerosol concentration varies (Anderson et al. 2003a). In some cases, a slight systematic increase in ω_0 can be seen (Fig. 3.11a) due to a rise of σ_{sp} while σ_{apd} remained fairly constant. This is not a humidification effect since the aerosol entering the nephelometer were dried (to ~30% RH), therefore the change in ω_0 signals a change in aerosol type (i.e., aerosol composition, size, etc.). Conversely, Fig. 3.11c shows a gradual decrease in ω_0 associated with declining values of σ_{sp} and constant values of σ_{apd}. However, even in these two cases, the overall small-scale horizontal variability in ω_0 is minimal (note the very small standard deviations associated with the mean ω_0 values over the course of any given transect).

In transects where ω_0 shows some variability, the variability is mostly attributable to changes in σ_{apd} throughout the transect. It should be noted that the value of σ_{apd} throughout CLAMS was remarkably low (on average, ~2.0×10^{-6} m^{-1}) and, as a result, the ω_0 values can be sensitive to small changes in σ_{apd}. Also, unlike the sharp decline in ω_0 values in the profiles of Fig. 3.1, the transects at higher levels of the lower troposphere (e.g., Fig. 3.11d) still show consistently high ω_0 values. In all transects of both flights, the standard deviation (SD) is $\leq$ 2% of the mean ω_0 value. Thus, there is minimal variability in the value of ω_0 on horizontal scales of ~ 4 km and the optical parameters more commonly vary on scales of tens of kilometers, if not more.

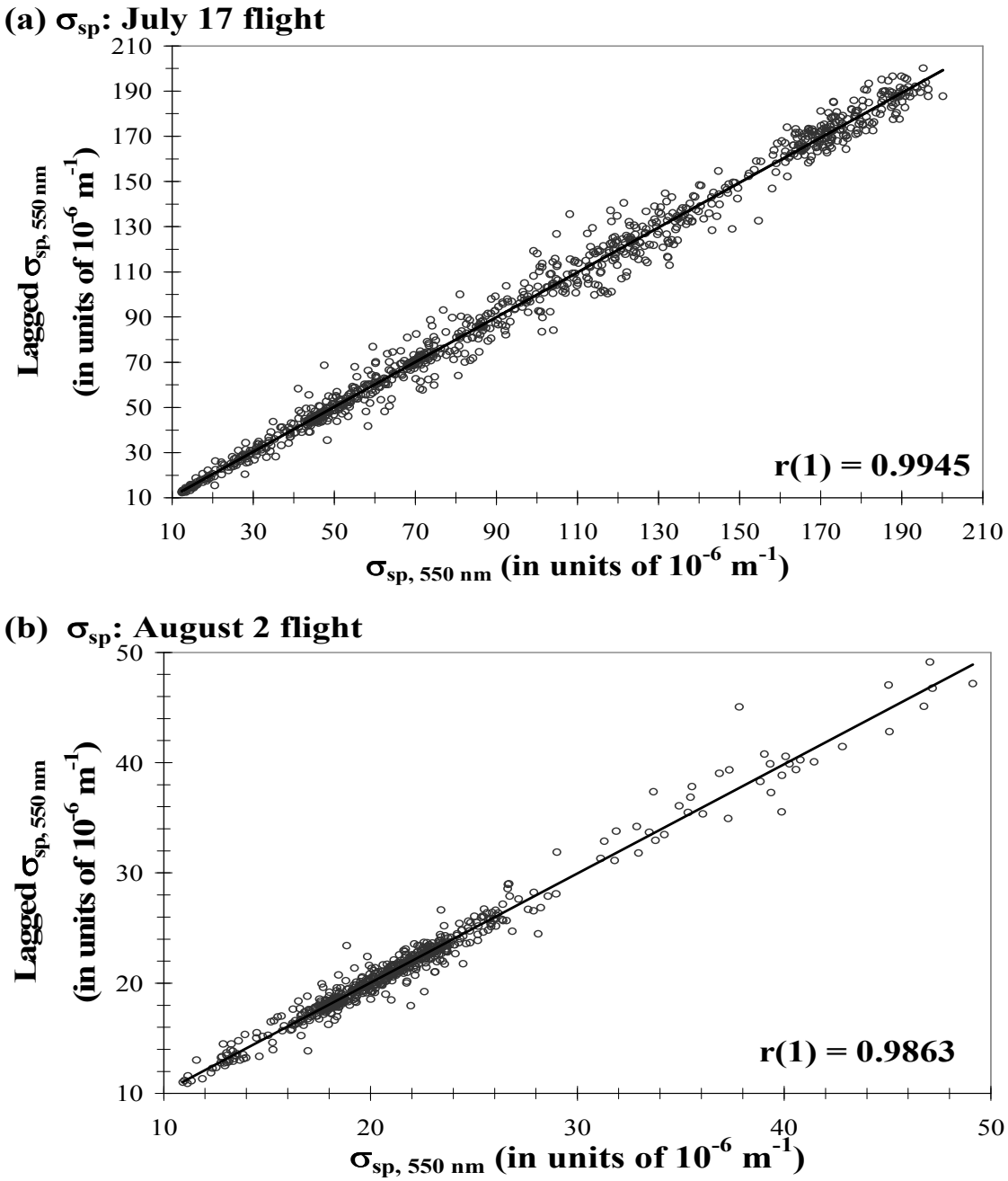

Figure 3.10 Lag-1 autocorrelation for σ_{sp} [(a) July 17 and (b) August 2] and σ_{apd} [(c) July 17 and (d) August 2] measurements made with the nephelometer and PSAP, respectively. The lag is one measurement interval, which we have chosen to be 10 s.

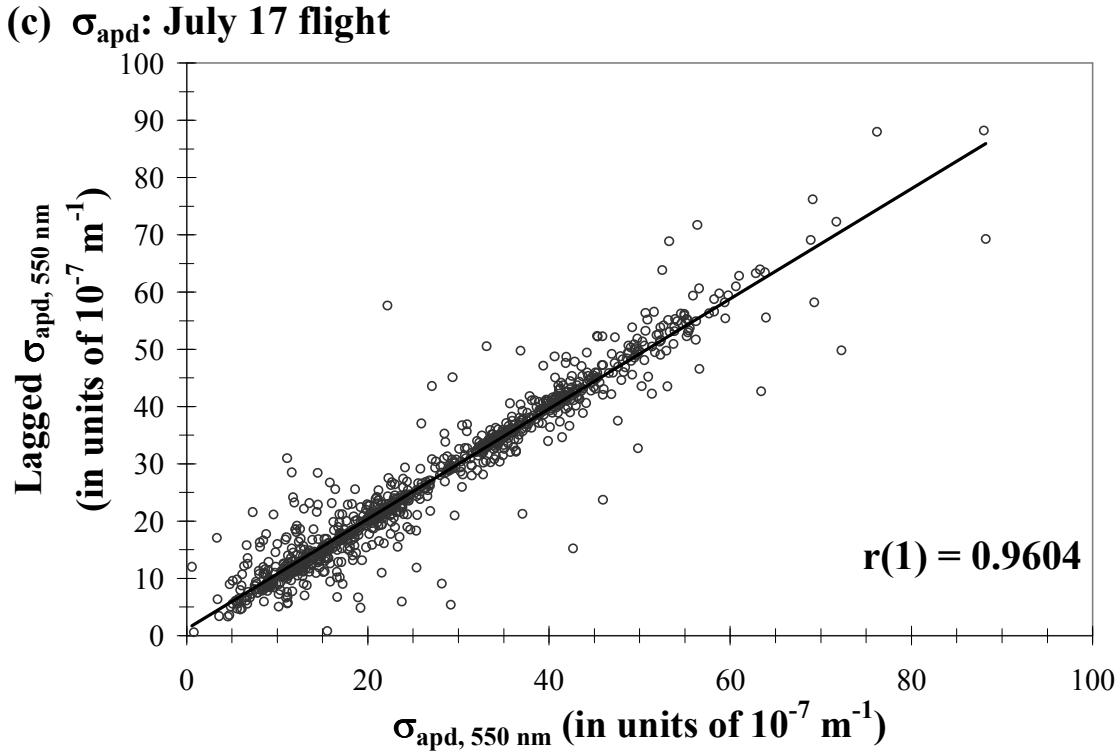

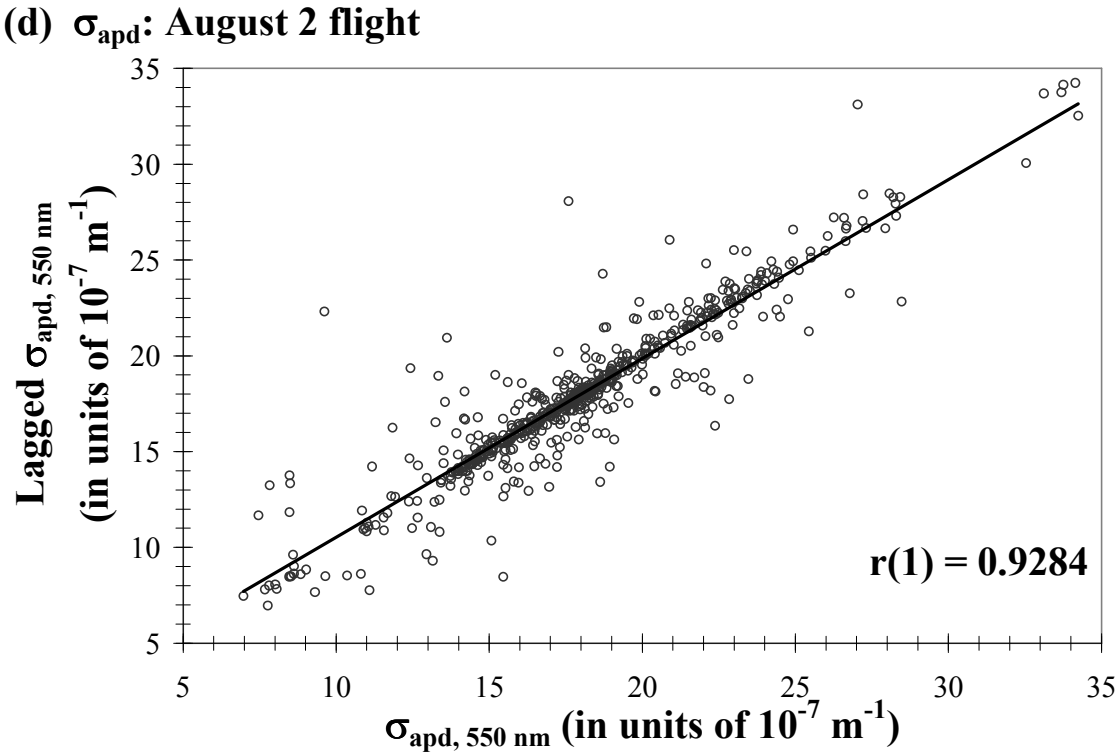

Figure 3.10 (continued)

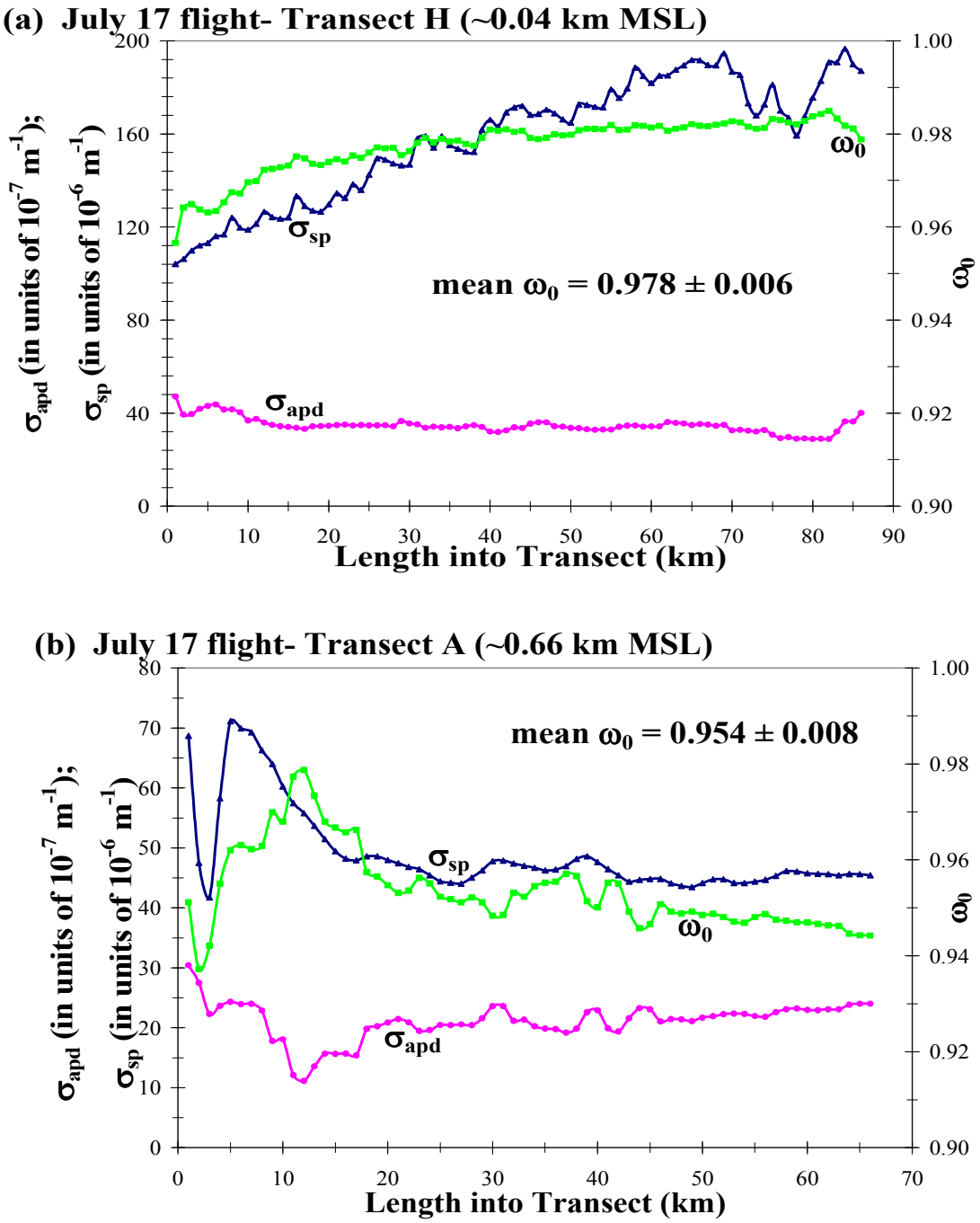

Figure 3.11 Small-scale (~ 4 km) horizontal variability of σ_{apd}, σ_{sp} and ω_0 at a wavelength of 550 nm for selected transects from July 17 and August 2 flights representing various levels of the lower troposphere.

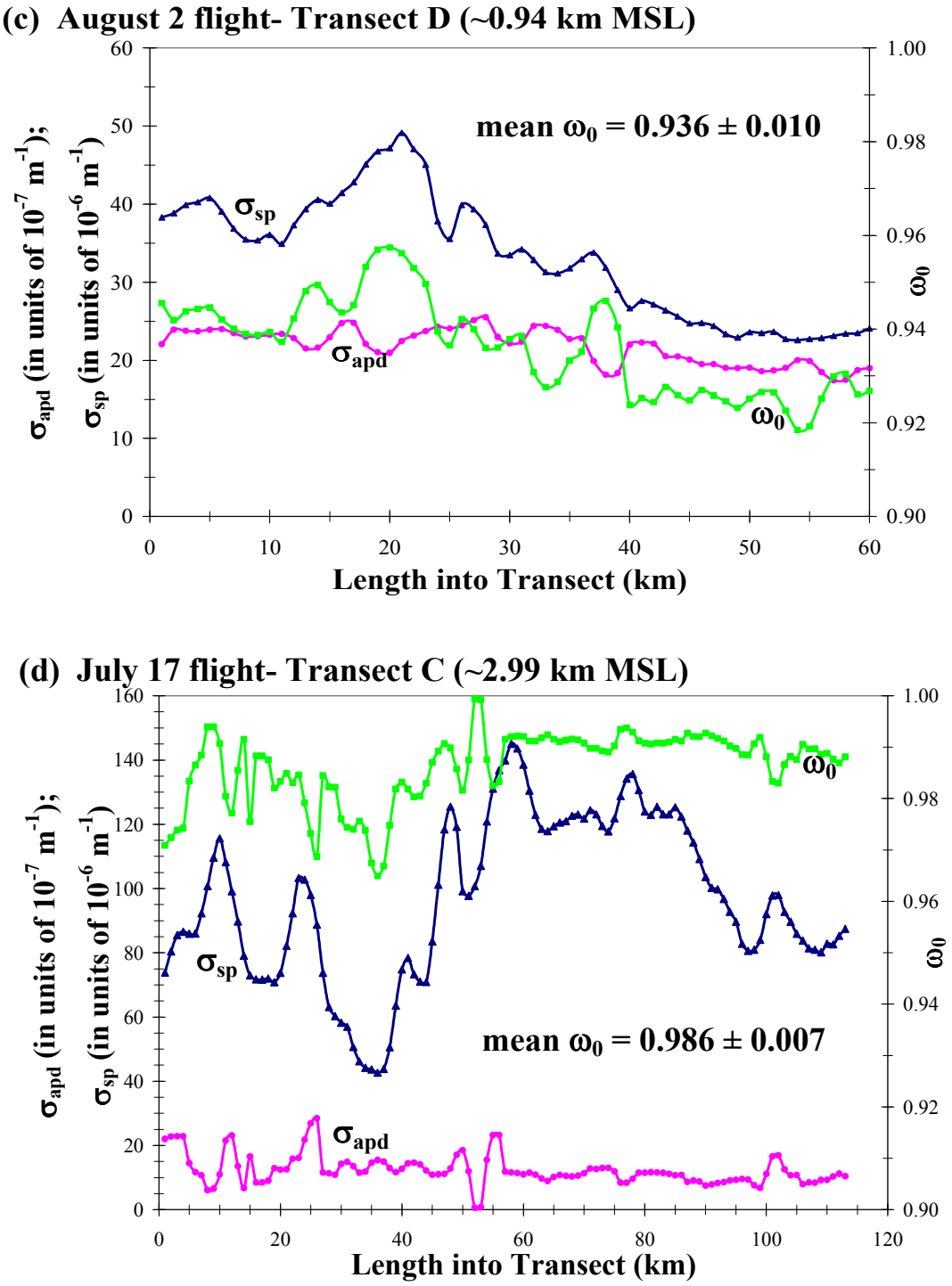

Figure 3.11 (continued)

3.3.2 Aerosol Optical Depth

The results presented here serve as a supplement to the analysis carried out by Redemann et al. (2005). Figure 3.12 shows the r(1) results for the AOD measurements on July 17 (Fig. 3.12a) and August 2 (Fig. 3.12b). Redemann et al. (2005) discuss their methods for data reduction, calibration and error analysis of the AATS data. Since the authors have already accounted for instrument noise in the AATS data provided to us, we do not discuss noise reduction here. Rather, we show the results of the lag-1 correlation for all AATS data points obtained during the transects of both flights. The results are shown in Figure 3.12. Since Redemann et al. (2005) have already accounted for instrument noise in the AOD data used in this paper, it is appropriate that the r(1) values are quite high. The autocorrelation statistic at a lag time of one interval (10 s) using data from all transects of both flights was 0.9987 for July 17 and 0.9965 for August 2. Therefore, we conclude that these data are free of noise at this resolution (~1 km) and that there is no significant ambient variability at this spatial scale.

Redemann et al. (2005) analyzed the small-scale horizontal variability in AATS-derived AOD throughout CLAMS. They also perform correlations between AATS-, AERONET-, MODIS-, and MISR-derived AOD values. Their results show that AOD can vary by as much as 50-70%, but more typically 25-30% over horizontal distances of 50 km. Furthermore, they discovered that there was no spectral dependence of the relative variability in AOD. This suggests that the spatial variability in AOD during CLAMS was caused more by the transport and diffusion of similar aerosol types rather than the mixing of aerosol types having different sizes and compositions.

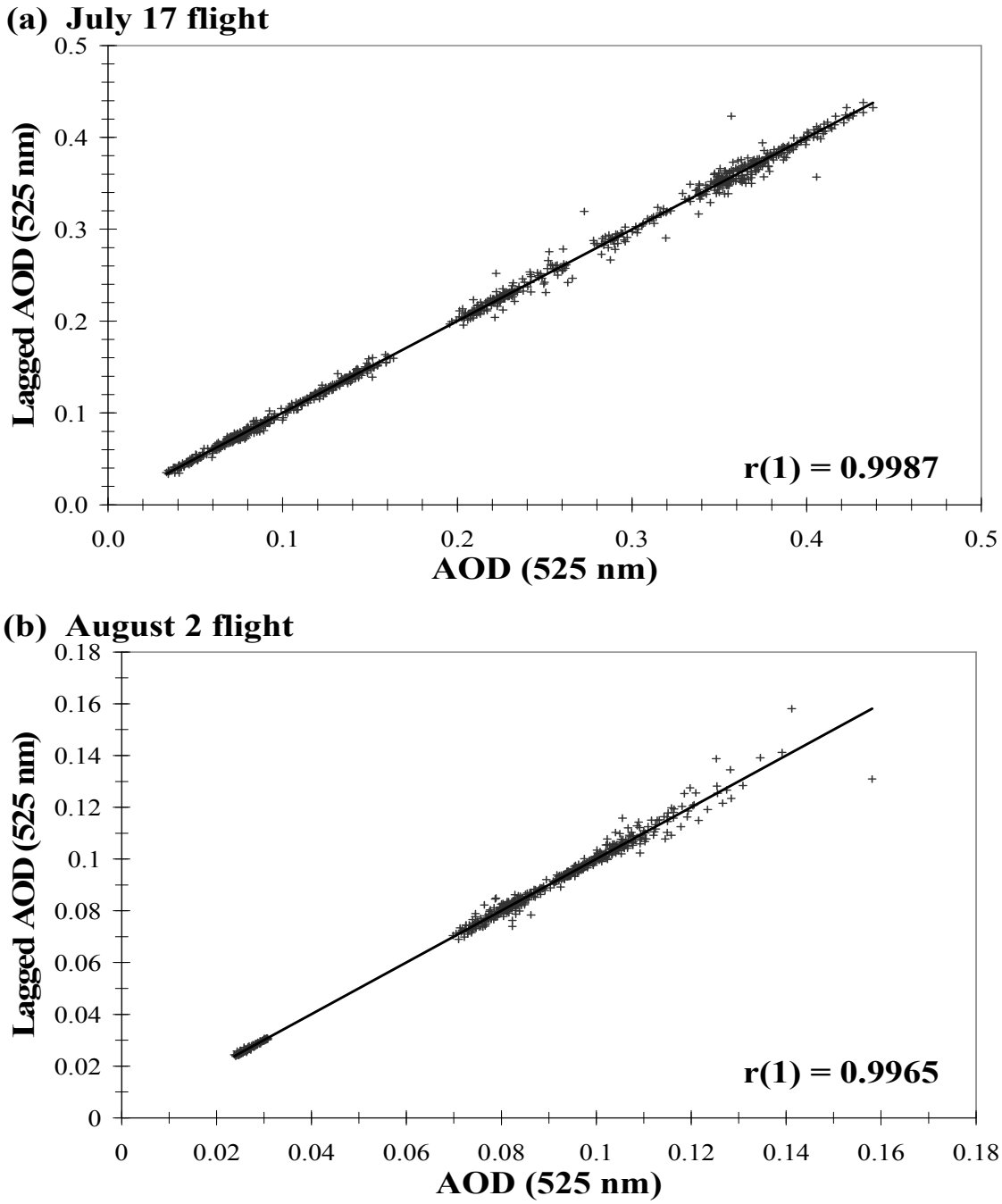

Figure 3.12 Lag-1 autocorrelation for AOD measurements made with the AATS-14 on (a) July 17, 2001 and (b) August 2, 2001 The lag is one measurement interval, which we have chosen to be 10 s or 1 km resolution.

The transport and diffusion of similar aerosol types could create regions of higher (lower) particle number concentration, which would create more (less) light extinction in the region, and ultimately cause higher (lower) AOD values (i.e., spatial variability in AOD).

Figure 3.13 illustrates the small-scale horizontal variability in AOD (at a mid-visible wavelength of 525 nm) for all transects of the (a) July 17 and (b) August 2 flights. The values presented in these figures were measured with the AATS-14 aboard the Convair-580 aircraft. Included in the figures are the mean AOD values for each transect with one standard deviation. These results are also derived from our AATS-14 measurements. It can be seen that AOD varies minimally even on horizontal scales of tens (sometimes hundreds) of kilometers at all levels of the lower troposphere.

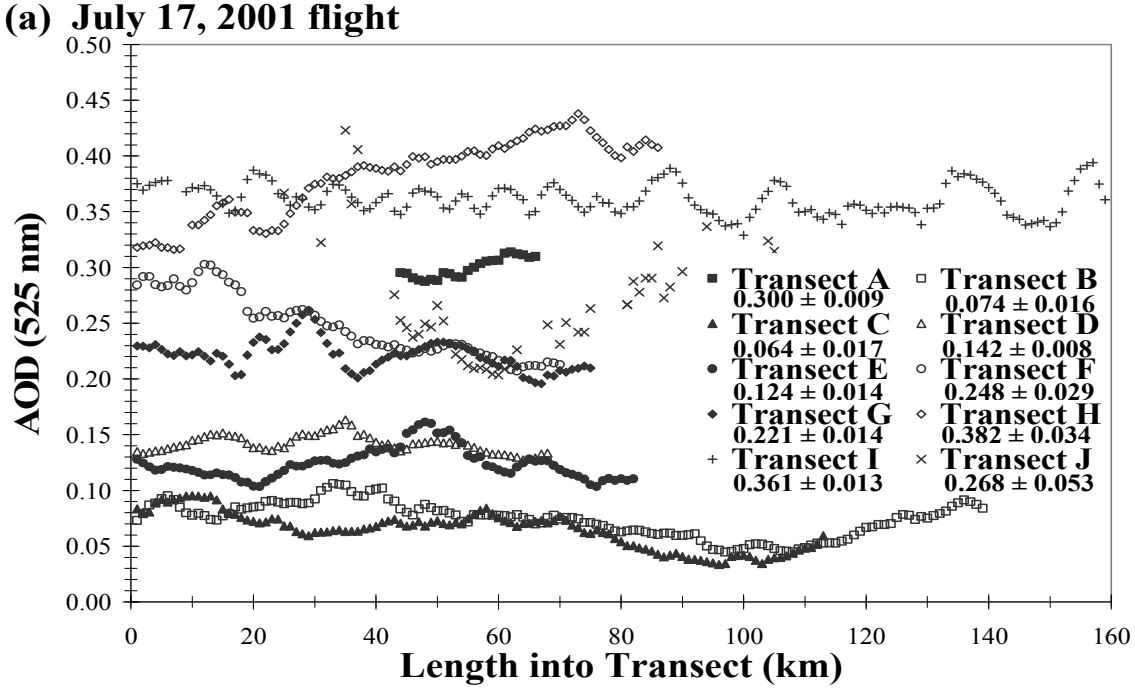

Figure 3.13 Small-scale (~1 km) horizontal variability in AOD (at 525 nm) as measured by the AATS-14 for all transects of the (a) July 17 and (b) August 2, 2001 flights with means and one standard deviation reported below each transect label.

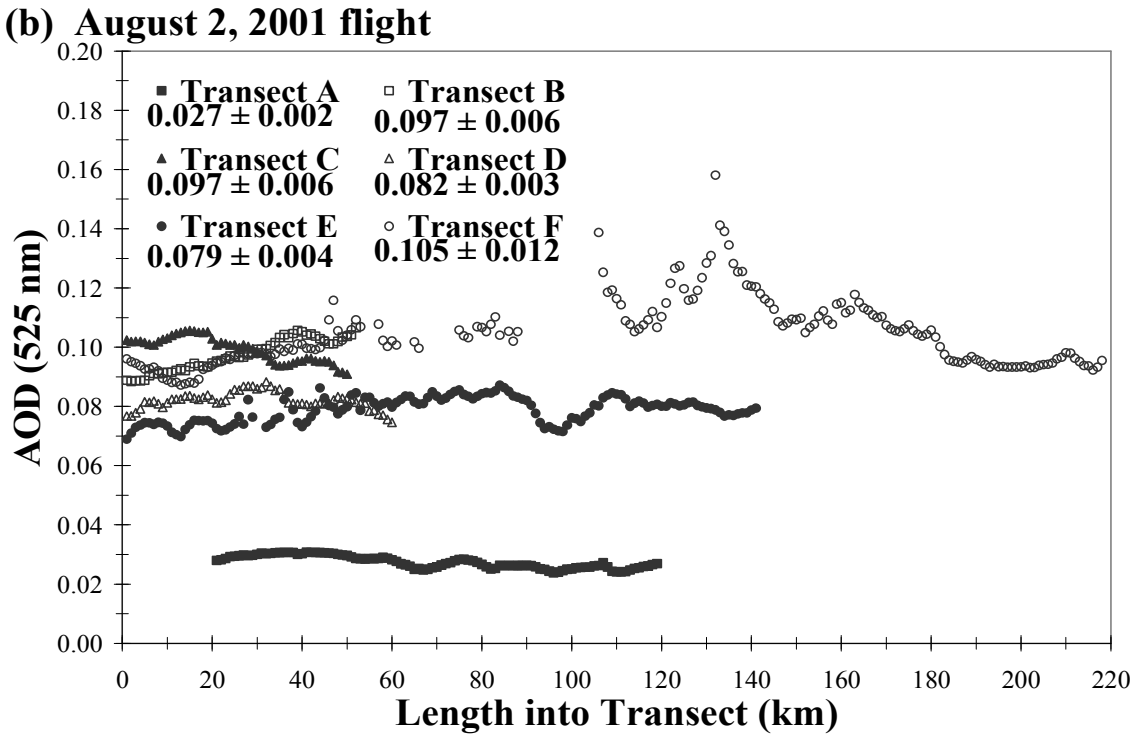

Figure 3.13 (continued)

3.3.3 Particle Size Parameters

Figure 3.14 shows the results from the autocorrelations for fine and coarse mode particle number concentrations (N) as measured by both the PCASP and FSSP-300 optical particle counters. On both days the r(1) value is ≥ ~ 0.99 for the fine mode N data from the PCASP, so we are confident there is no noise or significant variability in this parameter at spatial scales of ~1 km. However, the r(1) values for coarse mode N as measured by both the PCASP and FSSP-300 on both days (Fig. 3.14b-c and Fig. 3.14e-f) were quite poor. Given the extremely low coarse mode number concentrations on both days (the vast majority of second-by-second measurements were 0 cm^{-3} for all bins grouped in the coarse mode), we are unable to make any conclusions regarding the spatial

variability of coarse mode size parameters, and thus no plots are shown illustrating the small-scale horizontal variability of coarse mode size parameters on these two days during CLAMS.

Figure 3.15 illustrates the small-scale horizontal variability of accumulation mode particle size parameters measured by the PCASP for a few selected but representative transects from both flights at various levels of the lower troposphere. This figure explicitly shows the minimal variability in the horizontal of accumulation mode size parameters. Since D_{smd} is larger than D_g by a factor of $\exp[2\ln^2(\sigma_g)]$, and D_{vmd} is larger than D_g by a factor of $\exp[3\ln^2(\sigma_g)]$, any variability in D_g will be amplified in the determination of D_{smd} and D_{vmd}.

Figure 3.15 illustrates the extraordinarily minimal horizontal variability in accumulation mode size parameters, especially near the surface. The small-scale horizontal variability of these size parameters does increase slightly with height, though. This could be attributable to increasing vertical variability as altitude increases if the aerosol layers are not actually horizontal. In general, even on horizontal scales of more than 100 km, there is very little variability in the accumulation mode size parameters. This is supported by the fact that in all transects of both flights, the SD is no greater than 4% of the mean size of the accumulation mode D_g (and 14 of the 16 transects have a SD that is $\leq$ 2% of the mean).

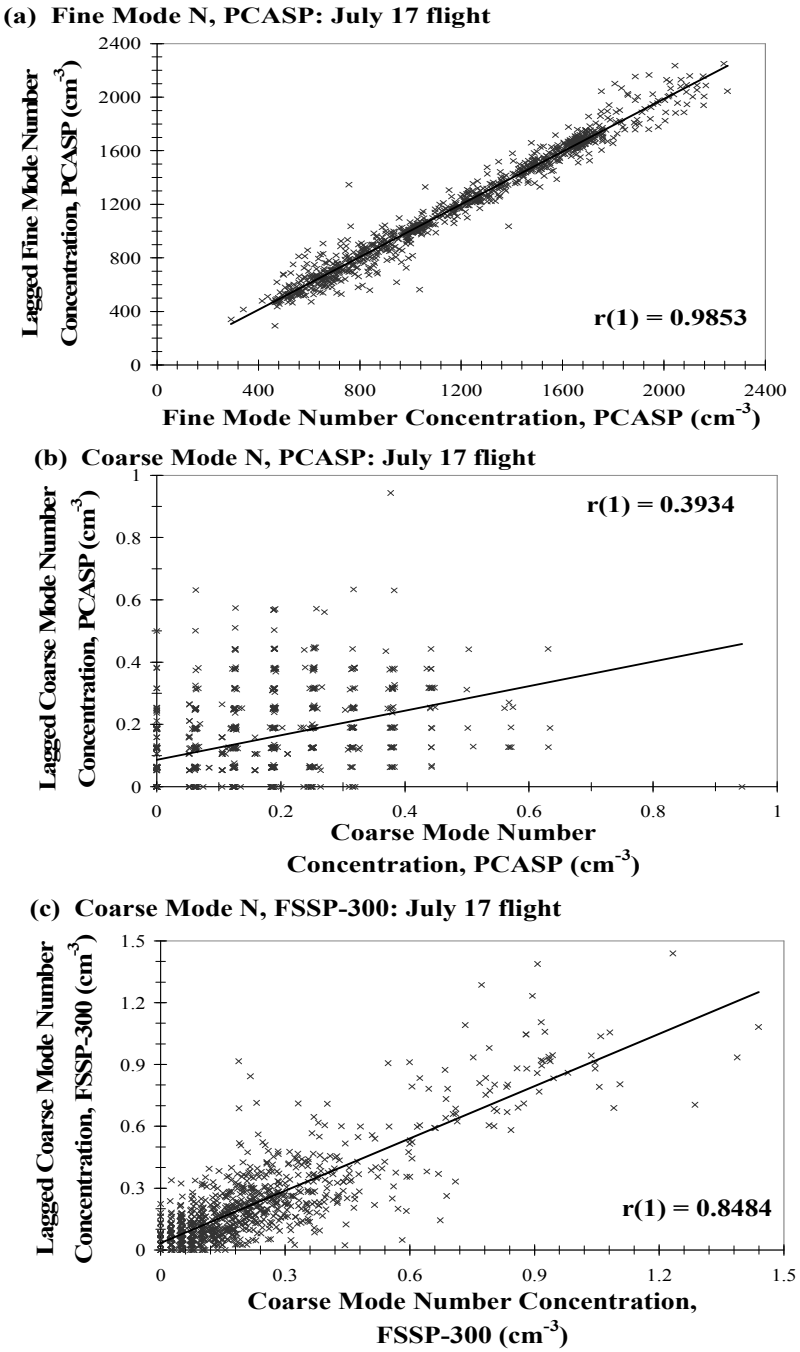

Figure 3.14 Lag-1 autocorrelation for number concentration, N, measurements for a given mode. (a) Fine mode N as measured with PCASP on July 17, 2001; (b) coarse mode N as measured with the PCASP on July 17; (c) coarse mode N as measured with the FSSP-300; (d) fine mode N as measured with the PCASP on August 2, 2001; (e) coarse mode N as measured with the PCASP on August 2, 2001; and (f) coarse mode N as measured with the FSSP-300 on August 2, 2001. The lag is one measurement interval, which we have chosen to be 10 s.

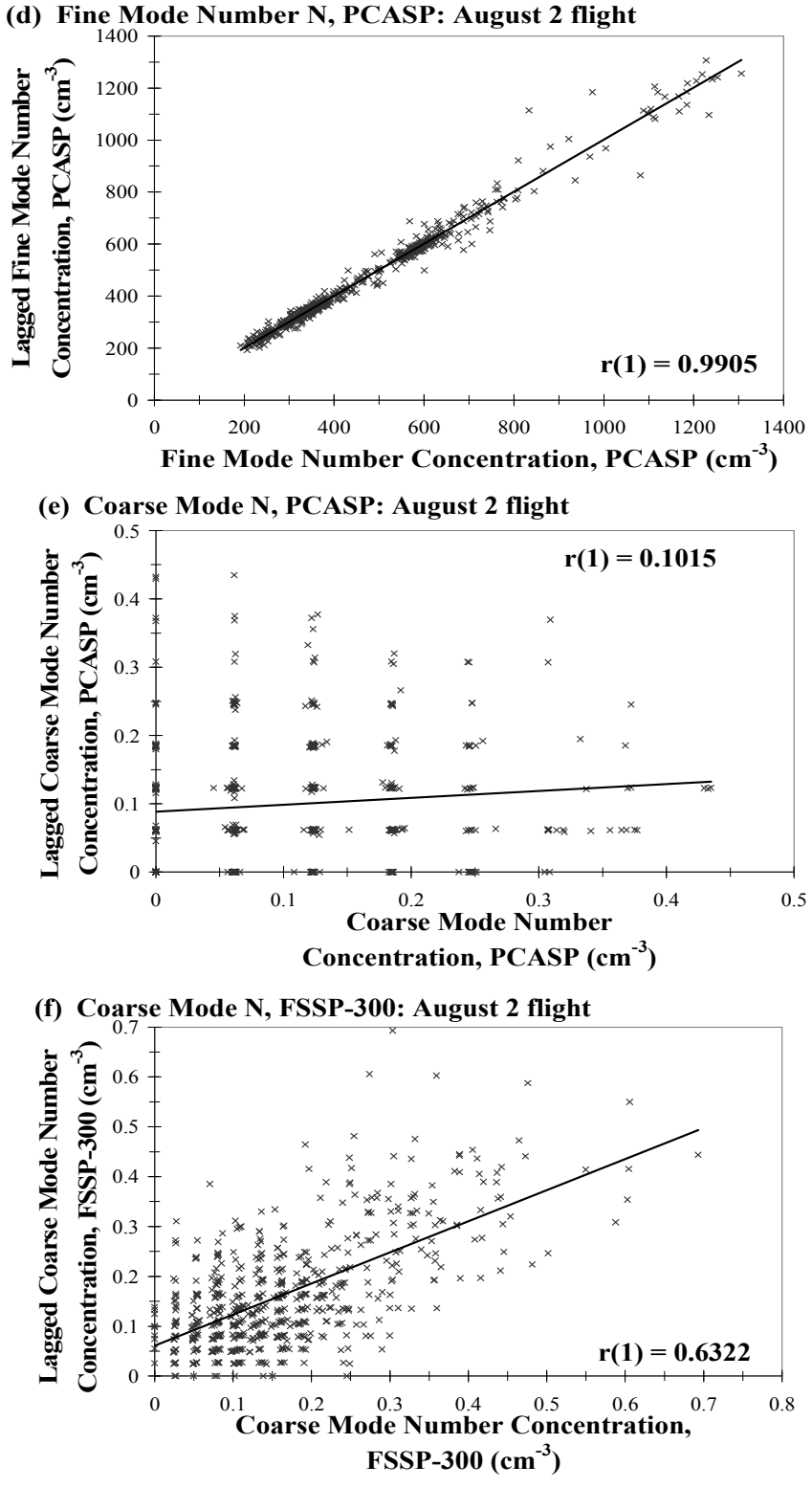

Figure 3.14 (continued)

Figure 3.14b,c,e & f shows that coarse mode particle number concentrations were remarkably low during these two days. Also, the r(1) values using a lag interval of 10 s were quite low, signifying either high instrument noise or ambient variability. Since the coarse mode N values were so low throughout CLAMS, we conclude that these measurements are a result of instrument noise. Therefore, no conclusion can be made regarding the variability of coarse mode size over small horizontal distances.

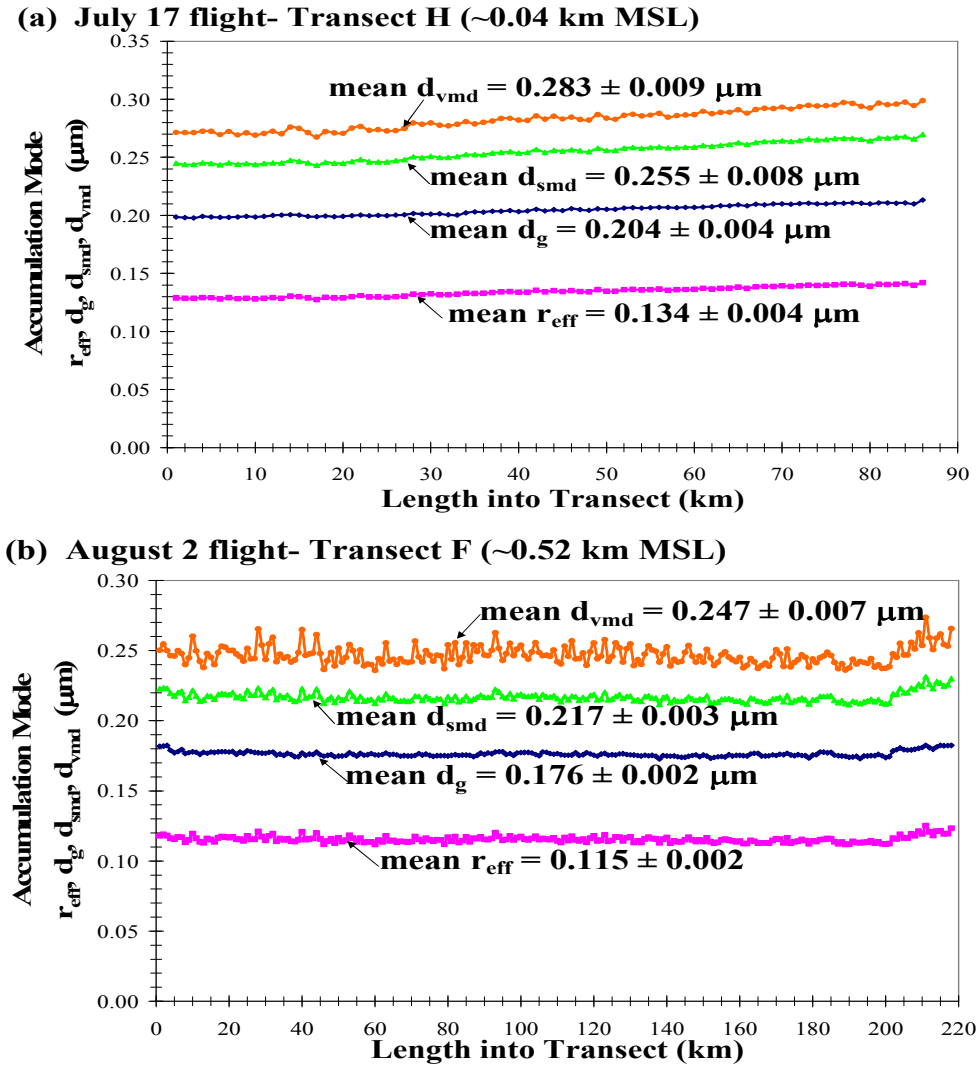

Figure 3.15 Small-scale (~1 km) horizontal variability of accumulation mode size parameters for selected transects from July 17 and August 2 flights representing various levels of the lower troposphere.

(c) August 2 flight- Transect A (~1.88 km MSL)

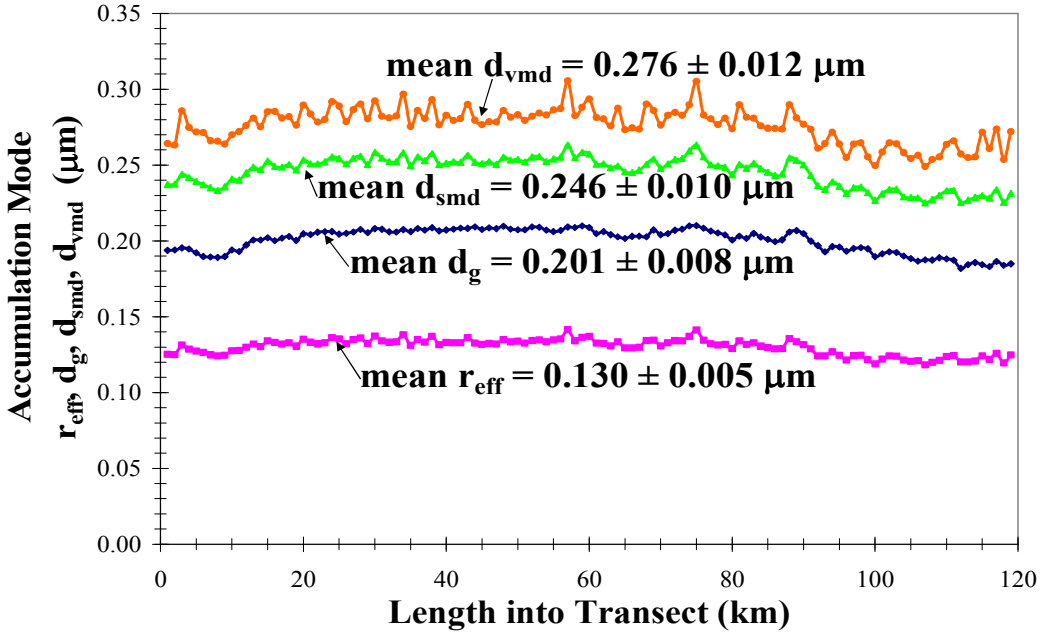

(d) July 17 flight- Transect C (~2.99 km MSL)

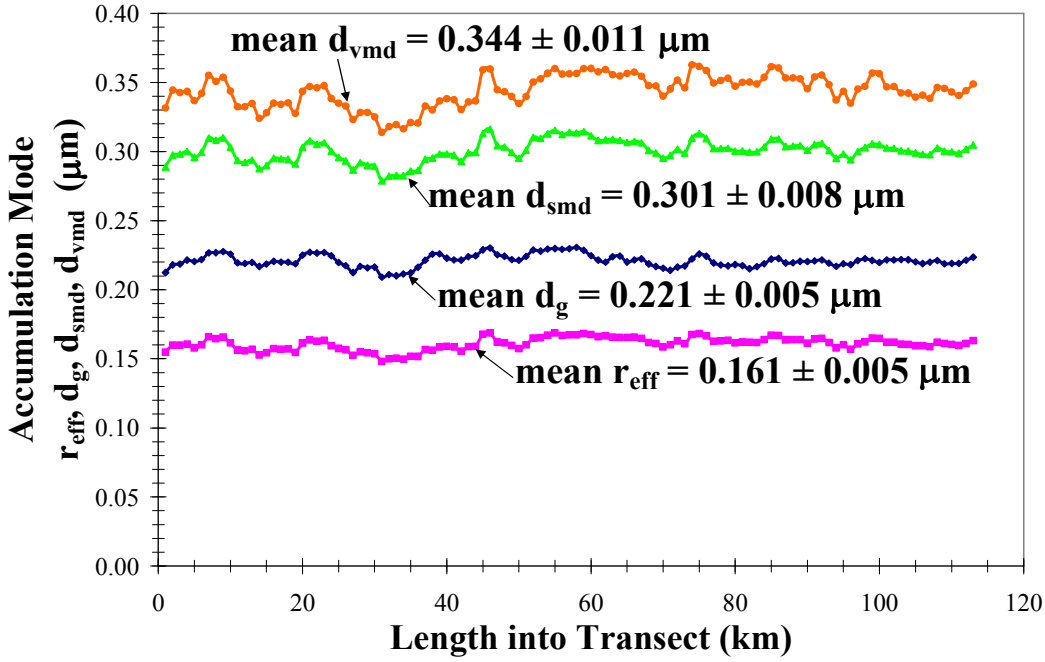

Figure 3.15 (continued)

3.3.4 Particle Number Concentration

Figure 3.16 shows the results from the autocorrelations for particle number concentration as measured by the PCASP, N_{PCASP}, [(a) July 17 and (b) August 2] and the TSI 3025A, N_{TSI}, [(c) July 17 and (d) August 2]. All four panels show very high autocorrelation coefficient values [(a) 0.9853; (b) 0.9905; (c) 0.9886; (d) 0.9950] when using a lag interval of 10 s, which corresponds to a spatial resolution of ~1 km. Therefore, we are confident that these data are free from instrument noise.

Since instrument noise is not a contributing factor to the variability in particle number concentration, we can look at Figure 3.17 to illustrate the small-scale horizontal variability of particle number concentrations measured by the PCASP (detection limits: 0.1 μm < D_p < 4.0 μm) and the TSI 3025A (detection limits: 3 nm < D_p < ~1.0 μm) for a few selected transects at various levels of the atmosphere from both the July 17 and August 2 flights. These transects are representative of ~1 km variability in particle number concentration in the other transects not presented here.

In all four transects shown in Fig. 3.17, the PCASP and TSI 3025A capture most all of the enhancements and declines in particle number concentration quite accurately. Fig. 3.17a is the near-surface example, showing a mean N_{PCASP} value of 341 ± 25 cm^{-3} (where the SD is 7% of the mean) and 5789 ± 567 cm^{-3} (SD is 10% of the mean) for N_{TSI}. Figure 3.17b shows a transect at ~0.5 km MSL, which was the longest transect of either of the two flights (218 km). Mean N_{PCASP} values at this level were 389 ± 57 cm^{-3} (SD is 15% of the mean) and 2009 ± 244 cm^{-3} (SD is 12% of the mean) for N_{TSI}. Figure 3.17d shows the particle number concentration results for the highest transect flown on either

day; the mean N_{PCASP} value was 825 ± 150 cm^{-3} (SD is 18% of the mean) and 2045 ± 249 cm^{-3} (SD is 12% of the mean) for N_{TSI}.

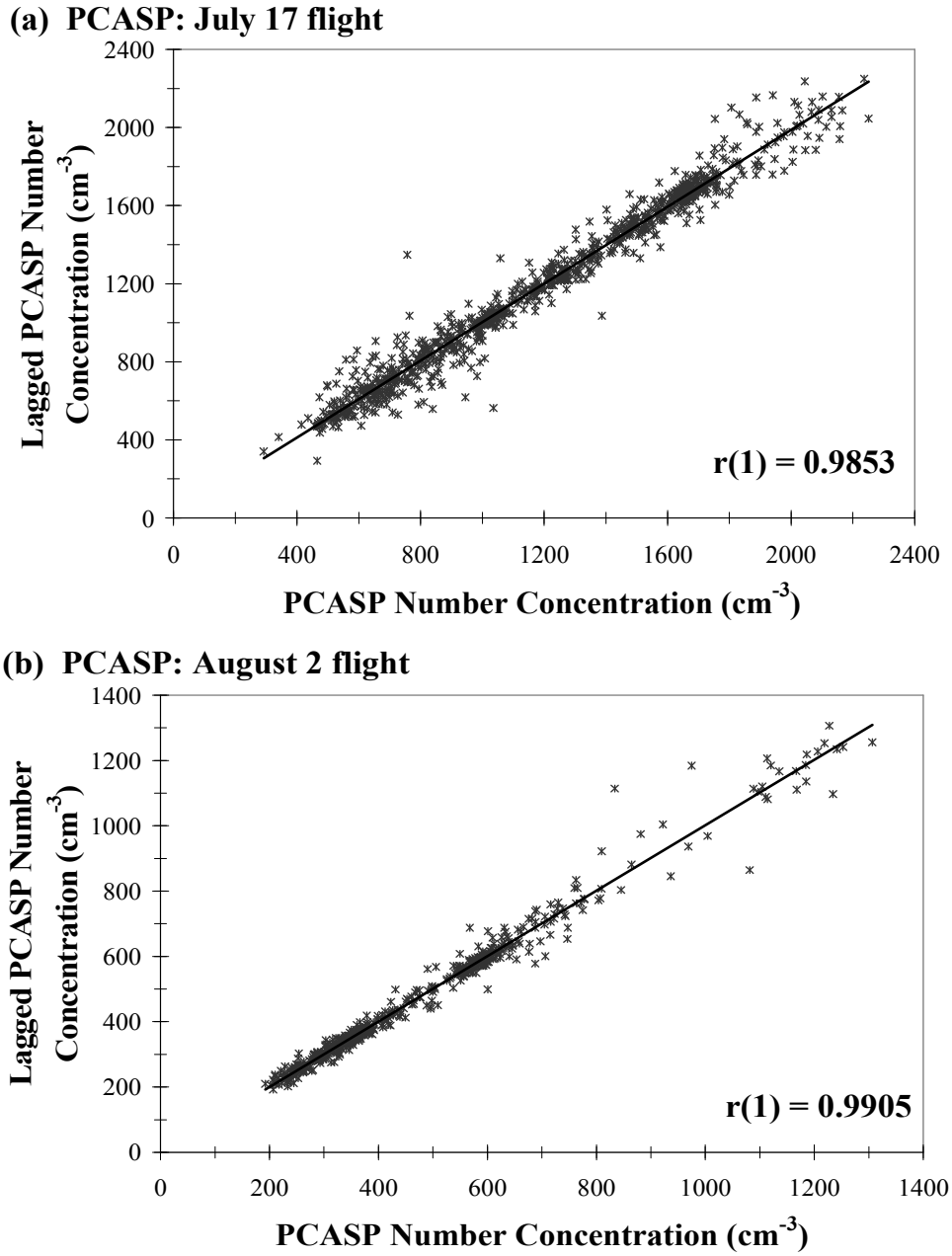

Figure 3.16 Lag-1 autocorrelation for N as measured by the PCASP [(a) July 17 and (b) August 2] and TSI 3025A [(c) July 17 and (d) August 2]. The lag is one measurement interval, which we have chosen to be 10 s or 1 km resolution.

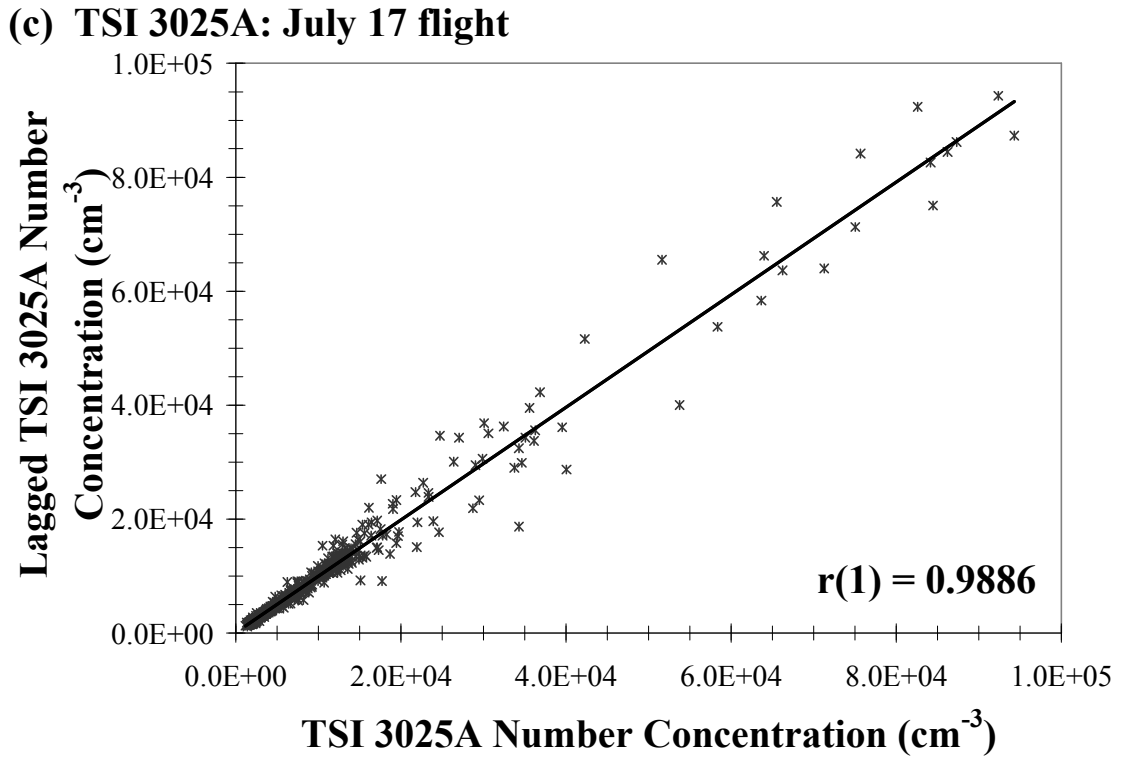

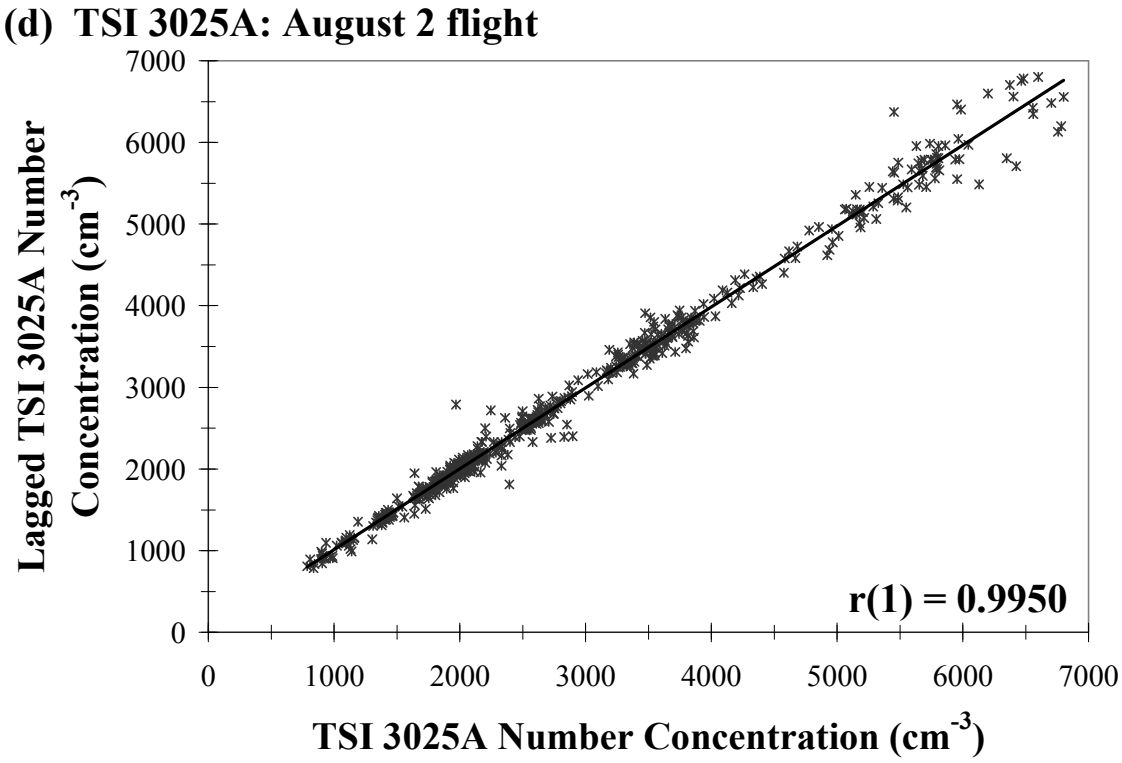

Figure 3.16 (continued)

Perhaps the most interesting frame is Fig. 3.17c, which shows a leg of the July 17 flight that had a large over-land component compared to the other transects of both flights that were mainly over the open ocean. There are two very strong, localized enhancements in particle number concentration (at x ≈ 25 km and x ≈ 95 km) that lead to the very large spread in number concentration values discussed in Section 3.1.4. The first enhancement occurs when the aircraft passed over the Great Dismal Swamp- a possible source of biogenic aerosols. The second, and much larger, enhancement occurred when the Convair-580 flew over Norfolk, VA- the lone urban center in the region of study, and a source of urban/anthropogenic particles. Interestingly, the variability in the N_{TSI} data is much greater than in the N_{PCASP} data, indicating that these enhancements are mainly due to very small ($D_p < 0.1$ μm) nucleation mode aerosols.

In all four transects shown (as well as those not presented here), N_{TSI} values were at least an order of magnitude greater than N_{PCASP} values. Given the differing detection limits of these instruments, it is clear there is a strong dominance by particles having $D_p <$ 0.1 μm at all levels of the lower troposphere. Furthermore, the variability in N_{PCASP} and N_{TSI} is actually lowest (in terms of SD as a % of mean) near the surface and consistently higher aloft. Finally, the km-to-km variability in N_{PCASP} and N_{TSI} can vary significantly on horizontal scales of a kilometer or less regardless of altitude (as much as 83.9 % with a mean of 4.9 ± 5.2 % for N_{PCASP} and as much as 93.9 % with a mean of 5.6 ± 5.8 % for N_{TSI}), though the variability is obviously greatest when in close proximity to a strong source of particulate matter and/or precursor gases.

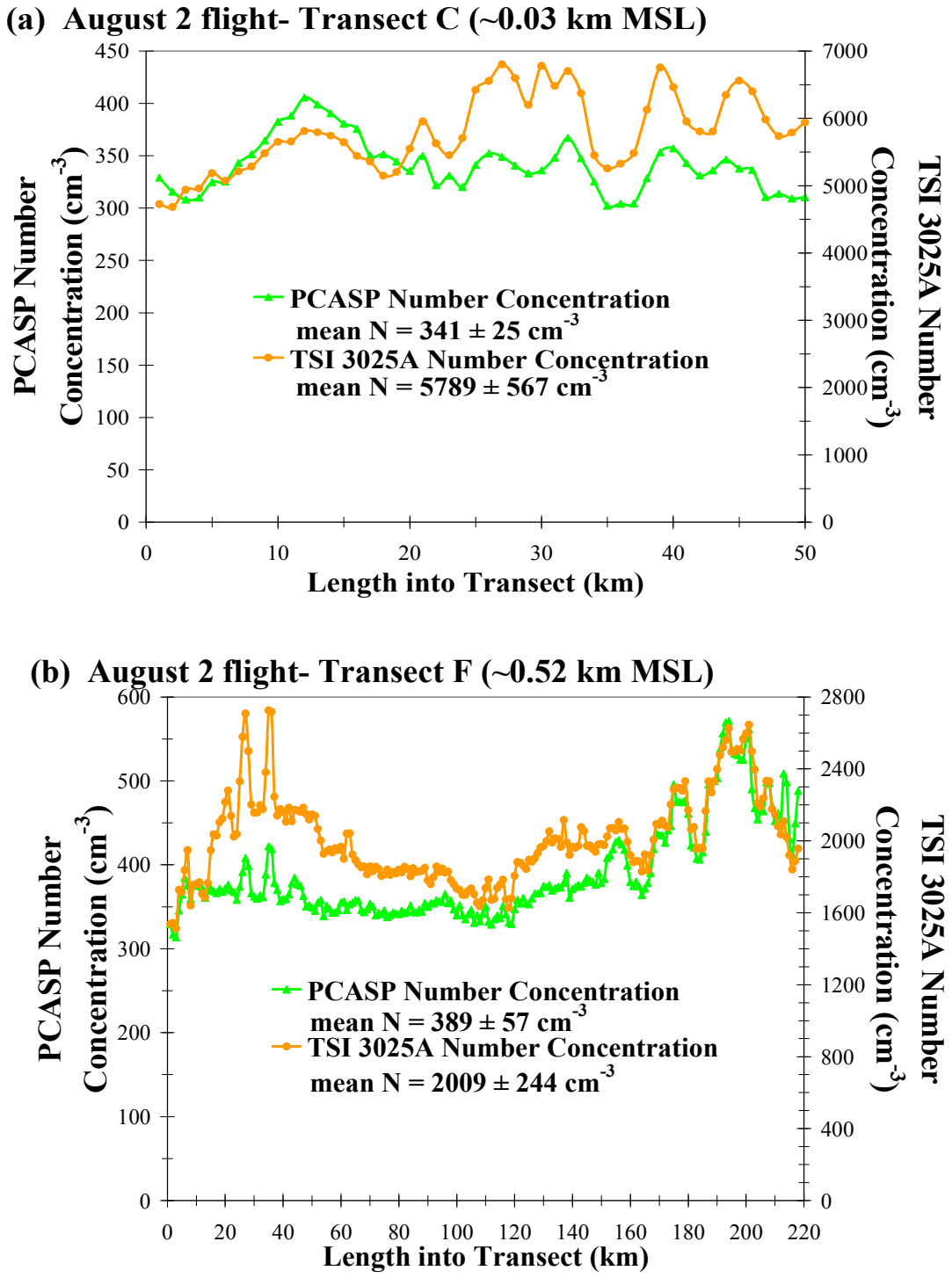

Figure 3.17 Small-scale (~1 km) horizontal variability of particle number concentration as measured by the TSI 3025A (orange circles) and PCASP (green triangles) for selected transects from July 17 and August 2 flights representing various levels of the lower troposphere.

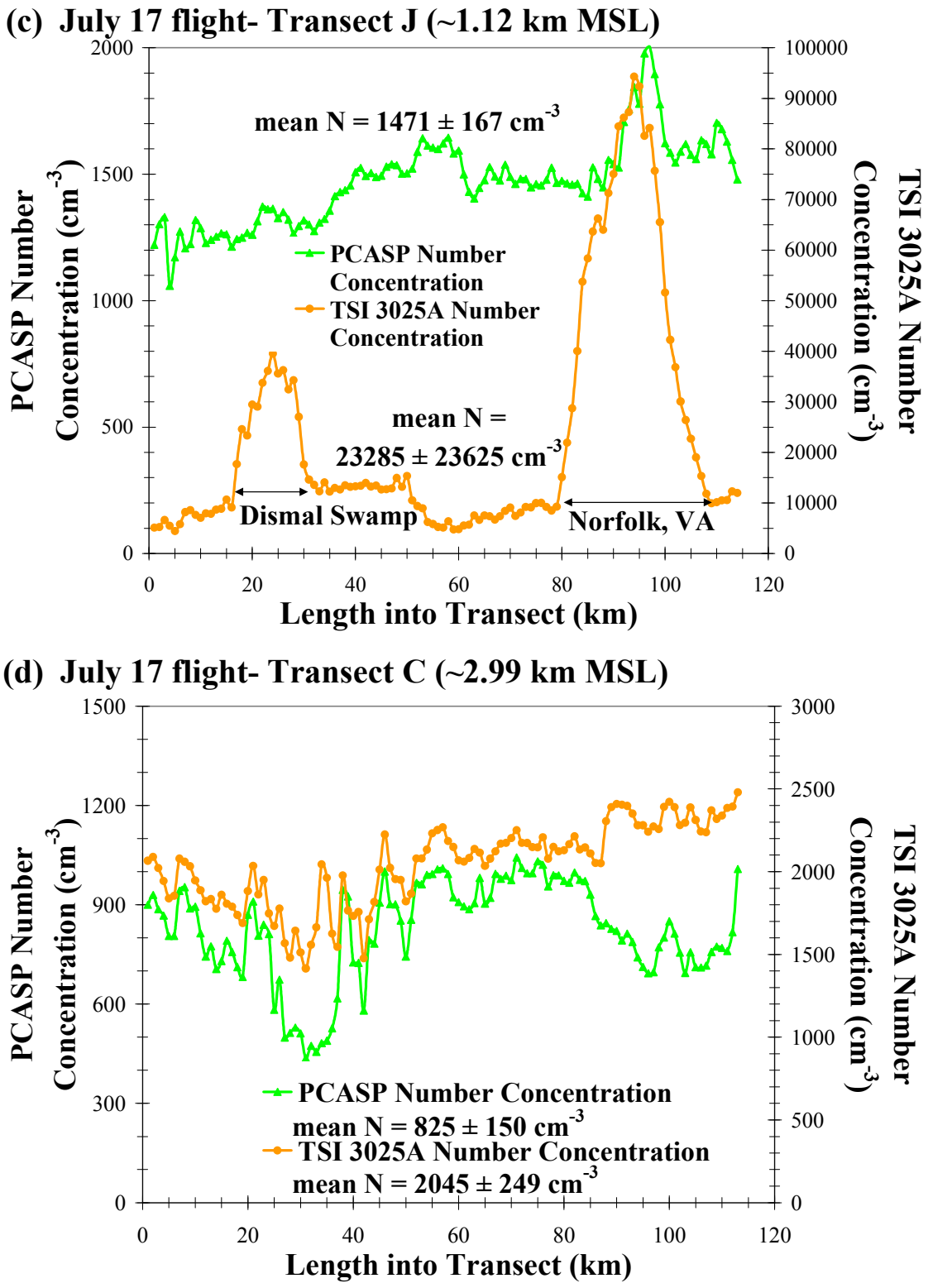

Figure 3.17 (continued)

3.3.5 Conclusions Regarding Small-scale Variability

As stated previously, an analysis of the small-scale horizontal variability of aerosol properties is needed to determine: a) if the resolution of the MISR aerosol retrieval algorithm is high enough to capture significant horizontal variability in aerosol properties, b) the effect of space/time offsets on the satellite validation results, and, c) whether or not the "layer method" employed in the particle size distributions is justified.

The resolution of the MISR aerosol retrieval algorithm is ~17.6 km. Therefore the resolution is high enough to capture horizontal variability in a given aerosol parameter if that parameter does not vary (or varies minimally) on a horizontal scale of ~15-20 km. Since ω_0, AOD and accumulation mode r_{eff} are the three aerosol parameters derived from MISR retrievals that are of most interest to the present study, we analyze their variability here. The ~4 km horizontal variability of ω_0 values derived from in situ measurements of σ_{sp} and σ_{apd} was quite small. The mean and SD for ~4 km changes in ω_0 values is 0.0039 ± 0.0047 (0.405 ± 0.495% change from the previous ~4 km) with a maximum of 0.0509 (5.70% change). Even on larger horizontal scales of 50-100 km, ω_0 almost always varied less than the uncertainty associated with the MISR retrieval of ω_0, which is ~0.05 (Kahn et al. 1998). Therefore, the resolution of the MISR aerosol retrieval was sufficient for accurately detecting any spatial variability in ω_0 during CLAMS.

The analysis of the small-scale horizontal variability in AOD (Fig. 3.12 and Fig. 3.13) coupled with the results from Redemann et al. (2005) show that the variability in AATS-derived AOD is less than the uncertainty associated with the retrieval of AOD

from MISR (0.05 or 20%, whichever is larger; Kahn et al. 2005). Thus, the resolution of the MISR retrieval is high enough to capture any significant variability in AOD during CLAMS. The in situ measurements of accumulation mode r_{eff} showed virtually no variability over horizontal scales of several hundred kilometers (Fig. 3.14 and Fig. 3.15); thus the resolution of the MISR aerosol retrieval was sufficient for accurately detecting any spatial variabilities in accumulation mode r_{eff} during CLAMS.

As discussed in Section 3.1.3, we used a "layer analysis" to determine the particle size distributions. Grouping transects which were flown over horizontal scales of several hundreds of km created the potential to mask any atmospheric variability. The results presented in Section 3.3.3 (and Fig.s 3.14-3.15) show that, in fact, minimal variability was masked using this "layer method". As Fig. 3.15 illustrates, the variability in accumulation mode size parameters is remarkably low over horizontal scales of several hundred km at all levels of the lower troposphere. The data are inconclusive with respect to spatial variability in the derived coarse mode size parameters, since the number concentration of coarse mode particles was so low. As a result, we see there is minimal horizontal variability in the relevant size parameters over distances of tens to hundreds of km (the mean % change from maximum to minimum r_{eff} values over entire transects is 9.7 ± 4.5 %, corresponding to 0.014 ± 0.008 μm) and a small uncertainty in the PCASP measurements (as described in Section 2.9); thus our methodology is justified.

3.4 Comparison of MISR Retrievals with Airborne In Situ Measurements

The main motivation for this research, and the CLAMS campaign in general, was to provide in situ measurements that would allow comparisons to (and thus validations of) remotely sensed aerosol parameters from the MISR satellite instrument. Previous studies have analyzed the success to which MISR-derived AOD values agree with those obtained from other measuring platforms such as the AATS-14 instrument (Redemann et al. 2005), and AERONET (Kahn et al. 2005). Redemann et al. (2005) showed that the correlation between AATS-14 and MISR standard algorithm regional mean AODs had an r-square of 0.94 during CLAMS. However, the authors point out that MISR AODs were systematically larger than the corresponding AATS values, with an rms difference of ~0.06. Kahn et al. (2005) compared a two-year measurement record of globally distributed AERONET sunphotometers and found that about two-thirds of the MISR-retrieved AOD values fall within 0.05 or ±20% (whichever is larger) of AERONET, and more than a third are within 0.03 or ±10% (whichever is larger).

Table 3.7 shows the results of the comparison between MISR-derived aerosol parameters and results from in situ measurements made aboard the Convair-580 aircraft during the two days of particular interest in CLAMS, on which we have concentrated here. However, these results are not necessarily directly comparable, since MISR values are total-column averages, while the aircraft measurements are not necessarily total column averages.

The most directly comparable aerosol property between the two measuring platforms is AOD. MISR retrieves total column effective AOD values, while the AATS-

14 (aboard the Convair-580 aircraft) provides a column-integrated AOD value for the total atmospheric column above the altitude of the aircraft. The Convair-580 AOD values presented in Table 3.7 are from the lowest transects flown for both flights (~ 50 m MSL), which intentionally coincided with the Terra overpass. Thus, the Convair-580 AOD values are very close to total column values. MISR and the AATS measured AOD at slightly different wavelengths (558 nm vs. 525 nm), therefore the Ångström exponent, å, as described by Anderson et al. (1999) (å = 2.02 ± 0.15 for July 17 and å = 1.98 ± 0.11 for August 2) has been applied to compare AOD at the same wavelength (558 nm). These results show that not only do the AOD values from both platforms agree very well on both days (July 17: 0.38 ± 0.05 from MISR and 0.34 ± 0.03 from the Convair-580; August 2: 0.10 ± 0.05 from MISR and 0.09 ± 0.01 from the Convair-580), but also the MISR retrieval did an excellent job in capturing the difference in AOD between both days.

While the data available for comparison of optical properties derived from Convair-580 and MISR measurements are limited, the available data from our in situ measurements allow for a rigorous test capable of disproving the MISR retrieval if it is erroneous. MISR retrieves column-effective aerosol optical properties, whereas ω_0 values derived from in situ measurements (presented in Table 2.3) are averages of ω_0 throughout an entire profile or transect.

Therefore, in order to make as accurate a comparison as possible between the in situ and MISR results, we compare the MISR-retrieved values of ω_0 to the mean ω_0

Table 3.7 Comparison of aerosol parameters as determined by MISR retrievals and Convair-580 measurements during CLAMS.

Date (2001)	Parameter	MISR	Convair-580
July 17	**AOD**	**0.38 ± 0.05** (558 nm)	**0.34 ± 0.03** (558 nm)
	ω_0	**> 0.95** (558 nm)	**0.97 ± 0.01** (550 nm)
	r_{eff}	**0.12 μm**	**0.14 μm**
	Classification	Small, spherical, clean	
August 2	**AOD**	**0.10 ± 0.05** (558 nm)	**0.09 ± 0.01** (558 nm)
	ω_0	**0.88 ± 0.05** (558 nm)	**0.93 ± 0.04** (550 nm)
	r_{eff}	**0.12 μm**	**0.12 μm**
	Classification	Small, spherical dirty	

values obtained during the profiles with the greatest vertical extent during each flight (profile #1 for July 17 and profile #2 for August 2).

However, horizontal and temporal offsets between MISR and the Convair-580 need to be accounted for, as does the aerosol above the top flight level of the aircraft. On both July 17 and August 2, MISR flew over the region of study at 36.90° latitude, -75.71° longitude. The mean aircraft location during the spiral ascent of profile #1 on July 17 was 36.92° latitude, -75.71° longitude. Similarly, the mean aircraft location for profile #2 on August 2 was 36.94° latitude, -75.78° longitude. Thus, mean horizontal offsets between the two platforms is less than the resolution of the MISR aerosol retrieval algorithm (~17.6 km). (The horizontal envelope of the flight pattern during profile #1 on July 17 was 8.8 km north/south and 10.7 km east/west. For profile #2 on August 2 the horizontal extent was 14.4 km north/south and 19.2 km east/west.) The MISR overpass occurred at 1608 UTC on both July 17 and August 2. Profile #1 of the July 17 flight was flown from 1305-1337 UTC, so there is a temporal offset of ~3 h. As Anderson et al. (2003a) discuss, this is not likely long enough for significant changes in aerosol

composition or number concentration, though this depends on gas and particle concentrations. As a result, the effect of advection must be investigated. While not ideal (since advection can vary significantly at different altitudes), the best way to account for advection when flying a vertical profile is to multiply the mean wind speed for the profile by the time it took to fly the entire profile. This value, α, can then be compared to the variability scale. The mean wind speed for profile #1 on July 17 was 12.7 ± 3.4 m s^{-1} and its duration was 31 min; thus α = 23.6 km for July 17. For profile #2 on August 2, the mean wind speed was 8.4 ± 4.3 m s^{-1} and it took 29 min to complete the profile; thus α = 14.6 km for August 2. Comparing these α values to the spatial variability scales discussed in Section 3.3, it can be seen that advection likely played a minimal role in introducing any new variability (since α is less than or equal to the general scales of variability discussed in Section 3.3).

On the August 2 flight, profile #2 was flown from 1626-1656 UTC- a temporal offset from the time of the MISR overpass of < 1 h. On July 17, the total column AOD (525 nm) as measured with the AATS from the lowest flight level (the base of profile #1, ~0.10 km MSL) was 0.408 ± 0.008. The AOD from the top of this profile to the top of the atmosphere was 0.012 ± <0.001, hence only ~3% of the AOD is unaccounted for in our vertical profile. Therefore, the mean value of ω_0 from profile #1 on July 17 represents the total column aerosol quite well. On August 2, the total column AOD (525 nm) from the base of profile #2 (~0.05 km MSL) was 0.095 ± 0.001. The AOD from the top of this profile to the top of the atmosphere was 0.015 ± <0.001, thus ~16% of the AOD is unaccounted for in this profile. (The effect of this unaccounted aerosol on values

of column ω_0 will be discussed shortly.) Therefore, unlike the July 17 case, on August 2 a relatively large amount of aerosol was unaccounted for by the in situ measurements. In summary, we are confident in directly comparing the in situ ω_0 values on both days with the column effective values derived from MISR, but the value of ω_0 derived from the in situ measurements on August 2 has a greater uncertainty.

The value of ω_0 at 550 nm using in situ data from the Convair-580 is 0.97 ± 0.01 for profile #1 of the 17 July 2001 flight, while that derived from MISR measurements at 558 nm for the same time is >0.95. The in situ value of ω_0 at 550 nm for profile #2 of the 2 August 2001 flight is 0.94 ± 0.03 and that derived from MISR measurements at 558 nm for the same time is 0.88 ± 0.05. While there is a significant amount of unaccounted aerosol aloft (i.e., above the top flight level) on August 2, a reasonable, yet conservative, estimation of ω_0 for the upper tropospheric/stratospheric aerosol given the relative homogeneity of the atmosphere on this day would be 0.90 ± 0.10. Weighting these values of ω_0 on August 2 (0.88 ± 0.05 for the lower troposphere and 0.90 ± 0.10 for the unaccounted aerosol aloft) by their respective AOD values, an estimation of total column ω_0 on August 2 is 0.93 ± 0.04. Therefore, the MISR-derived ω_0 values are in agreement (within the stated uncertainties) with the values of ω_0 obtained from the in situ measurements on both dates. It should be noted that the in situ values were measured at 550 nm, whereas MISR effective wavelength is 558 nm. As discussed by Hartley et al. (2000), any adjustment made to account for the 8 nm difference in the wavelengths at which these values of ω_0 are obtained, will result in a minimal change in ω_0 (< 0.01, which is less than the associated uncertainties).

As with the ω_0 values, a comparison between in situ and MISR particle size parameters is most useful when the in situ data are representative of the total column average particle size parameter. This is why the "layer analysis" (described in Section 3.1.3) has been employed. MISR retrievals provide total column average accumulation mode effective particle radius (r_{eff}) values. Thus, to compare in situ results with the remotely sensed results, the AOD-weighted total layer mean r_{eff} values (listed in Table 3.2) from the accumulation mode PCASP data are used. The total layer mean r_{eff} determined from measurements taken aboard the Convair-580 during the July 17 flight is 0.14 μm, while that derived from MISR retrievals is 0.12 μm. For the August 2 flight, both the Convair-580 measurements and MISR data yield an effective particle radius of 0.12 μm. Therefore, it can be seen that while the MISR retrievals did not capture the very small difference in r_{eff} values detected by the in situ measurements on both days, there is still very good agreement between the MISR and Convair-580 results on both days.

CHAPTER 4

SUMMARY AND CONCLUSIONS

The optical properties and size distributions of the aerosols measured aboard the UW's Convair-580 aircraft on July 17 and August 2, 2001 during the CLAMS field campaign have been summarized. These results have been discussed in detail and compared to results from the TARFOX field campaign as well as those from the MISR satellite sensor. Table 3.6 shows the results of this inter-campaign comparison, while Table 3.7 illustrates the inter-platform comparison.

Table 2.3 summarizes the single-scattering albedo values at a wavelength of 550 nm for each of the profiles and transects of the July 17 and August 2 flights. Single-scattering albedo values for all profiles flown on July 17 were significantly greater than those for the August 2 profiles. Therefore, the aerosol sampled on July 17 likely contained greater contributions from sulfate and possibly organic carbon particles.

The amount of aerosol was significantly higher on July 17 than on August 2 in terms of both boundary layer number and total column AOD. Furthermore, there was a predominance of particles with $D_p < 0.1$ μm on both days, indicative of secondary aerosol production by processes such as gas-to-particle conversion. Also, sea salt particles were present in the sub-0.5 km MSL layer on both days due to near-surface wind speeds of 5-10 m s^{-1}, but were only found further aloft on July 17 because of the more thoroughly mixed lower troposphere on this day. In general, slightly larger accumulation mode particles were present on July 17, as well. These differences are likely attributable to the

differing air parcel backtrajectories from both days. At low levels on July 17 (Fig. 2.2a) the air had been recirculating over the region of study for at least three days, allowing particle number concentrations to build up and particle growth by condensation of trace gases and coagulation with other particles. Further aloft on July 17 (Fig. 2.2b) the air had passed over Ontario and the Great Lakes region, thus the air sampled had a strong continental and/or anthropogenic influence. Conversely, the air parcel backtrajectories from August 2 (Fig. 2.3) indicate that the air had a strong maritime influence, having come from the north-northeast and east. As a result, on August 2, 2001, there were lower total particle number concentrations, less scattering and absorption, lower AOD values and slightly smaller accumulation mode size parameters.

Comparing the results from CLAMS to those from TARFOX, the aerosol in CLAMS was lower in total number concentration and mid-visible AOD and had slightly higher single-scattering albedo values (when looking at polluted layers where $\sigma_{sp} > 30 \times 10^{-6}$ m^{-1}), though this latter conclusion could have been due to the fact that Hartley et al. (2000) do not appear to have incorporated the scattering and calibration corrections to σ_{apd} recommended by Bond et al. (1999), both of which would tend to decrease σ_{apd} and thus increase ω_0. The aerosol composition was quite different in the two campaigns. These differences are due to differing airflow backtrajectories and meteorological conditions. In TARFOX, the airflows were mainly westerly or southwesterly, having passed over the industrial, agricultural and urban areas of the Midwestern and Southern U.S. The airflows during CLAMS, however, were more typically from the north or northeast, thus bringing cleaner air to the study region. Also, Smith et al. (2005) discuss

how weather conditions during CLAMS were atypical for summer along the East Coast of the U.S., due to an unusual number of cold frontal passages with a deep northeasterly flow of cool, clean, dry air. As a result, pollution (and thus, AOD, N, etc.) were uncharacteristically low during the CLAMS field study.

Redemann et al. (2005) concluded that the spatial variability in AOD during CLAMS was caused by the transport and diffusion of similar aerosol types, rather than to mixing of aerosol types with different sizes and compositions. Said another way, differential dilution is the probable cause of much of the variability (i.e., mixing of polluted and clean air). The transport and diffusion of similar aerosol types could create regions of higher (lower) particle number concentration, which would create more (less) light extinction in the region, and ultimately cause higher (lower) AOD values (i.e., spatial variability in AOD). This conclusion is strongly supported by the results presented herein showing that accumulation mode size, ω_0 and AOD did not vary to any significant degree on spatial scales of tens of km, and in some cases on scales of hundreds of km. Rather, the lone aerosol parameter we measured that showed any significant spatial variability was particle number concentration.. Figure 3.15 shows there is virtually no horizontal variability in accumulation mode size parameters; however we cannot make any conclusions regarding the horizontal variability in coarse mode size parameters due to the very low number concentrations of coarse mode particles at all levels throughout CLAMS. This analysis of the small-scale horizontal variability of several aerosol parameters provides an additional example, under different environmental conditions, to supplement previous variability studies such as the ACE-Asia campaign

discussed by Anderson et al. (2003b), as well as the review of mesoscale variations of tropospheric aerosols presented by Anderson et al. (2003a). The Anderson et al. (2003a & b) studies conclude that most of the variability is associated with extensive aerosol properties (e.g., σ_{sp}, σ_{apd}, AOD, etc.), while intensive aerosol properties (e.g., ω_0, particle size, etc.) are more homogeneous on scales of tens of km. The findings presented herein further support this conclusion.

As discussed in Section 2.15, MISR categorizes aerosol columns into about a dozen broad classes, based on particle size, shape, and crudely by composition. MISR sensitivity to ω_0 is 2-4 groupings over the natural range of aerosol values; ω_0 values of ~0.80, ~0.88, ~0.94, and 1.0 can typically be distinguished from one another (Kahn et al. 1998). These constraints are being updated and refined, as the validation process reflected by this and other studies progresses (e.g., Kahn et al. 2005). For example, Kalashnikova et al. (2005) have demonstrated that MISR data can be used to distinguish randomly oriented spheres, ellipsoids, grains, and plates. The MISR retrievals presented here are based on the early post-launch MISR Standard Aerosol algorithm (Version 12), which will be improved upon to incorporate the results presented herein as well as those from other validation efforts (Martonchik et al. 1998).

The MISR results (specifically ω_0 and r_{eff}, as well as broader information on size and composition) for July 17 and August 2 compare well with the in situ measurements obtained aboard the Convair-580. On July 17, the MISR algorithm showed "mostly small, spherical, clean" particles and on August 2 "small, spherical, dirty" aerosols. The Convair-580 results give small particles on both days: r_{eff} of 0.14 μm from the PCASP

compared to 0.12 μm from MISR on July 17, and 0.12 μm from both the PCASP and MISR on August 2. Also, the profile mean ω_0 value from the Convair-580 data on July 17 (0.97 ± 0.01) corresponds well with the MISR result of > 0.95. The profile mean ω_0 value on August 2 (0.94 ± 0.03), as well as the estimated total column mean (0.93 ± 0.04) agree with the MISR-retrieved total column ω_0 value of 0.88 ± 0.05 given the uncertainties associated with each value. It should be noted, though, that there was a significant amount of aerosol (16% of AOD at 525 nm) that was above the highest flight level, and thus unaccounted for, on August 2. We, therefore, cannot be as confident in the inter-platform comparisons on August 2 as we are for those on July 17. It should be noted that the MISR retrievals were derived prior to analyzing the Convair-580 data, and neither data set was adjusted in any way.

Future work could include an analysis of other in situ data sets (e.g., SAFARI-2000, ACE-Asia, etc.) acquired via aircraft in an effort to provide further validation information to, not only, MISR but also MODIS retrievals. It would also be interesting to compare the optical and physical aerosol parameters between the various field campaigns as well as any differences in the small-scale horizontal variabilities in aerosol properties.

REFERENCES

Alam, A., J. P. Shi, and R. M. Harrison, 2003: Observations of new particle formation in urban air. *J. Geophys. Res.*, **108,** 4093–4109.

Anderson, T. L., D. S. Covert, S. F. Marshall, M. L. Laucks, R. J. Charlson, A. P. Waggoner, J.A. Ogren, R. Caldow, R. L. Holm, F. R. Quant, G. J. Sem, A. Wiedensohler, N. A. Ahlquist, and T. S. Bates, 1996: Performance characteristics of a high-sensitivity, three-wavelength, total scatter/backscatter nephelometer. *J. Atmos. & Ocean. Technol.*, **13,** 967–986.

_____, and J. A. Ogren, 1998: Determining aerosol radiative properties using the TSI 3563 integrating nephelometer. *Aerosol Sci. Technol.*, **29,** 57–69.

_____, D. S. Covert, J. D. Wheeler, J. M. Harris, K. D. Perry, B. E. Trost, D. J., Jaffe, and J. A. Ogren, 1999: Aerosol backscatter fraction and single scattering albedo: Measured values and uncertainties at a coastal station in the Pacific Northwest. *J. Geophys. Res.*, **104**, 26,793-26,807

_____, R. J. Charlson, D. M. Winker, J. A. Ogren, and K. Holmen, 2003a: Mesoscale variations of tropospheric aerosols. *J. Atmos. Sci.*, **60,** 119–136.

_____, S. J. Masonis, D. S. Covert, N. C. Ahlquist, S. G. Howell, A. D. Clarke, and C. S. McNaughton, 2003b: Variability of aerosol optical properties derived from in situ aircraft measurements during ACE-Asia, *J. Geophys. Res.,* **108**, 8647-8665.

Baumgardner, D., J. E. Dye, B. W. Gandrud, and R. G. Knollenberg, 1992: Interpretation of measurements made by the forward scattering spectrometer probe (FSSP-300) during the Airborne Arctic Stratospheric Expedition. *J. Geophys. Res.*, **97,** 8035–8046.

Birmili, W., A. Wiedensohler, J. Heintzenberg, and K. Lehmann, 2001: Atmospheric particle number size distribution in central Europe: Statistical relations to air masses and meteorology. *J. Geophys. Res.*, **106,** 32,005–32,018.

Bodhaine, B. A., 1995: Aerosol absorption measurements at Barrow, Mauna Loa and the South Pole. *J. Geophys. Res.*, **100,** 8967–8975.

Bond, T. C., T. L. Anderson, and D. Campbell, 1999: Calibration and intercomparison of filter-based measurements of visible light absorption by aerosols. *Aerosol Sci. Technol.*, **30,** 582–600.

Brook, J. R., A. H. Wiebe, S. A. Woodhouse, C. V. Audette, T. F. Dann, S. Callaghan, M. Piechowski, E. Dabek-Zlotorzynska and J. F. Dloughy, 1997: Temporal and

spatial relationships in fine particle strong acidity, sulphate, PM_{10}, and $PM_{2.5}$ across multiple Canadian locations. *Atmos. Environ.*, **31**, 4223-4236.

Castanho, A. D. A., J. V. Martins, P. V. Hobbs, P. Artaxo, L. Remer, M. Yamasoe, and P. R. Colarco, 2005: Chemical characterization of aerosols on the East Coast of the United States using aircraft and ground-based stations during the CLAMS experiment. *J. Atmos. Sci.*, **62**, 934-946.

Charlson, R. J., S. E. Schwartz, J. M. Hales, R. D. Cess, J. A. Coakley, Jr., J. E. Hansen, and D. J. Hofmann, 1992: Climate forcing by anthropogenic aerosols. *Science*, **255**, 423-430.

Covert, D. S., V. N. Kapustin, T. S. Bates, and P. K. Quinn, 1996: Physical properties of marine boundary layer particles of the mid-Pacific in relation to sources and meteorological transport. *J. Geophys. Res.*, **101,** 6919–6930.

Diner, D. J., J. C. Beckert, T. H. Reilly, C. J. Bruegge, J. E. Conel, R. Kahn, J. V. Martonchik, T. P. Ackerman, R. Davies, S. A. W. Gerstl, H. R. Gordon, J-P. Muller, R. Myneni, R. J. Sellers, B. Pinty, and M. M. Verstraete, 1998: Multiangle Imaging SpectroRadiometer (MISR) description and experiment overview. *IEEE Trans. Geosci. Remt. Sens.*, **36,** 1072–1087.

Hartley, W. S., P. V. Hobbs, J. L. Ross, P. B. Russell, and J. M. Livingston, 2000: Properties of aerosols aloft relevant to direct radiative forcing off the mid-Atlantic coast of the United States. *J. Geophys. Res.*, **105,** 9859–9885.

_____ and P. V. Hobbs, 2001: An aerosol model and aerosol-induced changes in clear-sky albedo off the east coast of the United States. *J. Geophys. Res.*, **106**, 9733-9748.

Haywood, J. and O. Boucher, 2000: Estimates of the direct and indirect radiative forcing due to tropospheric aerosols: A review. *Rev. Geophys.* **38**, 513-543.

Hegg, D. A., J. Livingston, P. V. Hobbs, T. Novakov, and P. Russell, 1997: Chemical apportionment of aerosol column optical depth off the mid-Atlantic coast of the United States. *J. Geophys. Res.*, **102,** 25,293–25,303.

_____ and Y. J. Kaufman, 1998: Measurements of the relationship between submicron aerosol number and volume concentration. *J. Geophys. Res.*, **103**, 5671-5678.

Hobbs, P. V., 1999: An overview of the University of Washington airborne measurements and results from the Tropospheric Aerosol Radiative Forcing Observational Experiment (TARFOX). *J. Geophys. Res.*, **104**, 2233-2238.

Hobbs, P. V., 2000: *Introduction to Atmospheric Chemistry*, Cambridge University Press, 262 pp.

Hoppel, W. A., G. M. Frick, J. W. Fitzgerald, and R. E. Larson, 1994: Marine boundary layer measurements of new particle formation and the effects of nonprecipitating clouds have on aerosol size distribution. *J. Geophys. Res.,* **99,** 14,443–14,459.

Huebert, B. J., G. Lee, and W. L. Warren, 1990: Airborne aerosol inlet passing efficiency measurement. *J. Geophys. Res.*, **95**, 16,369-16381.

Ibald-Mulli, A., H. E. Wichmann, W. Kreyling, and A. Peters, 2002: Epidemiological evidence on health effects of ultrafine particles. *J. Aerosol. Med.*, **15**, 189-201.

Intergovernmental Panel on Climate Change (IPCC), 2001: *Climate Change 2001: The Scientific Basis*, J. T. Houghton et al., Eds., Cambridge Univ. Press, 896 pp.

Jaenicke, R., 1993: Tropospheric aerosols. In *Aerosol-Cloud-Climate Interactions.* P. V. Hobbs, Ed., Academic Press, 1–31.

Kahn, R., P. Banerjee, D. McDonald, and D. Diner, 1998: Sensitivity of multiangle imaging to aerosol optical depth, and to pure-particle size distribution and composition over ocean. *J. Geophys. Res.*, **103,** 32,195–32,213.

_____, _____, and _____, 2001: The sensitivity of multiangle imaging to natural mixtures of aerosols over ocean. *J. Geophys. Res.*, **106,** 18219–18238.

_____, J. Anderson, T. L. Anderson, T. Bates, F. Brechtel, C. M. Carrico, A. Clarke, S. J. Doherty, E. Dutton, R. Flagan, R. Frouin, H. Fukushima, B. Holben, S. Howell, B. Huebert, A. Jefferson, H. Jonsson, O. Kalashnikova, J. Kim, S-W. Kim, P. Kus, W-H. Li, J. M. Livingston, C. McNaughton, J. Merrill, S. Mukai, T. Murayama, T. Nakajima, P. Quinn, J. Redemann, M. Rood, P. Russell, I. Sano, B. Schmid, J. Seinfeld, N. Sugimoto, J. Wang, E.J. Welton, J-G. Won and S-C. Yoon, 2004: Environmental snapshots from ACE-Asia. *J. Geophys. Res.*, **109,** D19S14, doi:10.1029/2003JD004339.

_____, B. J. Gaitley, J. V. Martonchik, D. J. Diner, K. A. Crean, and B. Holben, 2005: Multiangle imaging spectroradiometer (MISR) global aerosol optical depth validation based on 2 years of coincident Aerosol Robotic Network (AERONET) observations. *J. Geophys. Res.*, **110,** D10S04, doi:10.1029/2004JD004706.

Kalashnikova O. V., R. Kahn, I. N. Sokolik, and W.-H. Li 2005: Ability of multiangle remote sensing observations to identify and distinguish mineral dust types:

Optical models and retrievals of optically thick plumes, *J. Geophys. Res.*, **110**, D18S14, doi:10.1029/2004JD004550.

Kim, Y. J., and J. F. Boatman, 1990: Size calibration corrections for the Forward Scattering Spectrometer Probe (FSSP) for measurements of atmospheric aerosols of different refractive indices. *J. Atmos. & Ocean. Technol.*, **7,** 681–688.

Kotchenruther, R. A., P. V. Hobbs, and D. A. Hegg, 1999: Humidification factors for atmospheric aerosols off the mid-Atlantic coast of the United States. *J. Geophys. Res.*, **104,** 2239–2251.

Li, J., J. D. G. Wong, J. S. Dobbie, and P. Chylek, 2001: Parameterization of the optical properties of sulfate aerosols. *J. Atmos. Sci.*, **58**, 193-209.

Liu, P. S. K., W. R. Leaitch, J. W. Strapp, and M. A. Wasey, 1992: Response of PMS airborne ASASP and PCASP to NaCl and latex particles. *Aerosol Sci. Technol.*, **16,** 83–95.

Magi, B. I., P. V. Hobbs, T. W. Kirchstetter, T. Novakov, D. A. Hegg, S. Gao, J. Redemann, and B. Schmid, 2005: Aerosol properties and chemical apportionment of the aerosol optical depth at locations off the U.S. East Coast in July and August 2001. *J. Atmos. Sci.,* **62**, 919-933.

Makela, J. M., I. K. Koponen, P. Aalto, and M. Kumala, 2000: One-year data of submicron size modes of tropospheric background aerosol in southern Finland. *J. Aerosol Sci.*, **31,** 595–611.

Martonchik, J. V., D. J. Diner, R. Kahn, M. M. Verstraete, B. Pinty, H. R. Gordon, and T. P. Ackerman, 1998: Techniques for the retrieval of aerosol properties over land and ocean using multiangle data. *IEEE Trans. Geosci. Remt. Sens.*, **36,** 1212–1227.

_____, _____, K. Crean, and M. Bull, 2002: Regional aerosol retrieval results from MISR. *IEEE Trans. Geosci. Remt. Sens.*, **40,** 1520–1531.

McMurry, P. H., 2000: A review of atmospheric aerosol measurements. *Atmos. Environ.*, **34**, 1959-1999.

Murphy, D. M., D. J. Cziczo, P. K. Hudson, M. E. Schein, and D. S. Thomson, 2004: Particle density inferred from simultaneous optical and aerodynamic diameters sorted by composition. *J. Aerosol Sci.*, **35,** 135–139.

Novakov, T., D. A. Hegg, and P. V. Hobbs, 1997: Airborne measurements of carbonaceous aerosols on the east coast of the United States. *J. Geophys. Res.,* **102,** 30,023–30,030.

O'Dowd, C. D., M. H. Smith, I. E. Consterdine, and J. A. Lowe, 1997: Marine aerosol, sea salt, and the marine sulphur cycle: a short review. *Atmos. Environ.*, **31,** 73–80.

Parungo, F., C. Nagamoto, and R. Madel, 1987: A study of the mechanisms of acid rain formation. *J. Atmos. Sci.*, **44**, 3162-3174.

Peters, A., H.E. Wichmann, T. Tuch, J. Heinrich, and J. Heyder, 1997: Respiratory effects are associated with the number of ultrafine particles. *Am. J. Respir. Crit. Care Med.*, **155**, 1376-1383.

Redemann, J., P. B. Russell, and P. Hamill, 2001: Dependence of aerosol light absorption and single-scattering albedo on ambient relative humidity for sulfate aerosols with black carbon cores. *J. Geophys. Res.*, **106**, 27485-27495.

Redemann, J., B. Schmid, J. A. Eilers, R. Kahn, R. C. Levy, P. B. Russell, J. M. Livingston, P. V. Hobbs, W. L. Smith, and B. N. Holben, 2005: Suborbital measurements of spectral aerosol optical depth and its variability at subsatellite grid scales in support of CLAMS 2001. *J. Atmos Sci.*, **62**, 993-1007.

Reid, J. S., and P. V. Hobbs, 1998: Physical and optical properties of young smoke from individual biomass fires in Brazil. *J. Geophys. Res.,* **103,** 32,013–32,030.

Reist, P. C., 1993: *Aerosol Science and Technology*, 2nd Edition, McGraw-Hill, 379 pp.

Rogers, R. R., and M. K. Yau, 1989: *A Short Course in Cloud Physics*, 3rd Edition, Butterworth-Heinemann, 290 pp.

Russell, P. B., J. M. Livingston, P. Hignett, S. Kinne, J. Wong, A. Chien, R. Bergstrom, P. Durkee, and P. V. Hobbs, 1999: Aerosol-induced radiative flux changes off the United States mid-Atlantic coast: Comparison of values calculated from sunphotometer and in situ data with those measured by airborne pyranometer. *J. Geophys. Res.*, **104**, 2289-2307.

Schmid, B. and C. Wehrli, 1995: Comparison of sunphotometer calibration by Langley technique and standard lamp, *Appl. Opt.*, **34**, 4500-4512.

Seinfeld, J. H., 1989: Urban Air Pollution: State of the Science. *Science*, **243**, 745-752.

_____, and S. N. Pandis, 1998: *Atmospheric Chemistry and Physics: From Air Pollution to Climate Change*, John Wiley & Sons, 1326 pp.

Sloane, C. S. and W. H. White, 1986: Visibility: An evolving issue. *Environ. Sci. Technol.*, **20**, 760-766.

Smirnov, A., B. N. Holben, O. Dubovik, N. T. O'Neill, L. A. Remer, T. F. Eck, I. Slutsker, and D. Savoie, 2000: Measurement of atmospheric optical parameters on U.S. Atlantic coast sites, ships, and Bermuda during TARFOX. *J. Geophys. Res.*, **105**, 9887-9901.

Smith, W. L., T. P. Charlock, R. Kahn, J. V. Martins, L. A. Remer, P. V. Hobbs, J. Redemann, and C. K. Rutledge, 2005: EOS *Terra* aerosol and radiative flux validation: An overview of the Chesapeake Lighthouse and Aircraft Measurements for Satellites (CLAMS) experiment. *J. Atmos. Sci.*, **62**, 903-918.

Stein, S. W., B. J. Gabrio, D. Oberreit, P. Hairston, P. B. Myrdal, and T. J. Beck, 2002: An evaluation of mass-weighted size distribution measurements with the Model 3320 aerodynamic particle sizer. *Aerosol Sci. Technol.*, **36,** 845–854.

Tanre, D., L. A. Remer, Y. J. Kaufman, S. Mattoo, P. V. Hobbs, J. M. Livingston, P. B. Russell, and A. Smirnov, 1999: Retrieval of aerosol optical thickness and size distribution over ocean from the MODIS airborne simulator during TARFOX. *J. Geophys. Res.*, **104**, 2261-2278.

van de Hulst, H. C., 1981: *Light Scattering by Small Particles*, Dover Publications, 470 pp.

Wallace, J. M., and P. V. Hobbs, 1977: *Atmospheric Science: An Introductory Survey*, Academic Press, 467 pp.

Wang, J., R. C. Flagan, J. H. Seinfeld, H. H. Jonsson, D. R. Collins, P. B. Russell, B. Schmid, J. Redemann, J. M. Livingston, S. Gao, D. A. Hegg, E. J. Welton and D. Bates, 2002: Clear-column radiative closure during ACE-Asia: Comparison of multiwavelength extinction derived from particle size and composition with results from Sun photometry. *J. Geophys. Res.*, **107**, 4688–4909.

Willeke, K., and P. A. Baron, Eds., 1993: *Aerosol Measurement: Principles, Techniques and Applications*, Van Nostrand Reinhold, 876 pp.

Worsnop, D. J., J. W. Morris, Q. Shi, P. Davidovits, and C. E. Kolb, 1996: A chemical kinetic model for reactive transformations of aerosol particles. *Geophys. Res. Lett.*, **29**, doi:10.1029/2002GL015542.

APPENDIX A

MISR image of CLAMS study region on July 17, 2001; red dot indicates the location of the MISR/Convair-580 comparison

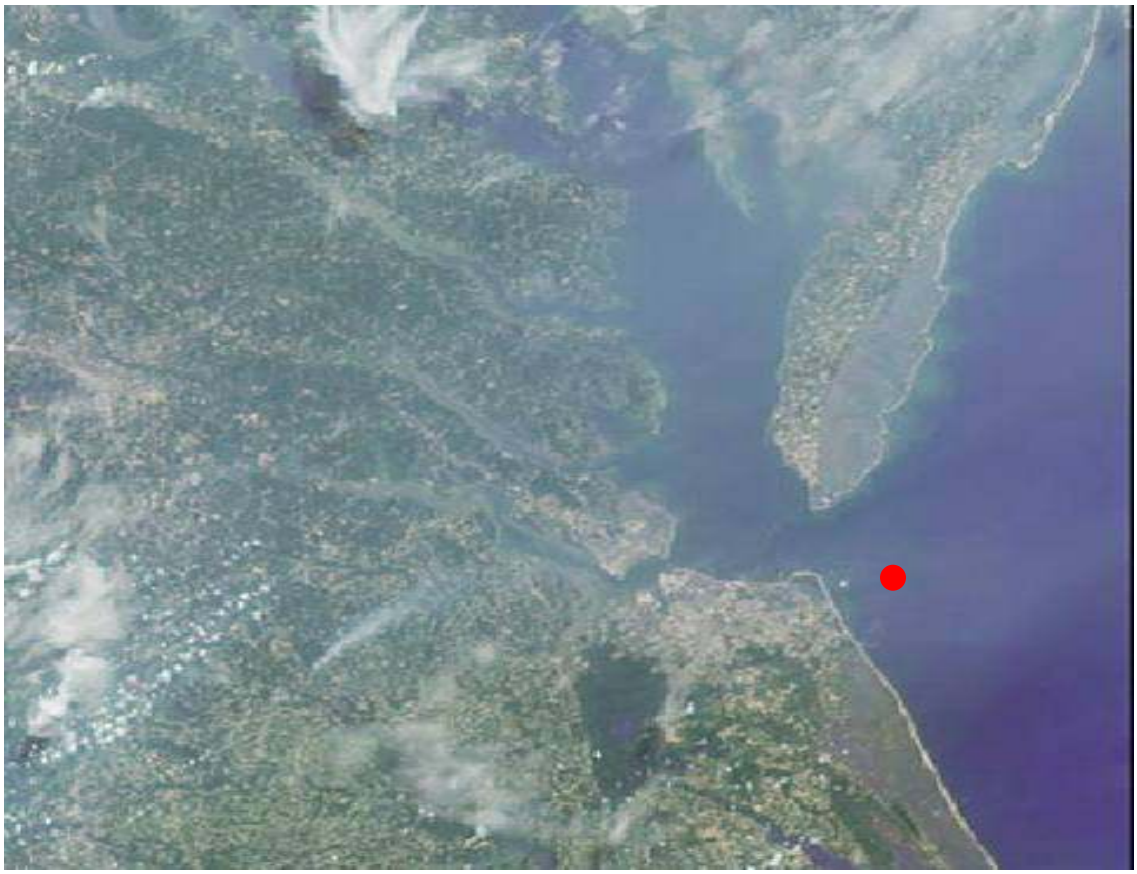

APPENDIX B

MISR image of CLAMS study region on August 2, 2001; red dot indicates the location of the MISR/Convair-580 comparison